Πολυτεχνειο Κρητης

Σχολη Μηχανικων Ορυκτων Πορων

Διδακτορικη Διατριβη

Μαρία Στρατηγάκη

Μικροδομή και Μηχανικές Ιδιότητες Σύνθετων Υλικών Κεραμικής Μήτρας με Μεταλλικά Εγκλείσματα

Microstructure and Mechanical Properties of Metal/Ceramic-matrix Composites

Ιουλιος 2018

ΠΟΛΥΤΕΧΝΕΙΟ ΚΡΗΤΗΣ

ΣΧΟΛΗ ΜΗΧΑΝΙΚΩΝ ΟΡΥΚΤΩΝ ΠΟΡΩΝ

ΔΙΔΑΚΤΟΡΙΚΗ ΔΙΑΤΡΙΒΗ

Μικροδομή και Μηχανικές Ιδιότητες Σύνθετων Υλικών Κεραμικής Μήτρας με Μεταλλικά Εγκλείσματα

Συγγραφέας:
Μαρία Στρατηγάκη

Επιβλέπων:
Αλέξανδρος Δ. Γκότσης

Διατριβή υποβληθείσα στα πλαίσια των απαιτήσεων
για την απόκτηση του Διδακτορικού τίτλου του Πολυτεχνείου Κρήτης

Ιούλιος 2018

Technical University of Crete

School of Mineral Resources Enginnering

DOCTORAL THESIS

Microstructure and Mechanical Properties of Metal/Ceramic-matrix Composites

---

Author:
Maria Stratigaki

Supervisor:
Alexandros D. Gotsis

July 2018

Declaration of Authorship

I declare that this Ph.D. thesis and the work presented in it are my own. I confirm that the work of the Dissertation was carried out while in candidature for a Doctoral Degree at the Technical University of Crete and is the result of my independent work. I further state that not any part of this thesis is being submitted for a degree or any other qualification at the Technical University of Crete or any other University. I confirm that where I have consulted the published work of others, this is always clearly attributed, and where I have quoted from the work of others, the source is always given.

Δηλώνω πως η παρούσα Διδακτορική Διατριβή και το έργο που παρουσιάζεται σε αυτήν είναι το αποτέλεσμα ανεξάρτητης προσωπικής μου εργασίας, και επιβεβαιώνω πως διεξήχθη εξ' ολοκλήρου κατά την υποψηφιότητα μου για Διδακτορικό Δίπλωμα στο Πολυτεχνείο Κρήτης. Δηλώνω, επιπρόσθετα, ότι κανένα μέρος αυτής της εργασίας δεν υποβάλλεται για πτυχίο ή άλλο τίτλο στο Πολυτεχνείο Κρήτης ή σε οποιοδήποτε άλλο Πανεπιστήμιο. Επιβεβαιώνω ότι όπου συμβουλεύτηκα το δημοσιευμένο έργο άλλων, αυτό πάντα αποδίδεται σαφώς, και όπου ανέφερα το έργο άλλων, η πηγή δίνεται πάντα.

Διδακτορική Διατριβή
Μαρία Στρατηγάκη
ΑΜ: 2013040351
email: mstratigaki@isc.tuc.gr

Η παρούσα Διδακτορική Διατριβή παρουσιάστηκε δημόσια, εξετάστηκε και εγκρίθηκε από την ακόλουθη επταμελή εξεταστική επιτροπή:

Καθηγητής **Αλέξανδρος Δ. Γκότσης**, Επιβλέπων
Σχολή Μηχανικών Ορυκτών Πόρων
Πολυτεχνείο Κρήτης

Καθηγητής **Κωνσταντίνος Κομνίτσας**
Σχολή Μηχανικών Ορυκτών Πόρων
Πολυτεχνείο Κρήτης

Καθηγητής **Κωνσταντίνος Προβιδάκης**
Σχολή Αρχιτεκτόνων Μηχανικών
Πολυτεχνείο Κρήτης

Επίκουρη Καθηγήτρια **Μαρία Σταυρουλάκη**
Σχολή Αρχιτεκτόνων Μηχανικών
Πολυτεχνείο Κρήτης

Καθηγήτρια **Αθηνά Τσετσέκου**
Σχολή Μηχανικών Μεταλλείων-Μεταλλουργών
Εθνικό Μετσόβιο Πολυτεχνείο

Αναπληρωτής Καθηγητής **Ιωάννης Τσομπανάκης**
Σχολή Μηχανικών Περιβάλλοντος
Πολυτεχνείο Κρήτης

Καθηγητής **Διονύσιος Χριστόπουλος**
Σχολή Μηχανικών Ορυκτών Πόρων
Πολυτεχνείο Κρήτης

5 Ιουλίου 2018

Acknowledgements

I wish to thank my supervisor, Prof. Alexandros D. Gotsis, for giving me the opportunity to work on this Doctoral Dissertation, for his support and guidance throughout the years. I am deeply indebted to Prof. Willi Pabst from the University of Chemistry and Technology, UCT Prague, Czech Republic, and thank him for our collaboration. Special thanks are due to Dr. Eva Gregorová, Vojtěch Nečina, and Tereza Uhlířová from UCT Prague. I deeply thank Michal Hajíček and Dr. Jiří Zýka from UJP PRAHA a.s. for realization of the sintering. Thanks go also to the European Erasmus+ Programme, through which I could finance the time I spent at UCT in Prague. I also thank Dr. Antonis Stratakis from TUC for the X-ray diffraction data, and Mr. Giorgos Apostolakis, TUC, for assistance with the cross-sections of the samples. H.C. Starck GmbH and Sandvik Osprey Ltd are acknowledged for the provision of the tungsten and copper metallic powders. The Thales Research Grant and the scientific coordinator, Prof. Athena Tsetsekou from the National Technical University of Athens, are thanked for providing partial funding. The research for this work has been co-financed by the European Union (European Social Fund - ESF) and Greek national funds through the Operational Program "Education and Lifelong Learning" of the National Strategic Reference Framework (NSRF) - Research Funding Program THALES: Reinforcement of the interdisciplinary and/or interinstitutional research and innovation. The members of the Supervisory Committee are thanked for their thoughtful comments on this dissertation. Ευχαριστώ όλους εκείνους που στάθηκαν δίπλα μου. Την οικογένειά μου για όσα με δίδαξε. Τον Θοδωρή για τη στήριξη και τη κατανόηση.

Μαρία Στρατηγάκη
Ιούλιος 2018
Χανιά

Contents

List of Abbreviations

AMCSD	American Mineralogist Crystal Structure Database
ASTM	American Society for Testing and Materials
CHNS	Carbon/Hydrogen/Nitrogen/Sulfur
CTE	Coefficient of Thermal Expansion
DIN	Deutsche Industrie Norm (German Institute for Standardization)
FFT	Fast Fourier Transform
FGM	Functionally Graded Material
HP	Hot Pressing
IET	Impulse Excitation Technique
ISO	International Organization for Standardization
LPS	Liquid Phase Sintering
OM	Optical Microscopy
PoP	Plaster of Paris
RD	Relative Density
RT	Room Temperature
SPS	Spark Plasma Sintering
SSS	Solid State Sintering
VRH	Voigt Reuss Hirsch
XRD	X-Ray Diffraction

Σύνοψη στα Ελληνικά

Το αντικείμενο και οι στόχοι της παρούσας διδακτορικής διατριβής, καθώς και η δομή του κειμένου παρουσιάζονται στο εισαγωγικό Κεφάλαιο 1.

Εισαγωγή

Τα κεραμικά υλικά χαρακτηρίζονται από εξαιρετικές ιδιότητες όπως χαμηλή πυκνότητα, μεγάλη σκληρότητα και ακαμψία, υψηλό σημείο τήξης, καλή αντοχή σε οξείδωση και διάβρωση, καθώς και σε υψηλές θερμοκρασίες. Οι τεχνολογικές εφαρμογές τους ωστόσο, περιορίζονται δραματικά γεγονός που πηγάζει από την ψαθυρή συμπεριφορά τους η οποία τα καθιστά ευπαθή στην απότομη καταστροφική θραύση. Σε αντίθεση με τα κεραμικά, τα μέταλλα είναι όλκιμα και ελατά υλικά, που χαρακτηρίζονται από υψηλή δυσθραυστότητα με δυνατότητα πλαστικής παραμόρφωσης πριν την θραύση.

Ο συνδυασμός κεραμικών και μεταλλικών υλικών αποσκοπεί στην δημιουργία ενός νέου, σύνθετου υλικού δύο φάσεων με βελτιωμένη αντοχή στην θραύση, αποτελούμενο από μια συνεχή φάση (κεραμική μήτρα) και μια διακριτή φάση (μεταλλικά σωματίδια). Ως σύνθετο ορίζεται το υλικό το οποίο πληροί τις ακόλουθες προϋποθέσεις: (α) μπορεί να κατασκευαστεί, (β) αποτελείται από δύο ή περισσότερες διακριτές φάσεις με διαφορετικές φυσικές ή/και χημικές ιδιότητες που διαχωρίζονται μέσω διεπιφάνειας, και (γ) έχει χαρακτηριστικά που δεν απεικονίζονται μεμονωμένα από τα επιμέρους υλικά που το απαρτίζουν.

Η παρούσα διδακτορική διατριβή είχε ως στόχους την σύνθεση κεραμικών (μη ενισχυμένων) δειγμάτων, καθώς και σύνθετων δειγμάτων κεραμικής μήτρας ενισχυμένων με μεταλλικά εγκλείσματα μέσω κατάλληλης μεθόδου μορφοποίησης, τον χαρακτηρισμό και την μελέτη της μάκρο- και μίκρο-δομής τους, την αξιολόγηση της μηχανικής τους απόκρισης, καθώς και τον συσχετισμό ανάμεσα στην δομή και τις μηχανικές ιδιότητες.

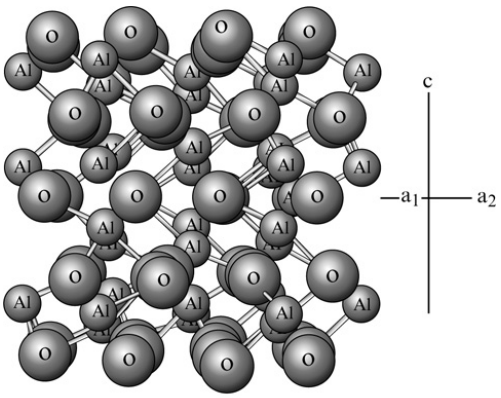

Σχήμα 1: Η δομή του οξειδίου του αργιλίου.

Ως συνεχής κεραμική φάση επιλέχθηκε το οξείδιο του αλουμινίου (οξείδιο του αργιλίου), ευρέως γνωστό ως αλούμινα, με χαρακτηριστικούς δεσμούς ανάμεσα σε άτομα αλουμινίου και οξυγόνου (Σχήμα 1). Η αλούμινα αποτελεί ένα κεραμικό υλικό υψηλής ποιότητας με μοναδικό συνδυασμό φυσικών και μηχανικών ιδιοτήτων, και είναι ένα από τα πιο σημαντικά προηγμένα τεχνολογικά κεραμικά που χρησιμοποιείται σε πλήθος εφαρμογών. Ως μεταλλικά εγκλείσματα επιλέχθηκαν: (α) ο χαλκός λόγω της μεγάλης αντοχής σε θραύση και δυνατότητας παραμόρφωσης καθώς και της σχετικά χαμηλής πυκνότητας, και (β) το βολφράμιο λόγω του χαμηλού συντελεστή θερμικής διαστολής, καθώς και του υψηλού σημείου τήξης.

Η μορφοποίηση των δειγμάτων πραγματοποιήθηκε μέσω της μεθόδου χύτευσης εναιώρησης με γνώμονα την δυνατότητα για καλύτερο στοίβαγμα των σωματιδίων συγκριτικά με τις απλές ξηρές μεθόδους μορφοποίησης, όπως η συμπίεση κόνεων, η οποία συνήθως οδηγεί σε δοκίμια με μη ομοιόμορφη δομή. Παράλληλα η χύτευση αιωρήματος είναι μια μέθοδος με χαμηλές απαιτήσεις σε οργανικά πρόσθετα, συγκριτικά με άλλες υγρές μεθόδους, ενώ η χρήση νερού ως υδατικό μέσο την καθιστά ασφαλή και αποδοτική. Τέλος, η συγκεκριμένη τεχνική επιτρέπει την σύνθεση δοκιμίων σε μια πληθώρα σχημάτων και μεγεθών, εφόσον η κατασκευή των εκμαγείων εκτελείται από τον πειραματιστή.

Συνολικά παρασκευάστηκαν και μελετήθηκαν τέσσερις διαφορετικές συνθέσεις δειγμάτων: (α) καθαρή, μη ενισχυμένη αλούμινα, (β) αλούμινα ενισχυμένη με σωματίδια χαλκού σε πέντε συγκεντρώσεις με κλάσμα όγκου Cu από 1 έως 10%, (γ) αλούμινα ενισχυμένη με σωματίδια βολφραμίου σε τέσσερις συγκεντρώσεις με κλάσμα όγκου W από 0.5 έως 6%, (δ) αλούμινα με συνδυασμό σωματιδίων βολφραμίου/χαλκού σε έξι συγκεντρώσεις με συνολικό κλάσμα όγκου W-Cu από 2 έως 22%.

Το Κεφάλαιο 2 παρέχει πληροφορίες για την δομή και τις ιδιότητες των υλικών που χρησιμοποιήθηκαν, καθώς και βασικές αρχές που διέπουν τα υπό μελέτη σύνθετα υλικά κεραμικής μήτρας με μεταλλική ενίσχυση. Δίνεται η βιβλιογραφική επισκόπηση με επιλεγμένα παραδείγματα που εξετάζονται και συζητούνται ως προς τις μεθόδους σύνθεσης, την δομή και τις μηχανικές τους ιδιότητες, και επιπρόσθετα, αναφέρονται οι μέθοδοι μορφοποίησης που χρησιμοποιούνται για την παρασκευή κεραμικών υλικών ή/και σύνθετων υλικών με κεραμική μήτρα.

Θεωρία και Βιβλιογραφική Επισκόπηση

Πορώδες

Όπως αναφέραμε, τα κεραμικά, γνωστά ήδη από την αρχαιότητα, αποτελούν ένα αναπόσπαστο κομμάτι του ευρύτερου κλάδου των υλικών. Πρόκειται για ανόργανα μη μεταλλικά υλικά με ισχυρούς ιοντικούς ή/και ομοιοπολικούς δεσμούς, τα οποία έχουν υποστεί κατεργασία κάτω από υψηλές θερμοκρασίες, ενώ χαρακτηριστικό τους γνώρισμα αποτελεί το γεγονός πως συχνά δεν επιτυγχάνουν την πλήρη πυκνοποίηση μετά την ολοκλήρωση της πυροσυσσωμάτωσης. Αυτό έχει ως αποτέλεσμα την δημιουργία ενός τελικού δοκιμίου με πυκνότητα χαμηλότερη της θεωρητικής, και συνεπώς την παρουσία κάποιου πορώδους που παραμένει στην δομή, συνήθως της τάξεως του 5%. Το πορώδες μπορεί να είναι ανοιχτό ή κλειστό, υπό μορφή μικρών ή μεγάλων πόρων, μεμονωμένων ή υπό μορφή συστάδας.

Συνεπακόλουθο αυτού του χαρακτηριστικού είναι η μείωση του μέτρου ελαστικότητας και της σκληρότητας, καθώς και άλλων ιδιότητες των υλικών, οι οποίες επηρεάζονται από την παρουσία των πόρων και παρουσιάζουν ελάττωση στις τιμές τους με την αύξηση του πορώδους. Στην βιβλιογραφία υπάρχουν διαθέσιμες εξισώσεις κατάλληλες για να περιγράψουν την ελάττωση των τιμών του μέτρου ελαστικότητας, καθώς και της σκληρότητας, η χρήση των οποίων είναι ιδιαιτέρως σημαντική στην περίπτωση των σύνθετων υλικών, εφόσον συναντώνται σε μια πληθώρα εφαρμογών όπως στην αεροδιαστημική και αεροπορική βιομηχανία, στην βιομηχανία αυτοκινήτων, καθώς και σε προϊόντα καθημερινής χρήσης, στις οποίες είναι απαραίτητο να γνωρίζουμε εκ των προτέρων την συμπεριφορά του κάθε υλικού.

Τεχνικές Μορφοποίησης

Η μορφοποίηση των κεραμικών υλικών ή/και σύνθετων υλικών που απαρτίζονται από κεραμική μήτρα και κάποια φάση ενίσχυσης μπορεί να πραγματοποιηθεί μέσω διαφόρων μεθόδων ή τεχνικών, η κατηγοριοποίηση των οποίων γίνεται με βάση τις απαιτήσεις τους σε κάποιο υδατικό μέσο (συνήθως νερό). Με βάση αυτή την απαίτηση, προκύπτουν οι ακόλουθες κατηγορίες:

Ξηρές Μέθοδοι κατά τις οποίες δεν απαιτείται η προσθήκη νερού. Η ξηρή μονοαξονική συμπίεση είναι η πιο κοινή μέθοδος που χρησιμοποιείται για την σύνθεση δειγμάτων με σχετικά απλά σχήματα. Αποτελεί μια γρήγορη και απλή μέθοδο μορφοποίησης μέσω της συμπίεσης των υλικών (σε μορφή κόνεων) μέσα σε ένα καλούπι, όμως συχνά οδηγεί σε ανισοτροπία του δοκιμίου λόγω της μη ομοιόμορφης συμπίεσης όλων των σημείων του δείγματος. Εναλλακτικές τεχνικές αποτελούν: η ισοστατική συμπίεση για την σύνθεση δειγμάτων με ομοιογενή δομή και αρκετά υψηλότερες πυκνότητες ή η συμπίεση εν θερμώ με την ταυτόχρονη εφαρμογή υψηλής πίεσης και υψηλής θερμοκρασίας μέσω της οποίας τα δείγματα πλησιάζουν τις θεωρητικές πυκνότητες, έχει όμως υψηλό κόστος και περιορισμένη παραγωγικότητα.

Πλαστικές Μέθοδοι οι οποίες χρησιμοποιούνται για τον σχηματισμό και την παραγωγή τελικών προϊόντων υπό μορφή ράβδων ή σωλήνων. Η πιο κοινή μέθοδος αυτής της κατηγορίας είναι η εξώθηση η οποία έχει μεγάλες απαιτήσεις σε νερό καθώς και σε οργανικά πρόσθετα συστατικά τα οποία επιτρέπουν την δημιουργία μιας εύπλαστης μάζας η οποία θα μορφοποιηθεί (υπό πίεση) στο κατάλληλο σχήμα.

Ημι-υγρές Μέθοδοι κατά τις οποίες απαιτείται μεγάλη ποσότητα υδατικού μέσου (νερού) ώστε να σχηματιστεί ένα αιώρημα. Η πιο χαρακτηριστική τεχνική αυτής της κατηγορίας είναι η χύτευση εναιώρησης, για την χρήση της οποίας αρχικά απαιτείται η προετοιμασία κατάλληλων πορωδών εκμαγείων μέσα στα οποία θα γίνει η έγχυση του αιωρήματος και αυτά θα απορροφήσουν την περίσσεια νερού ώστε να σχηματιστεί ένα ωμό δείγμα μετά την απομάκρυνση από το καλούπι (Σχήμα 2).

Χύτευση Εναιώρησης

Η χύτευση αιωρήματος διακρίνεται: (α) στην στερεή χύτευση, κατά την οποία το αιώρημα προστίθεται συνεχώς στο καλούπι έως ότου σχηματιστεί ένα συμπαγές δοκίμιο, και (β) στην χύτευση με απόχυση, κατά την οποία η περίσσεια του αιωρήματος απομακρύνεται από το καλούπι ώστε να προκύψει τελικά ένα κοίλο δείγμα.

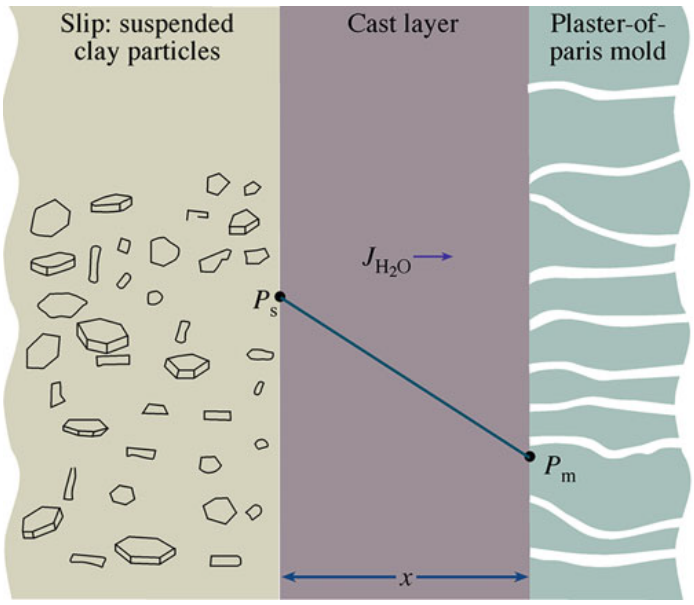

Σχήμα 2: Απορρόφηση νερού από πορώδες εκμαγείο κατά την χύτευση εναιώρησης.

Όπως αναφέραμε πρωτύτερα, η συγκεκριμένη μέθοδος προτιμάται λόγω χαμηλού κόστους, και καλύτερης ομοιογένειας τελικού προϊόντος συγκριτικά με απλές τεχνικές συμπίεσης. Επιπλέον πλεονεκτήματα της τεχνικής περιλαμβάνουν την δυνατότητα παρασκευής δοκιμίων με πολύπλοκα σχήματα και μεγέθη, καθώς και οι χαμηλότερες απαιτήσεις σε οργανικά συστατικά έναντι άλλων μεθόδων που κάνουν χρήση υδατικού μέσου. Μειονεκτήματα της τεχνικής αποτελούν (αρχικά) η ανάγκη να παρασκευαστούν τα καλούπια, οι χρονικές απαιτήσεις για χύτευση και ξήρανση των δοκιμίων, καθώς και οι η ανάγκη επαρκούς αφυδάτωσης των καλουπιών ανάμεσα σε δύο διαδοχικές χυτεύσεις. Επιπρόσθετα η φθορά, λόγω χρήσης, των εκμαγείων απαιτεί την εκ νέου δημιουργία τους.

Ξήρανση & Πυροσυσσωμάτωση

Μετά την ολοκλήρωση του σταδίου της μορφοποίησης για την μετατροπή των σωματιδίων σκόνης σε ένα υλικό με επιθυμητό σχήμα, είναι απαραίτητο να πραγματοποιηθούν τα εξής βήματα: (α) η ξήρανση, (β) η απομάκρυνση του οργανικού συστατικού, και (γ) η πυροσυσσωμάτωση, τα οποία θα επιτρέψουν την μετατροπή των (ωμών) δειγμάτων σε ένα τελικό πυροσυσσωματωμένο προϊόν.

Η ξήρανση αποτελεί ένα σημαντικό στάδιο της διαδικασίας και αφορά στην απομάκρυνση του νερού ή/και της υγρασίας από το δείγμα. Απαιτείται ιδιαίτερη προσοχή κατά το στάδιο της ξήρανσης ώστε να αποφευχθούν (ή να περιοριστούν στο ελάχιστο) οι επιφανειακές ρωγμές που είναι δυνατό να δημιουργηθούν

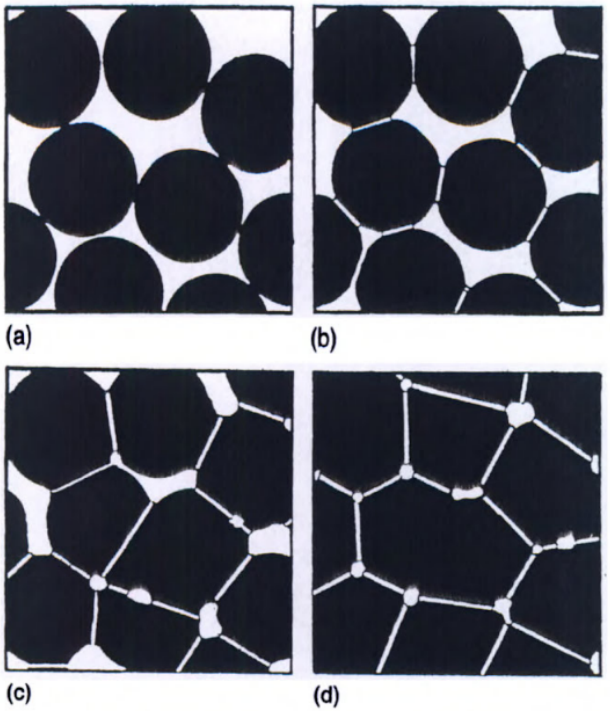

Σχήμα 3: Η πρόοδος του φαινομένου της πυροσυσσωμάτωσης.

λόγω συρρίκνωσης του δείγματος. Ακολουθεί το στάδιο της απομάκρυνσης του οργανικού συστατικού σε θερμοκρασία χαμηλότερη από αυτή της έψησης (συνήθως γύρω στους $400\,^{\circ}\mathrm{C}$ με $600\,^{\circ}\mathrm{C}$ όπου αποδομείται η οργανική ένωση), και τέλος αυτό της πυροσυσσωμάτωσης το οποίο στοχεύει στην αύξηση της πυκνότητας του δοκιμίου και μείωση του πορώδους.

Κατά την διάρκεια της πυροσυσσωμάτωσης λαμβάνουν χώρα διάφορες χημικές αντιδράσεις οι οποίες επιφέρουν τα ιδιαίτερα χαρακτηριστικά στο κεραμικό υλικό και του προσδίδουν τις επιθυμητές ιδιότητες, καθώς και την απαιτούμενη μικροδομή. Η έψηση περιγράφει την μετατροπή μιας δομής σε ένα συμπαγές σώμα μέσω θέρμανσης και επηρεάζεται από πολλές παραμέτρους όπως τα χαρακτηριστικά των πρώτων υλών (μέγεθος και σχήμα, βαθμός συσσωματωμάτων), και τα χαρακτηριστικά της διαδικασίας όπως η θερμοκρασία και ο χρόνος έψησης, η πίεση και η ατμόσφαιρα, οι ρυθμοί θέρμανσης και ψύξης.

Η πυροσυσσωμάτωση (σε στερεή κατάσταση) πραγματοποιείται μέσω διαφόρων μηχανισμών είτε από την επιφάνεια είτε από το εσωτερικό του δείγματος και διακρίνεται σε στάδια που περιλαμβάνουν: την ανάπτυξη 'λαιμού' μεταξύ δυο κόκκων στο αρχικό στάδιο και κλείσιμο των πόρων με σχετικές πυκνότητες 60-65%, το ενδιάμεσο στάδιο με σχετικές πυκνότητες 65-90% που αφορά στον σχηματισμό των ορίων των κόκκων στην διεπαφή τους, και το τελικό στάδιο που οι πυκνότητες πλησιάζουν τις θεωρητικές τιμές (Σχήμα 3).

Η έψηση των κεραμικών υλικών συνήθως εκτελείται σε ατμόσφαιρα οξυγόνου (αέρα), ενώ παρουσία μεταλλικών υλικών είναι απαραίτητη η χρήση αναγωγικής (υδρογόνου) ή αδρανούς (αζώτου) ατμόσφαιρας προς αποφυγή δημιουργίας οξειδίων. Τελικό στάδιο είναι ο έλεγχος του προϊόντος και ο χαρακτηρισμός του ως προς τις ιδιότητες (φυσικές, μηχανικές, χημικές, θερμικές).

Διάδοση Ρωγμής και άλλες Παρατηρήσεις

Όπως αναφέραμε πρωτύτερα, η ψαθυρή θραύση των κεραμικών υλικών οφείλεται στα μικρά ποσοστά ενέργειας που απαιτούνται ώστε αρχικά να δημιουργηθεί η ρωγμή και έπειτα να διαδοθεί μέσα στο υλικό έως ότου επέλθει η θραύση και η οριστική του αστοχία. Η διασπορά των μεταλλικών σωματιδίων μέσα στην κεραμική μήτρα στοχεύει στην βελτίωση της αντοχής του υλικού μέσω της ενεργοποίησης διαφόρων μηχανισμών οι οποίοι δρουν είτε μεμονωμένα είτε συνεργατικά.

Τα μεταλλικά εγκλείσματα αλληλεπιδρούν με την ρωγμή που διαδίδεται μέσα στην κεραμική μήτρα, και αυτό μπορεί να επιτευχθεί μέσω δύο βασικών μηχανισμών: (α) την γεφύρωση της ρωγμής μέσω πλαστικής παραμόρφωσης των σωματιδίων, ή (β) άλλης μορφής αλληλεπίδραση όπως η εκτροπή της πορείας της ρωγμής, η διάδοση της διαμέσου της διεπιφάνειας ή η περαιτέρω διακλάδωση της στο υλικό της μήτρας.

Δεν μπορεί να παραβλεφθεί φυσικά το γεγονός πως η διασπορά των μεταλλικών σωματιδίων μέσα στην κεραμική μήτρα, πέραν της αυξημένης αντοχής που προσδίδει στο τελικό σύνθετο προϊόν, συχνά επιφέρει και την δημιουργία τάσεων λόγω των μεγάλων διαφορών που υπάρχουν ανάμεσα στις δύο φάσεις, τόσο ως προς το μέτρο ελαστικότητας όσο και ως προς τον συντελεστή θερμικής διαστολής. Συνεπώς, κατά την διάρκεια της ψύξης, μετά το τέλος της πυροσυσσωμάτωσης, οι διαφορές αυτές ανάμεσα στα δύο υλικά είναι δυνατό να προκαλέσουν τάσεις και ίσως μικρο-ρηγματώσεις.

Επιπλέον, η διασκόρπιση των μεταλλικών σωματιδίων στην κεραμική μήτρα είναι δυνατό να προκαλέσει και άλλες αλλαγές όπως ελάττωση της τελικής πυκνότητας, αύξηση του πορώδους, δημιουργία συσσωματωμάτων, ασθενή διεπιφάνεια ανάμεσα στις φάσεις. Αυτό έχει ως αποτέλεσμα η ενίσχυση του κεραμικού υλικού με μεταλλικά εγκλείσματα να συντελεί στην αύξηση της αντοχής σε θραύση αλλά ταυτόχρονα η διασπορά μιας φάσης με μικρότερη σκληρότητα καθώς και μικρότερο μέτρο ελαστικότητας από αυτό του κεραμικού να επιφέρει μείωση των τιμών των συγκεκριμένων μηχανικών ιδιοτήτων.

Η πειραματική διαδικασία που ακολουθήθηκε στην παρούσα διατριβή για την σύνθεση των δειγμάτων περιγράφεται στο Κεφάλαιο 3. Επιπρόσθετα αναφέρονται οι μέθοδοι χαρακτηρισμού που χρησιμοποιήθηκαν για τις πρώτες ύλες και τα δείγματα, καθώς και οι τεχνικές μέτρησης των μηχανικών ιδιοτήτων των τελικών δοκιμίων.

Πειραματική Μέθοδος

Στην παρούσα εργασία, η σύνθεση των δειγμάτων έγινε μέσω της μεθόδου χύτευσης αιωρήματος. Τα υλικά που χρησιμοποιήθηκαν για την παρασκευή των δοκιμίων ήταν υψηλής καθαρότητας, σε μορφή σκόνης, και περιελάμβαναν το οξείδιο του αλουμινίου που χρησιμοποιήθηκε για την σύσταση της συνεχούς φάση (κεραμική μήτρα), και μεταλλικές σκόνες χαλκού και βολφραμίου που χρησιμοποιήθηκαν ως μέσο ενίσχυσης (μεταλλικά εγκλείσματα). Επιπρόσθετα, χρησιμοποιήθηκε απιονισμένο νερό, καθώς και μικρή ποσότητα ενός οργανικού παράγοντα για την σταθεροποίηση του αιωρήματος.

Η τεχνική αυτή καθιστά απαραίτητη την δημιουργία κατάλληλου εκμαγείου μέσα στο οποίο θα γίνει η έγχυση του αιωρήματος και η μορφοποίηση του ωμού δείγματος. Προετοιμάστηκαν, συνεπώς, καλούπια για να δημιουργηθούν κυλινδρικά δείγματα σε σχήμα ράβδου με διαστάσεις περίπου $5\,\mathrm{mm}$ σε διάμετρο και $50\,\mathrm{mm}$ σε μήκος. Για την προετοιμασία των καλουπιών χρησιμοποιήθηκε, σε κατάλληλη αναλογία, νερό και γύψος Παρισιού. Το μίγμα ομογενοποιήθηκε με δια χειρός ανάμιξη, και έπειτα έγινε έγχυση σε πρωτότυπο εκμαγείο. Αντίστοιχη διαδικασία ακολουθήθηκε για την παραγωγή του δεύτερου τμήματος του εκμαγείου. Τα καλούπια παρέμειναν σε θερμοκρασία δωματίου για $72\,\mathrm{h}$ ώστε να στεγνώσουν πλήρως.

Μετά την απομάκρυνση του δείγματος από το καλούπι, αρχικά πραγματοποιήθηκε η ξήρανση του σε θερμοκρασία δωματίου για $24\,\mathrm{h}$, και έπειτα σταδιακά σε ξηραντήρα από τους $40\,^{\circ}\mathrm{C}$ έως τους $110\,^{\circ}\mathrm{C}$ έως ότου παρουσιάσει σταθερό βάρος. Η απομάκρυνση του οργανικού παράγοντα έγινε σε ατμόσφαιρα υδρογόνου στους $600\,^{\circ}\mathrm{C}$ με ρυθμό θέρμανσης $1\,^{\circ}\mathrm{C}/\,\mathrm{min}$ και παραμονή σε αυτή την θερμοκρασία για $2\,\mathrm{h}$. Τέλος, η πυροσυσσωμάτωση έγινε υπό αναγωγική ατμόσφαιρα στους $1500\,^{\circ}\mathrm{C}$ με ρυθμό θέρμανσης $2\,^{\circ}\mathrm{C}/\,\mathrm{min}$ και παραμονή στην θερμοκρασία έψησης για $2\,\mathrm{h}$, ενώ ο ρυθμός ψύξης έως την θερμοκρασία δωματίου ήταν $5\,^{\circ}\mathrm{C}/\,\mathrm{min}$.

Στο Κεφάλαιο 4 παρουσιάζονται τα χαρακτηριστικά των κόνεων όπως προκύπτουν ως αποτέλεσμα διαφόρων τεχνικών χαρακτηρισμού που περιλαμβάνουν την κρυσταλλική φάση του κάθε υλικού μέσω της περίθλασης ακτίνων Χ, το μέγεθος των σωματιδίων και την κατανομή μεγεθών δια της περίθλασης με ακτίνες λέιζερ, καθώς και την γενικότερη μορφολογία των σωματιδίων με την χρήση οπτικού μικροσκοπίου.

Αποτελέσματα

Χαρακτηρισμός αρχικών υλικών

Οι σκόνες μελετήθηκαν μέσω περίθλασης ακτίνων Χ, μιας μη καταστρεπτικής μεθόδου κατάλληλης για κρυσταλλικά υλικά σε μορφή πούδρας, σε ένα εύρος γωνιών από 10° έως 80°. Τα φάσματα αναλύθηκαν και οι χαρακτηριστικές κορυφές του κάθε υλικού ταυτοποιήθηκαν με αντίστοιχες τιμές από βάση δεδομένων, επιβεβαιώνοντας την σύσταση, την δομή, και την καθαρότητα τους. Η αλούμινα παρουσιάζει μια πληθώρα κορυφών, ενώ στο υπό εξέταση εύρος γωνιών οι μεταλλικές σκόνες εμφανίζουν τρεις χαρακτηριστικές κορυφές.

Επιπρόσθετα, χρησιμοποιήθηκε η περίθλαση ακτίνων λέιζερ για την κοκκομετρική ανάλυση καθώς και τον προσδιορισμό της κατανομής των μεγεθών των σωματιδίων των υλικών. Τα αποτελέσματα συνοψίζονται ως εξής: μέσο μέγεθος για την αλούμινα 0.7 μm, με το 90% των σωματιδίων να έχουν μέγεθος μικρότερο από 2 μm, μέσο μέγεθος για τον χαλκό περίπου 17 μm, ενώ για το βολφράμιο το μέσο μέγεθος είναι κάτω από 1 μm. Συνολικά, οι τιμές συμφωνούν πλήρως με τα δεδομένα των κατασκευαστών.

Τέλος, ελήφθησαν αντιπροσωπευτικές εικόνες με την χρήση οπτικού μικροσκοπίου, που αποσκοπούσαν στην εκτίμηση κυρίως του σχήματος των σωματιδίων των μεταλλικών υλικών. Από αυτές παρατηρήθηκε το σχεδόν σφαιρικό σχήμα των σωματιδίων του χαλκού με απομονωμένα σωματίδια και ένα εύρος μεγεθών, σε αντίθεση με τα ακανόνιστης μορφολογίας σωματίδια βολφραμίου τα οποία παρουσίασαν αρκετά συσσωματώματα.

Το Κεφάλαιο 5 αφορά στον χαρακτηρισμό των δειγμάτων και στην ανάλυση της δομής τους. Τα αποτελέσματα περιλαμβάνουν μακροσκοπικές παρατηρήσεις, καθώς και μετρήσεις που αφορούν στον προσδιορισμό της σύστασης, στην πυκνότητα, στο πορώδες καθώς και στην ποσοστιαία συρρίκνωση των ραβδόμορφων κυλινδρικών δοκιμίων. Επίσης μελετάται η διασπορά των σωματιδίων στην κεραμική μήτρα καθώς και τα μορφολογικά χαρακτηριστικά τους μετά το πέρας της πυροσυσσωμάτωσης.

Αποτελέσματα

Χαρακτηρισμός δειγμάτων

Αρχικά τα δείγματα εξετάστηκαν μακροσκοπικά (παρατήρηση δια γυμνού οφθαλμού) όπου επιβεβαιώθηκε πως έχει διατηρηθεί το κυλινδρικό ραβδόμορφο σχήμα τους και δεν έχει επέλθει παραμόρφωση λόγω γεωμετρίας των δοκιμίων ή άλλη ατέλεια όπως ρωγμές ή φυσαλίδες αέρα στην επιφάνεια. Επίσης παρατηρήθηκε διαβάθμιση του χρώματος με αύξηση του ποσοστού της μεταλλικής ενίσχυσης, ενώ τα δείγματα που περιείχαν χαλκό παρουσίασαν μια δομή πυρήνα-επιφάνειας με χαρακτηριστικό το λευκό χρώμα της επιφάνειας λόγω περίσσειας αλούμινας και το κόκκινο στο εσωτερικό λόγω περίσσειας χαλκού.

Η περίθλαση ακτίνων Χ πραγματοποιήθηκε για τα ωμά και τα ψημένα δείγματα ώστε να γίνει ταυτοποίηση των φάσεων και να ελεγχθεί η πιθανή ύπαρξη οξειδίων. Τα δείγματα χαρακτηρίστηκαν ως προς την πυκνότητα και το πορώδες αξιοποιώντας την Αρχή του Αρχιμήδη. Η θεωρητική πυκνότητα των δειγμάτων υπολογίστηκε από τα γνωστά κατ όγκο ποσοστά καθώς και τις πυκνότητες της αλούμινας, του χαλκού, και του βολφραμίου. Οι σχετικές πυκνότητες πριν και μετά την πυροσυσσωμάτωση υπολογίστηκαν συγκρίνοντας τα πειραματικά δεδομένα με τις θεωρητικές τιμές, ενώ το ανοικτό πορώδες αφορά στα δείγματα μετά την πυροσυσσωμάτωση.

Μετά την ολοκλήρωση της μελέτης της μηχανικής απόκρισης των δοκιμίων ελήφθησαν θραύσματα τα οποία εμποτίστηκαν σε ρητίνη και προετοιμάστηκαν κατάλληλα μέσω λείανσης και στίλβωσης ώστε να προκύψουν στιλπνές τομές. Η παρουσία των σωματιδίων εξετάστηκε μέσω οπτικού μικροσκοπίου όπου επιβεβαιώθηκε η ομοιογενής διασπορά τους στην μήτρα με σφαιρικά σωματίδια χαλκού και συσσωματωμένα σωματίδια βολφραμίου.

Σχήμα 4: Φάσματα περίθλασης ακτίνων Χ για όλα τα δείγματα πριν και μετά την πυροσυσσωμάτωση. Τα φάσματα καταδεικνύουν την παρουσία μόνο καθαρών φάσεων που αντιστοιχούν στην αλούμινα, το χαλκό και το βολφράμιο, εφόσον οι χαρακτηριστικές κορυφές του κάθε υλικού ταυτοποιήθηκαν με αντίστοιχη βάση δεδομένων. Η πυροσυσσωμάτωση υπό αναγωγική ατμόσφαιρα υδρογόνου δεν επέτρεψε την δημιουργία οξειδίων στα δείγματα, τα οποία συχνά δυσχεραίνουν την μηχανική απόκριση των υλικών. Επιπρόσθετα παρατηρούμε την αύξηση της έντασης της κορυφής καθώς αυξάνεται το κλάσμα όγκου της μεταλλικής φάσης.

Σχήμα 5: Σχετική πυκνότητα των δειγμάτων πριν και μετά την πυροσυσσωμάτωση ως συνάρτηση του κλάσματος όγκου της μεταλλικής φάσης. Η μεγαλύτερη πυκνότητα στα ωμά δείγματα καταγράφηκε για τα δοκίμια της αλούμινας (περίπου 60%) ενώ οι τιμές για τα σύνθετα δείγματα κυμαίνονται στο 53-56% για εκείνα που περιέχουν χαλκού, 55-60% για αυτά που περιέχουν βολφράμιο, και 57-63% για τα δείγματα με βολφράμιο/χαλκό. Οι τιμές στα τελικά δείγματα παρουσιάζουν μείωση με αύξηση της μεταλλικής φάσης που σχετίζεται με την κακή διαβροχή του χαλκού στην μήτρα της αλούμινας, και τα συσσωματώματα του βολφραμίου καθώς και την απουσία πίεσης κατά την έψηση που δεν επιτρέπει την πυκνοποίηση των δειγμάτων μέχρι την θεωρητική πυκνότητα.

Σχήμα 6: Ανοικτό πορώδες των δειγμάτων μετά την πυροσυσσωμάτωση όπως υπολογίσθηκε με την μέθοδο του Αρχιμήδη. Παρατηρούμε πως το πορώδες είναι μηδαμινό για τα δοκίμια που περιέχουν βολφράμιο (<0.5%) και ανεξάρτητο από το κλάσμα όγκου, ενώ οι τιμές αυξάνονται με την αύξηση του ποσοστού μεταλλικής φάσης για τα δοκίμια που περιέχουν χαλκό, το οποίο σχετίζεται με το γεγονός πως μια μικρή ποσότητα χάνεται λόγω της πυροσυσσωμάτωσης που πραγματοποιείται σε θερμοκρασία πάνω από το σημείο τήξης του χαλκού. Τα ποσοστά για το ανοικτό πορώδες παραμένουν χαμηλά (περίπου 1%) για τα δείγματα που περιέχουν μικρά ποσοστά χαλκού, ενώ αύξηση (> 2%) εμφανίζεται για δείγματα με μεγαλύτερα ποσοστά (>10 vol.% Cu) δηλ. 10Cu, 10Cu-05W, 10Cu-5W, 20Cu-2W.

Στο Κεφάλαιο 6 παρουσιάζονται τα πειραματικά αποτελέσματα της μηχανικής απόκρισης των δειγμάτων που περιλαμβάνουν μετρήσεις για τον προσδιορισμό του μέτρου ελαστικότητας, της μικροσκληρότητας κατά Vickers, και της αντοχής σε κρούση. Τα δεδομένα που προκύπτουν για τα σύνθετα δοκίμια συγκρίνονται με εκείνα της μη-ενισχυμένης μήτρας ώστε να γίνει εκτίμηση της συνεισφοράς της μεταλλικής ενίσχυσης. Επιπρόσθετα τα αποτελέσματα συγκρίνονται με βιβλιογραφικά δεδομένα για αντίστοιχα σύνθετα υλικά αλούμινας με μεταλλικά εγκλείσματα, ενώ παράλληλα συζητείται η σχέση ανάμεσα στην δομή και τις μηχανικές τους ιδιότητες των δοκιμίων.

Αποτελέσματα

Μηχανικές Ιδιότητες

Το μέτρο ελαστικότητας, η σκληρότητα, και η αντοχή σε δοκιμή κρούσης αποτελούν σημαντικές μηχανικές ιδιότητες των υλικών. Οι δύο πρώτες ιδιότητες αποτελούν χαρακτηριστικά γνωρίσματα των κεραμικών υλικών με ιδιαίτερα υψηλές τιμές, ενώ η τελευταία αποτελεί ιδιότητα που απαιτεί βελτίωση.

Το μέτρο ελαστικότητας περιγράφει την δυσκαμψία ενός υλικού, συνεπώς όσο μεγαλύτερη είναι η τιμή του, τόσο πιο δύσκαμπτο είναι το υλικό. Η σκληρότητα αποτελεί ένα μέτρο αντίστασης του υλικού σε μια περιορισμένη, τοπική παραμόρφωση, επομένως όσο πιο μαλακό είναι το υλικό τόσο πιο μικρός θα είναι και ο ενδεικτικός αριθμός σκληρότητας. Τέλος, η αντοχή σε δοκιμή κρούσης μετρά την ικανότητα ενός υλικού να απορροφά ενέργεια έως την θραύση του.

Παρατηρούμε στα επόμενα σχήματα πως τα πειραματικά δεδομένα του μέτρου ελαστικότητας και της σκληρότητας είναι σε συμφωνία με τις θεωρητικές τιμές που προκύπτουν εφαρμόζοντας τόσο εξισώσεις για το πορώδες της μήτρας, καθώς και κατάλληλα μοντέλα που προβλέπουν την συνεισφορά των δύο ή τριών φάσεων στην μηχανική συμπεριφορά του υλικού. Αντίθετα, η απόκριση στην δοκιμή κρούσης δεν παρουσιάζει γραμμική συμπεριφορά με το κλάσμα όγκου.

Σχήμα 7: Μέτρο ελαστικότητας: τα πειραματικά δεδομένα συγκρίνονται με τις θεωρητικές εξισώσεις οι οποίες διορθώνουν για το πορώδες και την συνεισφορά της μεταλλικής φάσης. Συνολικά παρατηρείται μείωση στις τιμές των πειραματικών μετρήσεων καθώς αυξάνεται το κλάσμα όγκου της μεταλλικής φάσης, μια συμπεριφορά αναμενόμενη λόγω της διασποράς ενός μαλακού μετάλλου με πολύ χαμηλότερο μέτρο ελαστικότητας από εκείνο της μήτρας (δείγματα που περιέχουν χαλκό). Στα δοκίμια που περιέχουν βολφράμιο αρχικά παρατηρείται μια μικρή αύξηση των τιμών (μέτρο ελαστικότητας βολφραμίου παραπλήσιο της αλούμινας), ενώ στα δείγματα τριών φάσεων η ελάττωση οφείλεται στις μεγάλες συγκεντρώσεις χαλκού.

Σχήμα 8: Μικροσκληρότητα Vickers: τα πειραματικά δεδομένα των μετρήσεων συγκρίνονται με θεωρητική εξίσωση που προβλέπει την μείωση της σκληρότητας λόγω της διασποράς της δεύτερης φάσης, καθώς και λόγω της ύπαρξης πόρων στα δοκίμια. Η συμπεριφορά των δοκιμίων είναι παρόμοια εφόσον η σκληρότητα των σύνθετων δειγμάτων ελαττώνεται με την αύξηση του κλάσματος όγκου της μεταλλικής φάσης, κυρίως για τα δείγματα που περιέχουν μεγάλα ποσοστά ενίσχυσης. Σε αντίθεση με το μέτρο ελαστικότητας, η ελάττωση των τιμών δεν επηρεάζεται σημαντικά από την μεταλλική φάση, εφόσον, είτε αυτή είναι χαλκός είτε βολφράμιο, η σκληρότητά τους είναι πολύ μικρότερη από εκείνη της κεραμικής μήτρας.

Σχήμα 9: Αντοχή σε κρούση: Σε αντίθεση με το μέτρο ελαστικότητας και την σκληρότητα, η αντοχή σε θραύση αποτελεί μια μηχανική ιδιότητα που δεν παρουσιάζει ακριβή εξάρτηση από την πυκνότητα των δειγμάτων ή το κλάσμα όγκου της δεύτερης φάσης, γεγονός που επιβεβαιώνει την πολυπλοκότητα της καθώς και την εξάρτησή της από μια πληθώρα παραμέτρων. Παρατηρούμε πως τα δείγματα που περιέχουν χαλκό εμφανίζουν βελτιωμένη μηχανική συμπεριφορά ως προς την αντοχή για χαμηλά ποσοστά χαλκού, ενώ η περαιτέρω αύξηση έχεις ως αποτέλεσμα την ελάττωση της αντοχής των δοκιμίων. Τα δείγματα που περιέχουν βολφράμιο εμφανίζουν μόνο μια μικρή αύξηση αρχικά, ενώ τα δοκίμια τριών φάσεων παρουσιάζουν μια πιο πολύπλοκη μηχανική συμπεριφορά.

Το Κεφάλαιο 7 ολοκληρώνει την διδακτορική διατριβή συνοψίζοντας τα αποτελέσματα και τα συμπεράσματα. Συζητούνται οι στόχοι που επιτεύχθηκαν καθώς και πιθανά θέματα και προτάσεις για περαιτέρω έρευνα.

Συμπεράσματα

Η παρούσα διδακτορική διατριβή αφορούσε στην μελέτη σύνθετων υλικών κεραμικής μήτρας ενισχυμένης με μεταλλικά σωματίδια. Η έρευνα περιλαμβάνει την σύνθεση των υλικών, τον χαρακτηρισμό ως προς την δομή τους, την απόκριση της μηχανικής τους συμπεριφοράς λόγω της διαβάθμισης του κλάσματος όγκου της μεταλλικής φάσης, καθώς και την μελέτη των σχέσεων ανάμεσα στην δομή και τις μηχανικές ιδιότητες. Μη ενισχυμένα δείγματα, αποτελούμενα από οξείδιο του αλουμινίου, παρασκευάστηκαν με την ίδια μέθοδο, ώστε να προκύψει σύγκριση και να αξιολογηθεί η συνεισφορά της μεταλλικής φάσης.

Οι συνθέσεις που μελετήθηκαν ποικίλλουν σημαντικά λόγω των ιδιοτήτων των μετάλλων που χρησιμοποιήθηκαν για την διασπορά τους ως εγκλείσματα στην μήτρα αλούμινας. Οι ιδιότητες αυτές είναι μηχανικές (πυκνότητα, ελαστικότητα, και αντοχή), καθώς και θερμικές (σημείο τήξης, και συντελεστής θερμικής διαστολής), και οι διαφορές τους οφείλονται στον μεταλλικό δεσμό του κάθε στοιχείου: ο ασθενής δεσμός του χαλκού επιτρέπει την παραμόρφωσή του, όμως επιφέρει και ένα χαμηλό σημείο τήξης καθώς και έναν υψηλό συντελεστή θερμικής διαστολής, ενώ ο ισχυρός δεσμός που χαρακτηρίζει το βολφράμιο είναι αυτός που το καθιστά σκληρό και άκαμπτο ενώ παράλληλα επιφέρει ένα υψηλό σημείο τήξης και ένα χαμηλό συντελεστή διαστολής.

Στην παρούσα εργασία παρουσιάσαμε πως, παρ' όλες τις διαφορές, η μέθοδος που ακολουθήσαμε επιτρέπει την δημιουργία σύνθετων υλικών με ενισχυμένη μηχανική απόκριση αντοχής και διατήρηση των άλλων μηχανικών ιδιοτήτων σε καλά επίπεδα. Σύνθετα δείγματα μετάλλου/κεραμικού αποτελούμενα από Al_2O_3 και σωματίδια Cu, W, και W-Cu παρασκευάστηκαν επιτυχώς μέσω της μεθόδου χύτευσης εναιώρησης και πυροσυσσωμάτωσης υπό αναγωγική ατμόσφαιρα υδρογόνου.

Τα δείγματα παρουσίασαν ομοιογενή δομή, υψηλή πυκνότητα και χαμηλό πορώδες. Η μηχανική τους συμπεριφορά μελετήθηκε μέσω κατάλληλων μετρήσεων για την εκτίμηση της ελαστικότητας, της σκληρότητας και της αντοχής από τις οποίες προκύπτει πως (κυρίως) τα μικρά ποσοστά μεταλλικής ενίσχυσης μπορούν να βελτιώσουν την αντοχή σε θραύση αλλά όχι εις βάρος της υψηλής σκληρότητας και ελαστικότητας που διακατέχουν την κεραμική μήτρα.

Σχήμα 4

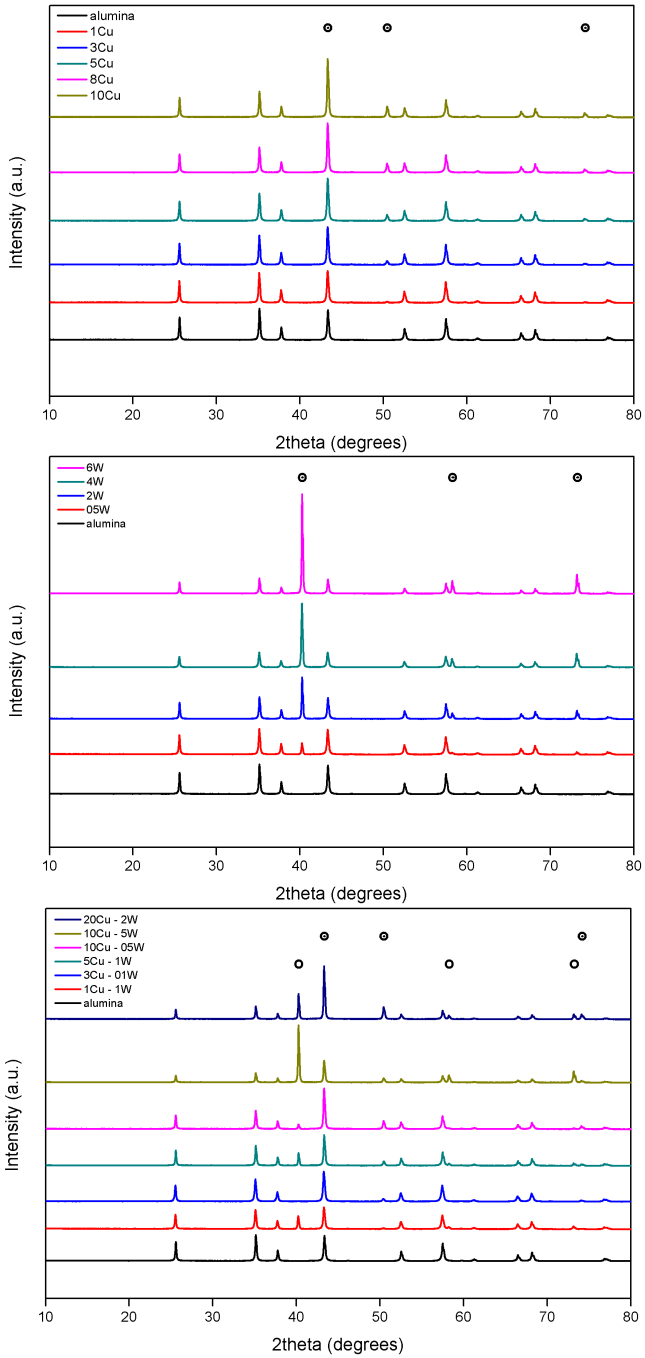
alumina
1Cu
3Cu
5Cu
8Cu
10Cu
Intensity (a.u.)
10
20
30
40
50
60
70
80
2theta (degrees)
6W
4W
2W
05W
alumina
Intensity (a.u.)
2theta (degrees)
20Cu - 2W
10Cu - 5W
10Cu - 05W
5Cu - 1W
3Cu - 01W
1Cu - 1W
alumina
Intensity (a.u.)
2theta (degrees)

Σχήμα 5

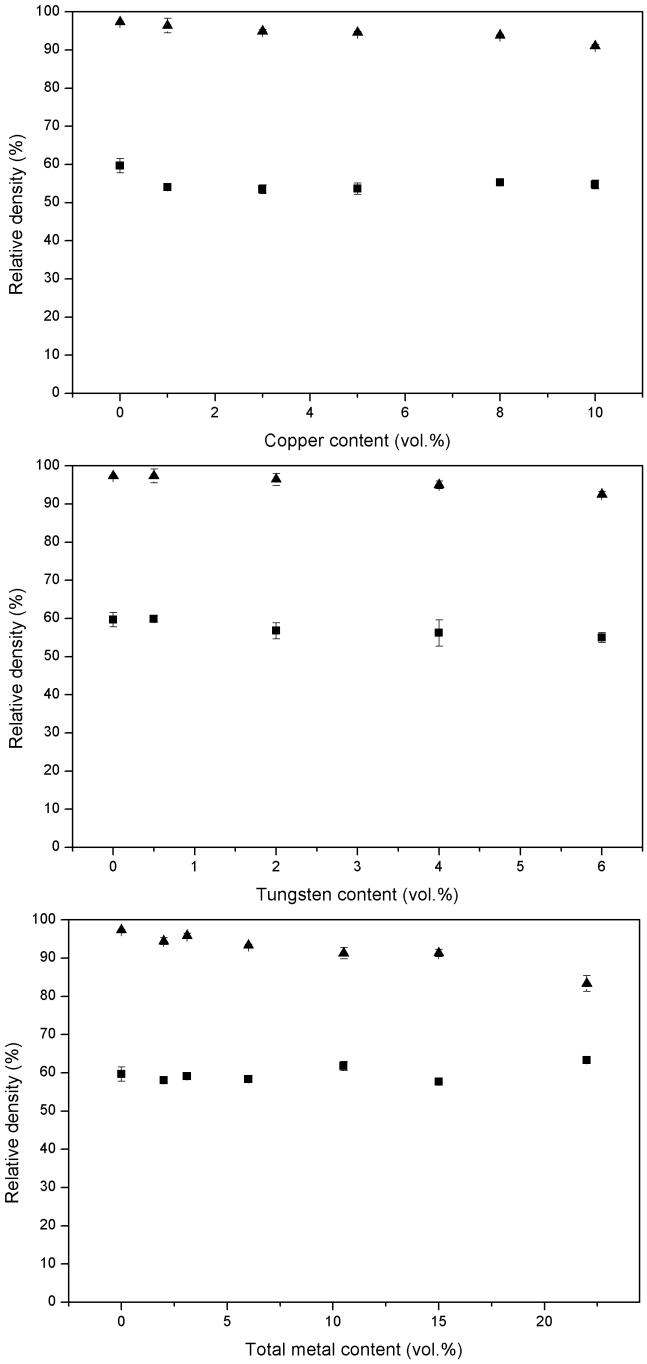
Relative density (%)
Copper content (vol.%)
Relative density (%)
Tungsten content (vol.%)
Relative density (%)
Total metal content (vol.%)

Σχήμα 6

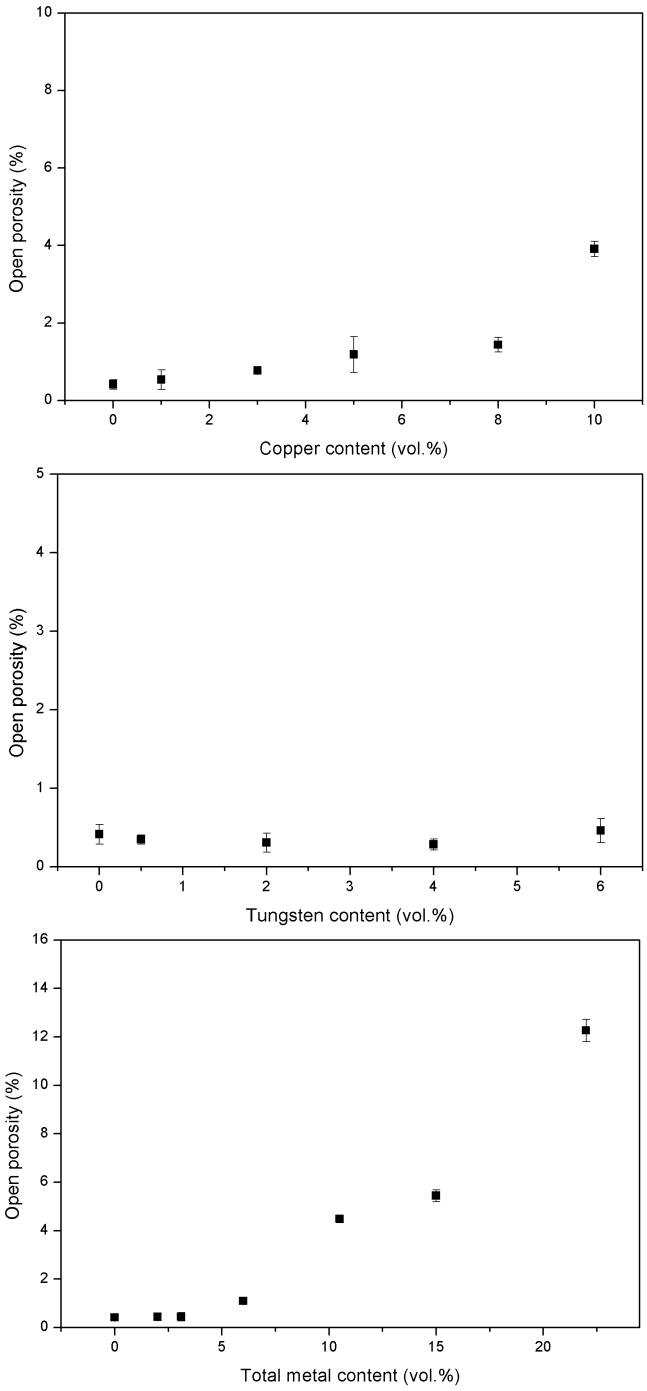
Open porosity (%)
Copper content (vol.%)
Open porosity (%)
Tungsten content (vol.%)
Open porosity (%)
Total metal content (vol.%)

Σχήμα 7

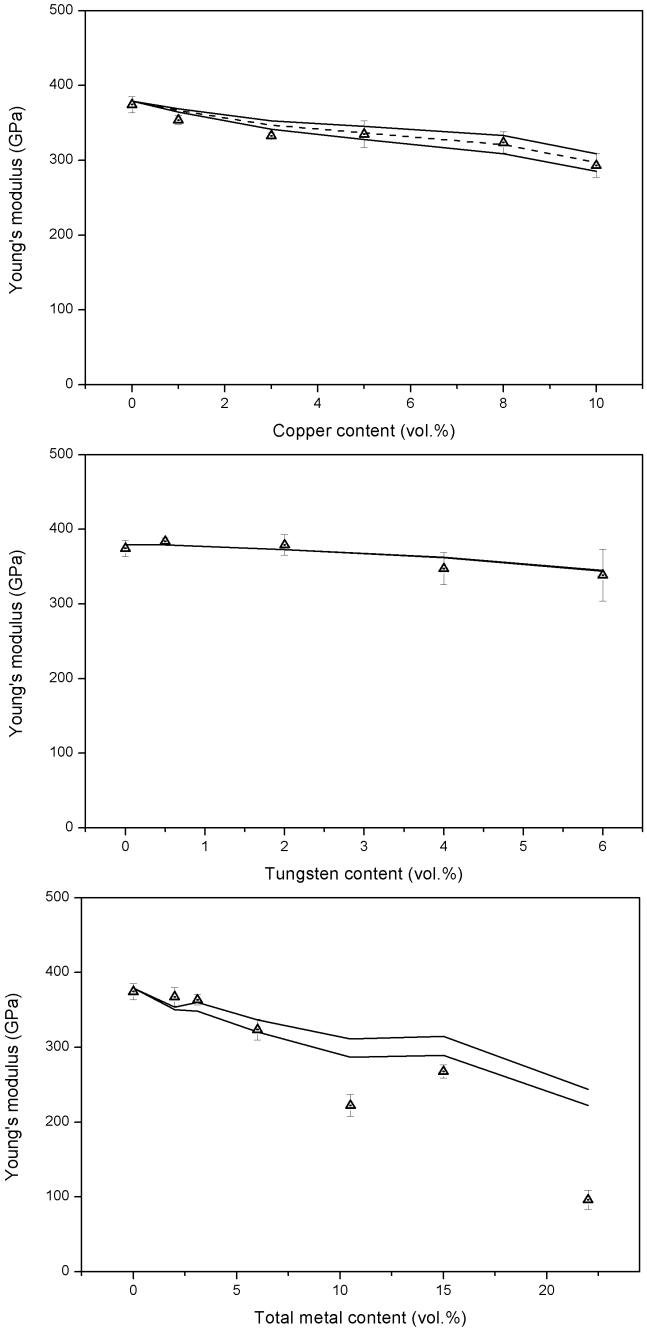
Young's modulus (GPa)
Copper content (vol.%)
Young's modulus (GPa)
Tungsten content (vol.%)
Young's modulus (GPa)
Total metal content (vol.%)

Σχήμα 8

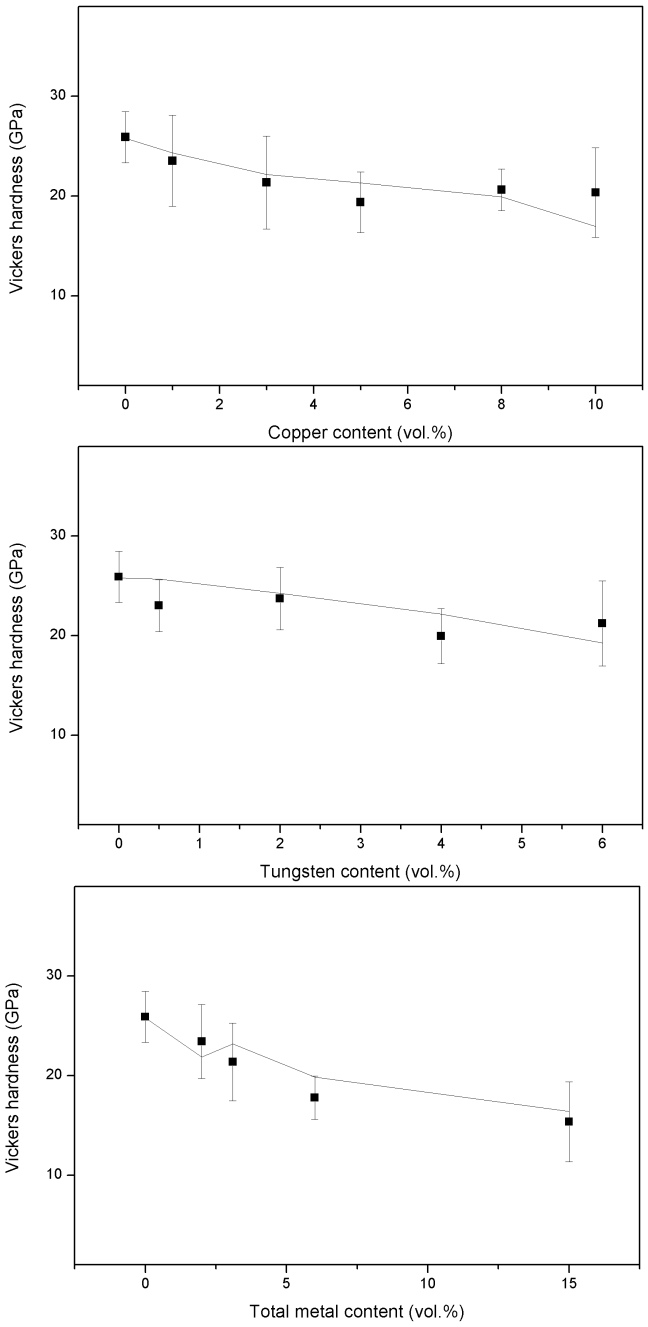
Vickers hardness (GPa)
30
20
10
0
2
4
6
8
10
Copper content (vol.%)
Vickers hardness (GPa)
30
20
10
0
1
2
3
4
5
6
Tungsten content (vol.%)
Vickers hardness (GPa)
30
20
10
0
5
10
15
Total metal content (vol.%)

Σχήμα 9

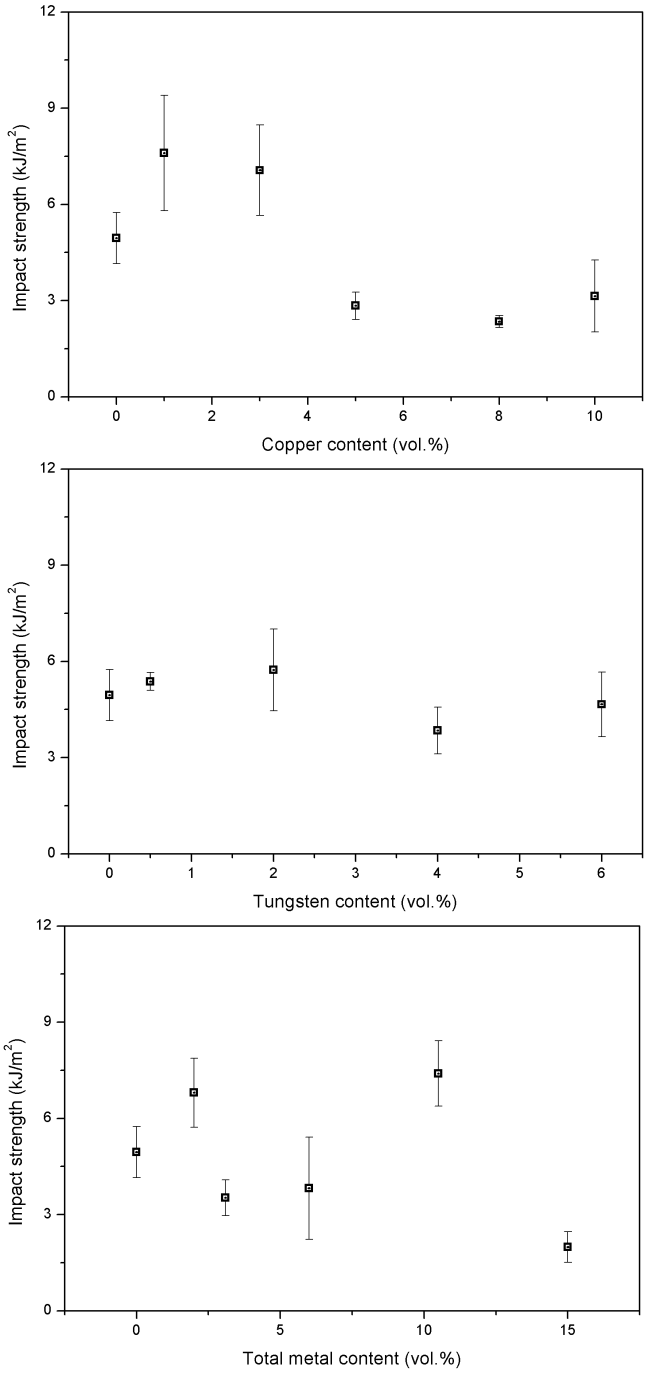
Impact strength (kJ/m^2)
Copper content (vol.%)
Impact strength (kJ/m^2)
Tungsten content (vol.%)
Impact strength (kJ/m^2)
Total metal content (vol.%)

1 Introduction

Ceramics are materials that are characterized by excellent properties including low density, high melting point, high stiffness and hardness, resistance to corrosion and oxidation, and ability to withstand high temperatures and harsh environments. Ceramics, however, exhibit limited applicability as structural engineering materials which stems from their inherent characteristic of brittleness. The synthesis of composite materials consisting of a ceramic matrix reinforced with metallic second-phase inclusions is an endeavor to produce metal/ceramic composites that possess a combination of properties not possible in monolithic metallic or ceramic materials, mostly towards an increased resistance of the matrix to crack propagation.

The aim of this research was to fabricate ceramic samples and metal-ceramic composite samples via a suitable processing route, characterize and study their macrostructure as well as microstructure, evaluate their mechanical response, and correlate the structure to the mechanical properties. Alumina, a high quality ceramic material with a unique combination of physical and mechanical properties, was selected to serve the purpose of the matrix material. The ductile nature of copper, its high fracture toughness, and relatively low density, as well as the high melting point of tungsten, high elastic modulus, and low thermal expansion coefficient were considered a good motivation for their exploitation as reinforcing materials in this study. The aqueous slip-casting processing route that was followed was considered to differentiate from other fabrication methods; i.e. the dry mixing of the powders usually yields non-uniform microstructures, while other liquid or semi-liquid shaping methods have higher requirements in organic additives which would complicate the, already, challenging sintering process. Further, its superiority was identified with reference to its cost-effective and non-hazardous aspects as a fabrication method, in addition to the potentially of fabricating parts without any restrictions concerning their shape and size.

This PhD dissertation presents an investigation on four compositions including samples of: (i) pure Al_2O_3, (ii) Al_2O_3 with five concentrations of copper

(Cu) content ranging from 1 to 10 vol.%, (iii) Al_2O_3 with four concentrations of tungsten (W) content ranging from 0.5 to 6 vol.%, and (iv) Al_2O_3 with six concentrations of mixed tungsten-copper (W-Cu) content ranging from 2 vol.% up to 22 vol.% in total. Cu-Al_2O_3 and W-Al_2O_3 composites are metal/ceramic systems that have not been widely studied, while W-Cu-Al_2O_3 is a composite not owing any scientific references as yet, to the best of the author's knowledge.

Thesis outline

This introductory chapter has presented the research area of the PhD dissertation, and has provided the aims and the structure of the thesis.

Chapter 2 discusses the basic principles and reviews the relevant literature regarding metal/Al_2O_3 composites. Some vital information of the structure and properties of the constituent phases are presented, and the micromechanics of composite materials are discussed. The fabrication and processing methods that are used to prepare ceramic and ceramic-based materials are reviewed. The theoretical considerations for ductile-particle reinforced ceramic-matrix composites are presented by introducing some crack propagation and particle/matrix interface aspects. Further, actual metal/alumina composites are reviewed in terms of processing route, resulting structure and mechanical properties.

Chapter 3 demonstrates a step-by-step experimental approach by introducing the raw materials and their characteristics, while also providing insight on the processing route followed in this work. The steps of the fabrication and sintering of the parts are discussed thoroughly. The characterization methods that were used for the raw materials (powders) and fabricated (green and sintered) samples, and the measurement techniques that were used to evaluate the mechanical behavior of the samples are given in detail.

Chapter 4 presents the characteristics of the initial powder materials that have been obtained accordingly, including the phase composition and crystal structure via X-Ray diffraction analysis, the particle size and size distribution determined via laser diffraction analysis, as well as the particle shape and morphology evaluated with the use of optical microscopy.

Chapter 5 is concerned with the macro- and micro-structural characteristics of the green and sintered samples. These include the phase composition, green and sintered density, open porosity, and linear shrinkage. Further, an analysis of the microstructure is performed in terms of particle distribution, particle size and shape via optical microscopy and analysis of the captured micrographs.

Chapter 6 provides the results of the mechanical testing that has been performed on the sintered specimens. The mechanical properties of the composites, i.e. modulus of elasticity, Vickers microhardness, and impact strength, are discussed, and the values are compared with those of the unreinforced Al_2O_3 specimens. The measured data are also compared with cited values of the literature to facilitate a further discussion in terms of structure/property correlation.

Chapter 7 concludes the research work of the PhD dissertation. The achievements of the present work are summarized, while possible topics and proposals for further work with respect to metal/alumina composites are suggested.

But before we delve into this elaborate subject, let us consider some of the relevant historical background. The work ceramic comes from the Greek adjective κεραμικός, derived from κέραμος, meaning the art of pottery. People's association with ceramics goes back in time; primitive ceramics were made of clay by first mixing with water and then firing to form objects that were fabricated to serve immediate needs, or as a form of artistic expression. Sintering, this complicated process accompanied by a number of physical and chemical changes that occur simultaneously, is also a craft that has been practiced since ancient civilizations with the firing of pottery. Setting aside the current classification of ceramic materials, i.e. traditional ceramics (bricks, tiles, pottery made of clay) or advanced ceramics (with superior properties including mechanical, thermal, optical, electrical), the interaction between the two sectors is certainly beneficial.

2 Basic Principles & Literature Review

This chapter provides basic information on ceramic and metallic materials, and presents their properties and characteristics. The attention is drawn towards the Al_2O_3 ceramic matrix, and the copper and tungsten metallic reinforcements. The processing routes that can be followed for the fabrication of ceramic and ceramic-based materials are introduced. Some theoretical considerations concerning ductile-particle/ceramic-matrix composites are discussed. Selected studies on metal-alumina composite materials are introduced; their processing route, resulting structure, and mechanical behavior (hardness, toughness, modulus of elasticity) are reviewed.

2.1 Background

Materials can be classified into three distinct categories including metals, ceramics, and polymers (although six may be more accurate; i.e. metals, ceramics, polymers, elastomers, glasses, composites (Ashby, 1989)) based on fundamental properties such as: physical (melting point and density), and mechanical (ductility, toughness, strength, and hardness). These properties can be further divided into: (a) structure-sensitive properties describing those that depend on the microstructure of a material, such as hardness, ductility, fracture toughness, thermal conductivity, and (b) structure-insensitive properties for those that do not depend on the microstructure, such as Poisson's ratio, density, melting point, elastic (Young's) modulus, thermal expansion coefficient.

Young's modulus is named after the British scientist Thomas Young, and the term modulus is the diminutive of the Latin term modus which means measure. The concept of the modulus, however, was developed by Leonhard Euler in 1727, and the first experiments that used the concept of Young's modulus in its current form were performed by the Italian scientist Giordano Riccati in 1782.

Ceramics

Ceramic materials are inorganic compounds between metallic and non-metallic elements (oxygen, carbon, or nitrogen) with strong covalent and ionic bonds. Ceramics are very hard materials, with high elastic moduli, high melting points, and low densities. Albeit their resistance to harsh environments and high temperatures, they are also characterized by their extreme brittleness. Surface flaws such as scratches, or internal flaws such as pores, microcracks, or second-phase inclusions can yield detrimental results in terms of mechanical response, mainly fracture toughness and strength.

Ceramic materials can be classified into two broad categories: the traditional ceramics (going back to early civilizations with pottery and clay objects derived from naturally occurring materials) and the advanced, engineering ceramics that are developed via synthetic routes for structural applications. These can be oxide (Al_2O_3, ZrO_2, SiO_2) or non-oxide ceramics (SiC, TiC).

Alumina | Al_2O_3

Aluminum oxide is a promising structural ceramic, frequently employed in engineering applications such as engine parts, and wear components, whilst its bio-compatibility is exploited in artificial joint prostheses. It is the most widely used engineering material for the fabrication of ceramics and is characterized by favorable properties such as low density, high hardness, high elastic modulus, and good corrosion resistance (Munro, 1997). Some selected mechanical and thermal properties of alumina are listed in Table 2.1.

The chemical bond of alumina is the covalent bonding of the Al-O groups, and its crystal structure is trigonal with six parallel planes of oxygen ions (Fig. 2.1).

Table 2.1: Selected mechanical and thermal properties of aluminum oxide.

	Alumina, Al_2O_3
Density, ρ [g cm^{-3}]	3.987
Young's modulus, E [GPa]	390
Poisson ratio, ν	0.25
Elongation ratio [%]	
Fracture toughness, K_{Ic} [MPa m$^{1/2}$]	3-5.3
Melting point, mp [°C]	2054
Thermal conductivity, k [W m^{-1} K^{-1}]	36
Linear thermal expansion, α_L [10^{-6} K^{-1}]	8

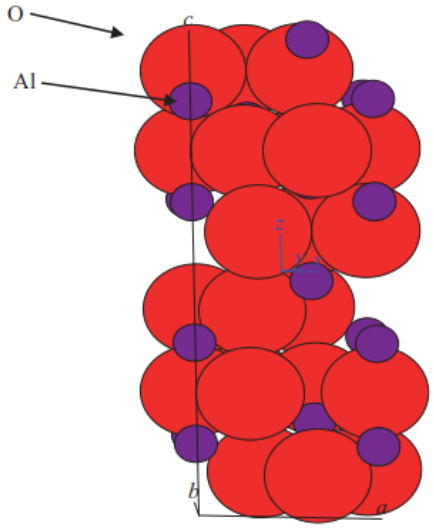

Figure 2.1: Crystal structure of Al_2O_3.

Alumina exists in many polymorphs, most of which are metastable, and can be classified into two categories: the FCC (such as the γ-alumina) or the HCP packing arrangement of oxygen anions. The α-alumina (the mineral corundum) is thermodynamically stable, and the one with the highest density (Levin and Brandon, 1998).

Alumina can be prepared in a variety of grades which differ in the size and shape of crystals, and level of chemical purity. The impurities (MgO, SiO_2, ZrO_2) are usually added to reduce the sintering temperature, or to control the grain size. The percent purity of the alumina ceramic strongly affects its properties, such as density, Young's modulus, and fracture toughness. Some common commercially available grades of alumina are the calcined, reactive, and tabular alumina (Cardarelli, 2008):

calcined alumina the calcined alumina, or α-alumina, is a polycrystalline material that consists of α-Al_2O_3 crystallite clusters with a particle size ranging from 0.5 to 10 μm. It is the most dense and stable crystalline form of alumina, and is used in a wide range of ceramic and refractory applications. The major impurity of calcined alumina is soda, and, therefore, calcined aluminas are categorized based on their Na_2O content,

tabular alumina the tabular alumina, or sintered alumina, is produced by sintering the calcined alumina above 1600 °C. It is of high purity (99.8 wt.% Al_2O_3) due to its low soda content, and consists of large crystals of corundum,

reactive alumina the reactive alumina is used when exceptional strength, wear and temperature resistance are required. It has a relatively high purity and small crystal size (<1μm), and sinters to a fully dense compact at a lower sintering temperature than the calcined alumina.

Porosity of ceramics

Porosity is a significant matter for ceramic materials, and efforts are devoted during manufacturing to minimize, or ideally eliminate, the void formation through optimization of the processing route. The porosity, P, for a given material can be determined by the ratio:

$$P = \frac{V_v}{V_t}\,, \tag{2.1}$$

where V_v is the volume of the void space, and V_t is the total volume of the material. Porosity is a fraction between 0 and 1, and can be classified into

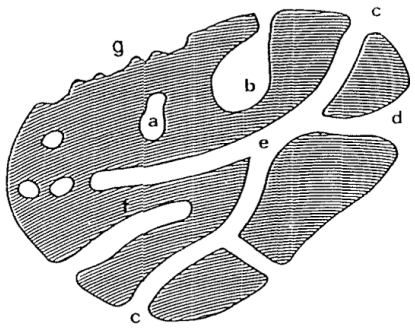

Figure 2.2: A schematic cross-section of a porous solid.

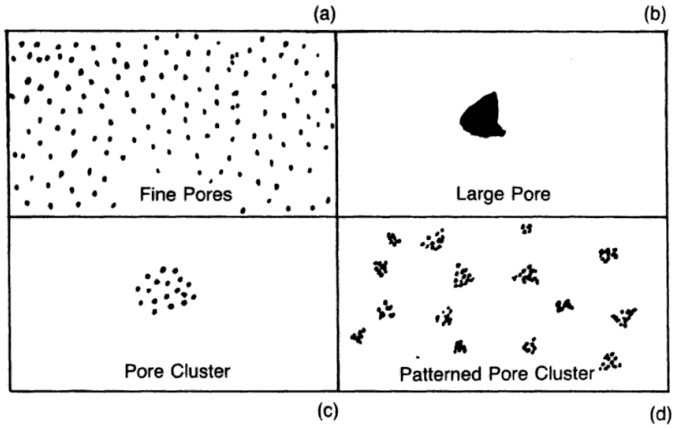

Figure 2.3: Common pore structures in sintered ceramics.

different types. Typical classes of porosity for ceramic and ceramic-based materials include the effective or open porosity, and the ineffective or closed porosity.

A schematic of a porous solid is shown in Fig. 2.2. The pores are classified according to their accessibility to an external fluid. For instance, one category is that of region (*a*) that reflects a closed pore which is isolated from other voids. Open pores, on the other hand, (see regions *b*, *c*, *d*, *e*, *f*) correspond to pores that thread through the solid, and communicate with the surface.

Common pore structures in sintered ceramics might include fine pores that are distributed throughout the body, large pores that may be due to the organic binder, or pore clusters, Fig. 2.3. Two rather useful terms for the description of porous solids include the "true" density (the density of the material excluding the pores and voids), and the "bulk" density (the density of the material including the pores and voids).

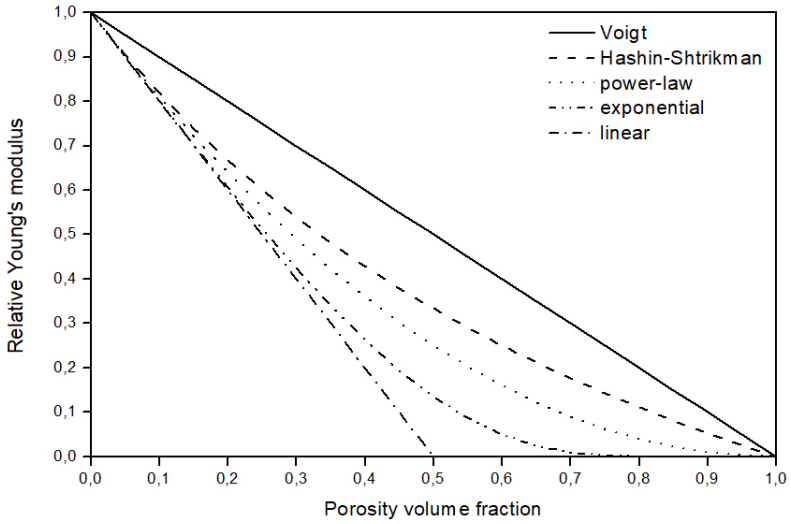

Figure 2.4: Effect of porosity on the elastic modulus of ceramics (Eqs. 2.3 - 2.8).

Effect of porosity on elastic modulus

The residual porosity, after sintering, is a characteristic of the structure that has an influence on the mechanical behavior of ceramic materials. The work of Coble and Kingery, 1956 provides a useful insight on the effect of porosity on the elastic modulus, strength, and thermal expansion coefficient of sintered alumina ceramics with isolated pores and total porosity ranging from 5 to 50%. It was concluded that the presence of pores does not influence the coefficient of thermal expansion, yet decreases the strength, and the elastic moduli of the bodies.

Polycrystalline ceramics with residual porosity are characterized by a decreased value of elastic modulus, given that a pore has zero stiffness. Some expressions that relate the porosity volume fraction, ϕ, of the material to its relative elastic modulus, E_r, are listed in this section. The relative modulus, E_r, is used to express the ratio of the modulus of the porous material, E, to the modulus of the solid material, E_o, (Fig. 2.4):

$$E_r = \frac{E}{E_o} \,. \tag{2.2}$$

The Voigt upper bound (Paul, 1960) and the Hashin-Shtrikman upper bound (Hashin and Shtrikman, 1963) are given by the following equations, respectively:

$$E_r = 1 - \phi \,, \tag{2.3}$$

$$E_r = \frac{1-\phi}{1+\phi} \,, \tag{2.4}$$

while the linear approximation is valid for low porosities and spherical voids (Dewey, 1947; Mackenzie, 1950):

$$E_r = 1 - 2\phi \,. \tag{2.5}$$

For higher porosities non-linear equations have to be used, such as the non-linear Coble-Kingery relation (Coble and Kingery, 1956; Pabst and Gregorová, 2003), which is identical to the Gibson-Ashby power-law relation (Gibson and Ashby, 1982):

$$E_r = 1 - 2\phi + \phi^2 \,, \tag{2.6}$$

$$E_r = (1-\phi)^2 \,, \tag{2.7}$$

and the Pabst-Gregorová exponential relation (Pabst and Gregorová, 2004):

$$E_r = \exp\left(\frac{-2\phi}{1-\phi}\right) . \tag{2.8}$$

Effect of porosity on hardness

The hardness of ceramics is also affected by the presence of void spaces throughout the matrix material. To account for the residual porosity of the matrix, an empirical exponential equation can be applied to predict the hardness of porous ceramic materials in the form of (Rice, 1989):

$$H = H_o \exp(-bP) \,, \tag{2.9}$$

where H_o is the hardness of the fully dense material, P is the volume fraction of porosity, and b is a constant that varies between 1 and 9 (Rice, 1996).

Table 2.2: Selected mechanical and thermal properties of tungsten and copper.

	Tungsten, W	**Copper, Cu**
Density, ρ [g cm^{-3}]	19.293	8.941
Young's modulus, E [GPa]	411	130
Poisson ratio, ν	0.28	0.34
Elongation ratio [%]	2	55
Fracture toughness, K_{Ic} [MPa m$^{1/2}$]	16	50
Melting point, mp [°C]	3414	1084
Thermal conductivity, k [W m^{-1} K^{-1}]	174	401
Linear thermal expansion, α_L [10^{-6} K^{-1}]	4.6	17

Metals

Metals are ductile and malleable materials, good conductors of heat and electricity, and are more dense than ceramic materials. Most metals usually fail in a ductile manner at room temperature due to plastic deformation that is related to their metallic bonding, as opposed to ceramics which fail under a brittle fracture due to their ionic bonding. Ductility is, thus, an important mechanical property of metals, and is a measure of the degree at which a structure will be plastically deformed prior fracture. Ductility can be expressed quantitatively as a percent elongation (%EL) given by:

$$\%\mathrm{EL} = \frac{l_f - l_o}{l_o} \times 100\,, \tag{2.10}$$

where l_f is the fracture length, and l_o the original length. Common metals that have a high percent elongation (approx. 40-50%) include copper, iron, aluminum, and nickel (Callister and Rethwisch, 2009; Cardarelli, 2008). Metals are used depending on the exploitation of properties such as high melting point and low coefficient of thermal expansion (tungsten) and ductility (copper). Some selected mechanical and thermal properties of the metallic materials used in the present study can be found in Table 2.2.

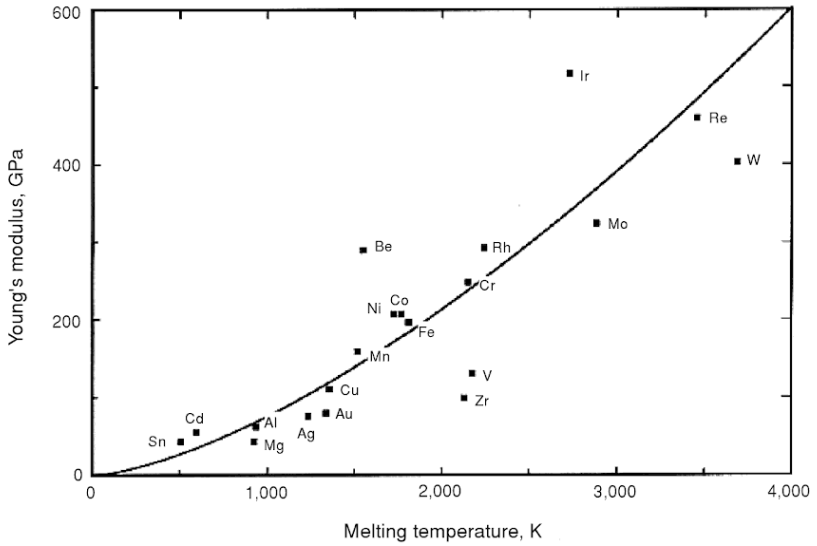

Figure 2.5: Correlation between Young's modulus at room temperature and melting point for various elements.

W | Tungsten

Tungsten was discovered in 1781 by the Swedish chemist Carl Wilhelm Scheele.

Tungsten is a hard and usually brittle grayish metal. It has the highest melting point of all metals in pure form, and the lowest thermal expansion coefficient (Fig. 2.5). Tungsten is characterized by excellent high temperature mechanical properties, excellent corrosion resistance, and is among the heaviest metals. Three modifications of tungsten are known: α, β, and γ. The α-form is the only stable modification, with a BCC metal crystal structure. The β-W and γ-W are metastable phases which convert to α-tungsten when heated above 600 °C - 700 °C (Lassner and Schubert, 1999).

The chemical interaction of tungsten with various elements, compounds, and/or gases is rather important in terms of fabricating and sintering W-Al_2O_3 composite materials. Tungsten is stable at room temperature; it is prone, however, to oxidation in air (N_2 + O_2), which initiates from around 300 °C to 500 °C and leads to the formation of tungsten oxides at higher temperatures. The intensive oxidation of W at air begins from 850 °C to 900 °C and leads to a marked loss of material by the vaporization of oxides. There is no interaction of tungsten with water at the ambient temperature. At higher temperatures,

however, the oxidation of W in the presence of water vapour is severe and is accompanied with an intensive vaporization of tungsten oxides (Shabalin, 2014).

Cu | Copper

Copper was discovered around 9,000 BC in the Middle East.

Copper is a soft, reddish metal, with an FCC crystal structure. It is an extremely ductile metal, and a good conductor of heat and electricity. The metallic bonds of copper are relatively weak, which reflect its low hardness and high ductility.

Copper is not particularly reactive, in comparison to most metals. It is resistant to attack by oxygen, and is not corroded by water, or even steam. It is easily attacked, however, by air and forms a protective patina (a thin surface layer to protect the metal from further attack) (Beatty, 2001). The oxidation of copper is a well-known process, and the two copper oxides that are usually formed are the red cuprous oxide, Cu_2O, and the black cupric oxide, CuO, the reduction of which may be accomplished by sintering under a reducing hydrogen atmosphere (Davis, 2001).

2.2 Composite materials

The term composite is used to describe a material that consists of two or more constituent materials with different physical and chemical characteristics. Composite structures are fabricated for being lighter, or more resistant, or less stiff, and more tough, and are designed to produce new materials that meet specific engineering requirements, by exploiting the advantageous individual characteristics of each component. Typical examples of composite materials are metal-matrix composites reinforced with ceramic particles to enhance the thermal properties and improve the corrosion resistance, or ceramic-matrix composites reinforced with metal particles to augment their mechanical behavior (Evans and McMeeking, 1986; Evans, 1990; Becher, 1991).

Ceramic-matrix-composites, in particular, have been rather popular due to their numerous applications and their applicability in mechanical and high-temperature demanding sectors, such as structural parts of engines, and

brake discs. The structure of CMC's may include (see Fig. 2.6): short or long fibers (a, b), layered composites (c), isometric particle reinforcement (d), functionally graded materials (e), polycrystalline composites (f, g, h).

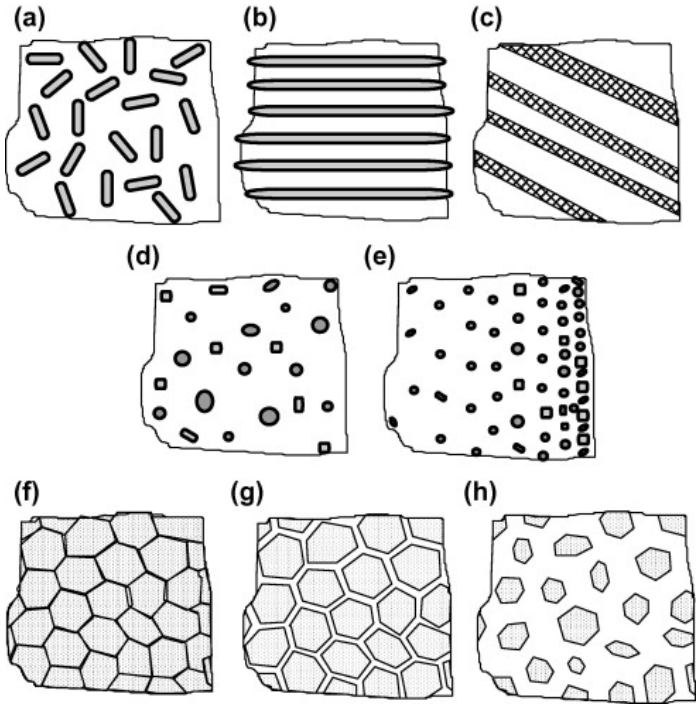

Figure 2.6: Different structures of ceramic-matrix composite materials.

2.2.1 Micromechanics of composites

Predicting the overall properties of a composite structure is of major importance; the density and the elastic modulus of composite materials are two key properties.

2.2.1.1 Density

Assuming a composite material of mass m_c and volume v_c that consists of a filler (m_f, v_f) and a matrix (m_m, v_m), then the total mass of the composite will be:

$$m_c = m_f + m_m \,, \tag{2.11}$$

while the volume of the composite will be:

$$v_c = v_f + v_m + v_v \ , \tag{2.12}$$

where v_v is the volume of the voids that might be present in the composite structure. Further, the theoretical density, ρ_c, of the composite material will be:

$$\rho_c = \rho_f V_f + \rho_m (1 - V_f) \ , \tag{2.13}$$

where V_f is the volume fraction of the filler, ρ_f is the density of the filler, and ρ_m is the density of the matrix. The relative density, RD%, can be calculated by:

$$\text{RD\%} = \frac{\rho^{exp}}{\rho_c} \times 100 \ , \tag{2.14}$$

where ρ^{exp} is the experimental density. The volume fraction, V_f, and the weight fraction, W_f, of the filler can be deduced by the following equations, respectively:

$$V_f = \frac{W_f / \rho_f}{W_m / \rho_m + W_f / \rho_f} \ , \tag{2.15}$$

$$W_f = \frac{V_f \rho_f}{V_m \rho_m + V_f \rho_f} \ . \tag{2.16}$$

2.2.1.2 Young's modulus

The modulus of elasticity (Young's modulus or elastic modulus) is a key property that determines a solid material's stiffness; i.e. its resistance to being elastically deformed under an applied stress. The elastic modulus can be calculated by dividing the tensile stress, σ, to the tensile strain, ϵ:

$$E = \frac{\sigma}{\epsilon} \ . \tag{2.17}$$

For two-phase composite materials, the elastic modulus, E_c, can be determined by applying a series of equations which include the properties of their components: E_m and E_f for the modulus of the matrix and the filler, respectively, and V_m, V_f as noted earlier.

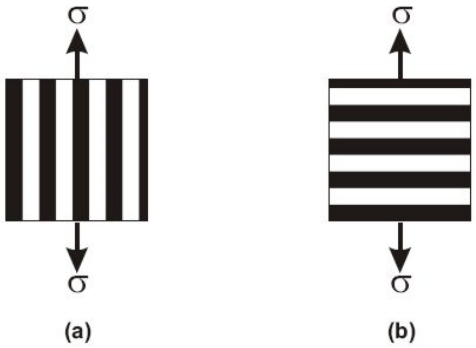

Figure 2.7: (a) Voigt and (b) Reuss formulation for two-phase composite materials.

Theories for the effect of particle loading on the elastic modulus

Various empirical or semi-empirical equations have been proposed to predict the elastic modulus of two-phase composites. The Voigt and Reuss bounds (Fig. 2.7) represent the simplest case (Hill, 1952; Hill., 1963).

The Voigt (upper) bound notes that the two phases will suffer the same strain upon loading, and the stress is the volume-average (parallel arrangement):

$$E^{+} = E_c = E_m V_m + E_f V_f \,, \tag{2.18}$$

and the Reuss (lower) bound notes that the two phases will carry the same stress and the strain is the volume average (series arrangement):

$$E^{-} = E_c = \left(\frac{V_m}{E_m} + \frac{V_f}{E_f} \right)^{-1} . \tag{2.19}$$

The relationship given by Eq. 2.18 is commonly referred to as rule-of-mixtures equation. Generally, the modulus of the composite material must lie in the regime formed by these two bounds; i.e. it should be lower than the upper bound and higher than the lower bound.

The simple arithmetic mean of the Voigt and Reuss bounds has been proposed by Hirsch as a "modified mixture rule" estimate of the elastic modulus in the form of (Hirsch, 1962):

$$E_c = \frac{E^{+} + E^{-}}{2} . \tag{2.20}$$

Depending on the elastic moduli values of the individual phases, and the composition of the material, the Voigt and Reuss bounds might be widely spaced, hence a number of formulations is available in the literature including more precise upper and lower bounds that form a regime more narrow than the Voigt-Reuss bounds, such as those proposed by Hashin and Shtrikman, 1963 and Ravichandran, 1994.

Other predictions have also been proposed, such as the Counto model that assumes a perfect bonding between the particles and the matrix in the form of (Counto, 1964):

$$\frac{E_c}{E_m} = 1 + \frac{V_f}{\frac{1}{\delta - 1} + {V_f}^{\frac{1}{2}} - V_f} \,. \tag{2.21}$$

Another upper bound solution is that proposed by Paul for a cubic inclusion that is embedded in a matrix (Paul, 1960):

$$\frac{E_c}{E_m} = \frac{1 + (\delta - 1){V_f}^{\frac{2}{3}}}{1 + (\delta - 1)({V_f}^{\frac{2}{3}} - V_f)} \,, \tag{2.22}$$

and another lower bound solution is given by Ishai-Cohen in the form of (Ishai and Cohen, 1967):

$$\frac{E_c}{E_m} = 1 + \frac{V_f}{\frac{\delta}{\delta - 1} - {V_f}^{\frac{1}{3}}} \,. \tag{2.23}$$

Additional predictive equations include the semi-empirical relationship of Halpin-Tsai for the modulus of particulate polymers (Halpin, 1969):

$$\frac{E_c}{E_m} = \frac{1 + ABV_f}{1 - BV_f} \,, \tag{2.24}$$

where A and B are constants for a given composite, and the Takayanagi model that was developed for polymer composites assuming spherical particles (Takayanagi, Uemura, and Minami, 1964):

$$\frac{E_c}{E_m} = \left(1 - \phi + \frac{\phi}{1 - \lambda + \lambda\delta}\right)^{-1} \,, \tag{2.25}$$

where ϕ and λ are functions of the volume fraction, with $\phi\lambda = V_f$.

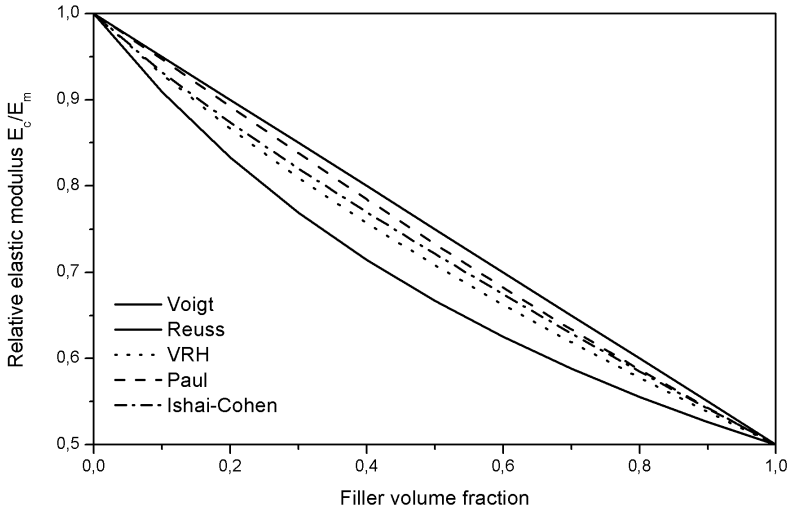

Figure 2.8: Dependence of relative elastic modulus (E_c/E_m) on the volume fraction of the reinforcement phase.

Fig. 2.8 illustrates some of the aforementioned equations for the prediction of the elastic modulus of composite materials as a function of the second-phase content. It can be seen in this graph that despite the possible applicability of each formulation, all equations fall in the regime formed by simple rule of mixtures (Eqs. 2.18 and 2.19), and, therefore, satisfy the following boundary conditions: (i) $E_c = E_m$ for $V_f = 0$, and (ii) $E_c = E_f$ for $V_f = 1$.

Effect of particle loading on hardness

In this respect, the theoretical prediction of the rule of mixtures for the hardness, H, of a two-phase composite material is in the form of:

$$H = V_f H_f + (1 - V_f) H_{Al_2O_3} \, , \tag{2.26}$$

where H_f and $H_{Al_2O_3}$ are the theoretical hardness values of the metallic phase and the alumina matrix, respectively.

2.3 Fabrication of ceramic materials

The research interest towards ceramic-matrix composite materials, that originates from their novel and enhanced properties, has resulted in the need for suitable processing routes and fabrication methods. In this section different

shaping techniques and densification processes will be presented, followed by the critical steps of debinding and sintering, while the effect of different parameters is also discussed.

2.3.1 Raw materials

The selection of the raw materials is one of the major issues that needs to be addressed for the successful preparation of ceramic and ceramic-based materials. Some important characteristics of the starting materials relate to the powder properties and these include the particle size, particle size distribution, and particle structure or shape.

The particle size can be reduced to meet the requirements of specific applications through various milling methods, such as ball milling (Carter and Norton, 2007). The particle shape is an important characteristic that has an effect on the powder density and, therefore, the sintering process. The shape depends on the production method of the powder and can be characterized accordingly as illustrated in Fig. 2.9a-2.9i. For instance, the acicular has needle-shaped characteristics, the dendritic has a branched crystalline shape, the irregular is due to lacking of any symmetry, and the spheroidal has roughly spherical dimensions. The images, however, portray ideal shapes and morphologies, while in reality particle shapes are more complex and might deviate and/or can exhibit characteristics of more than one type. The chemical composition of the powder is another important aspect of the initial materials. For instance metallic powders can be composed of only pure elements or a mixture of elements. Additional characteristics that relate to the chemistry of the powder are surface area and bulk density.

A major issue concerning powders is that of the degree of agglomeration which dominates the densification process and the resulting sintered density of the fabricated samples. The presence of hard agglomerates can be detrimental as they might delay the progress of void-elimination in the matrix. Fig. 2.10 is a schematic representation of an agglomerated powder, in which the large inter-agglomerate pores and the smaller intra-agglomerate pores can be discerned.

2.3.2 Shaping and forming techniques

The shaping process followed to manufacture a compact ceramic material refers to the transformation of a powder mixture into a consolidated body of a desired shape. There are several shaping techniques that can be employed

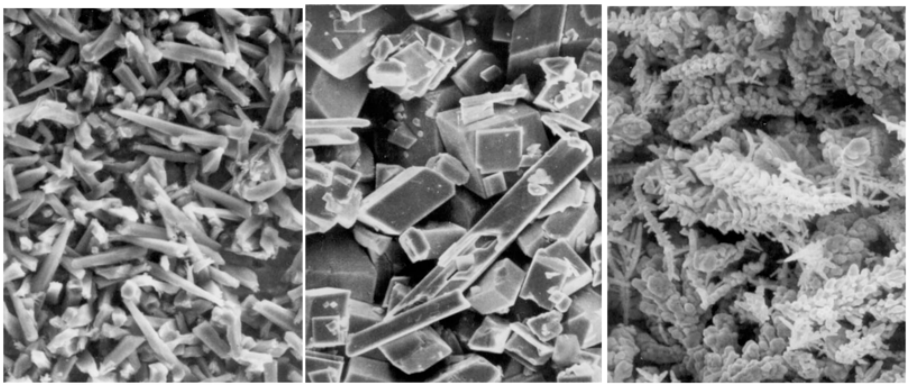

(a) Acicular **(b)** Angular **(c)** Dendritic

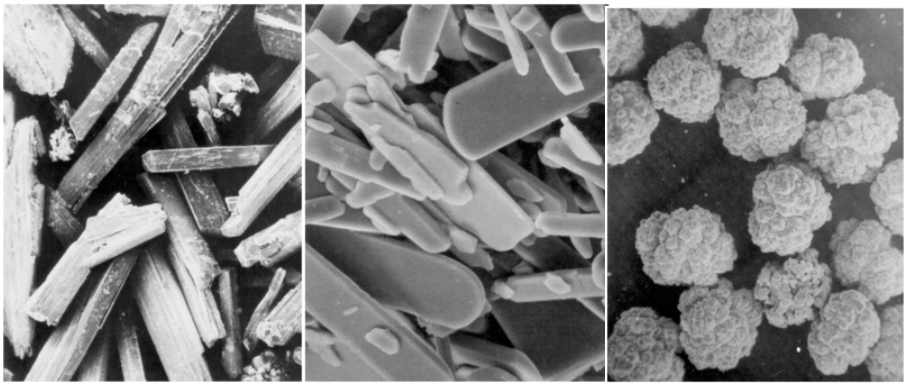

(d) Fibrous **(e)** Flaky **(f)** Granular

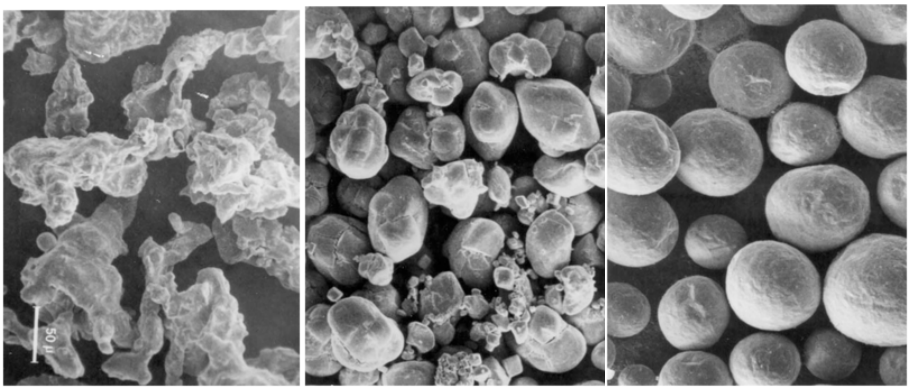

(g) Irregular **(h)** Nodular **(i)** Spheroidal

Figure 2.9: Common particle shapes as depicted in ISO 3252.

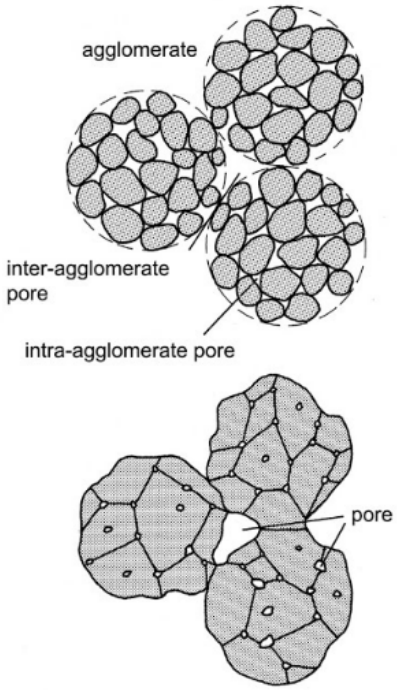

Figure 2.10: Schematic of an agglomerated powder with intra-agglomerate pores inside the agglomerates, and inter-agglomerate pores between the agglomerates.

for the synthesis of ceramic and ceramic-based materials, and these can be categorized depending on the water requirement of each processing method:

dry shaping refers to the production of ceramic samples through a simple compaction of powders. In that case the addition of water is more or less redundant. The dry (cold) pressing technique is the most widely used method of this category, and is employed for the production of solid samples with simple shapes. The process is quite simple and involves three steps, as shown in Fig. 2.11: the filling of the die with the powder, the compaction of the powder, and the removal of the formed sample. A low amount of binder is usually mixed with the raw powders, prior the filling of the die. However, density variations across the thickness of the sample, which can cause cracking and distortion during sintering, are a major disadvantage of the method. An alternative route is that of cold isostatic pressing (CIP) which allows the synthesis of more complex-shaped bodies, and usually results in higher green densities and a more uniform structure of the sample. Hot-pressing is another dry shaping method, which yields near theoretical densities through the simultaneous application of pressure and heat. It is a high-cost processing route, with limited productivity, and is suitable mostly for the manufacture of parts with simple shapes.

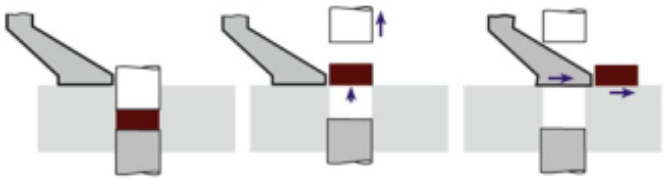

Figure 2.11: Dry pressing technique.

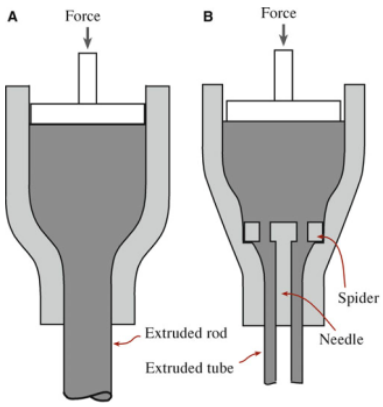

Figure 2.12: Extrusion of (a) rods and (b) tubes.

plastic shaping involves the methods which require the addition of a liquid (usually water, or an organic liquid) to produce a plastic mass under pressure. The most widely used method is that of extrusion during which a pliable mass is formed and goes through a die orifice. This method is usually employed for the production of long-shaped samples, such as rods and tubes (see Fig. 2.12). This pliable mass, however, is only properly formed via the addition of complex organic compounds that are used to facilitate the process. Another plastic-shaping method which also demands rheological adjustments is that of injection molding.

semi-liquid shaping describes the shaping methods that require a high amount of water, and are performed at room temperature conditions. A characteristic example of this category is that of slip casting where a suspension/slurry is initially formed, and is then poured into a porous gypsum mold that contains capillaries and absorbs water from the slurry, as shown in Fig. 2.13. Tape casting is another semi-liquid method, used for the formation of ceramic films or sheets, during which the slip is poured to a moving flat surface, and a doctor blade is used to spread the slip and form a thin tape, as shown in Fig. 2.14.

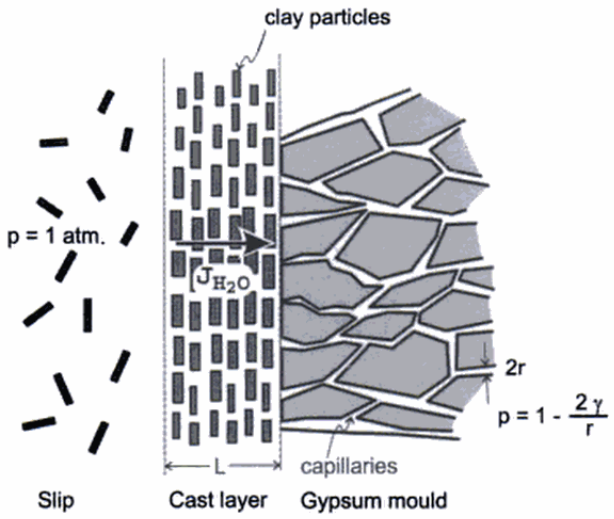

Figure 2.13: Slip-casting process showing the water that is absorbed by the capillary pressure in the mold.

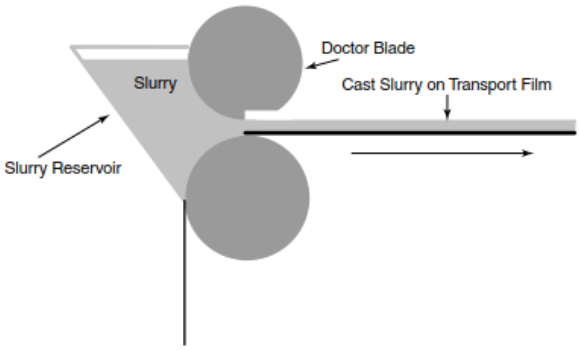

Figure 2.14: Tape casting of slurry using a doctor blade.

Basics of the slip-casting technique

Plaster of Paris is named after the French city where it was made and where there are abundant gypsum deposits. Following the Great Fire of London, in 1666, the walls of all wooden houses in the city of Paris were covered with plaster to provide fire protection. The earliest use of plaster coating dates back 9,000 years and was found in Anatolia and Syria. The Egyptians used plaster made from dehydrated gypsum powder mixed with water as a joining compound in the magnificent pyramids (Carter and Norton, 2007).

The manufacture of parts with the use of the slip-casting process is realized via the formation of a liquid mixture (slip), i.e. a suspension of particles in a liquid medium that is usually water. The slurry is poured into a porous and permeable mold that has been fabricated from mixing appropriate quantities of water and Plaster of Paris.

The presence of a deflocculant in the slurry is paramount as this neutralizes the electrical charge of the alumina powder, and enables the preparation of a stable suspension. The optimum results are obtained when a slurry with high solid content is prepared, given that a high amount of water results not only in lower densities, but also longer casting times, and thus, a lower number of produced samples.

Slip casting can be solid or drain: in solid casting the slurry is constantly poured into the mold (Fig. 2.15), whereas in drain casting the slurry is poured into the mold and the excess slip is drained as soon as a wall of appropriate thickness is formed, Fig. 2.16. This renders the drain casting technique suitable for the synthesis of hollow samples such as crucibles or tubes. Alternative routes for the casting technique include the centrifugal casting (spinning the mold to achieve better density), gel casting (polymerization and cross-linking of monomers in the slurry), vacuum casting, pressure casting.

The advantages of the solid slip-casting method include the low cost, the ability to fabricate samples in many (complex) shapes, and its versatility allowing one to prepare porous ceramic-matrix composites or composites with a graded structure (Pabst et al., 2011; Zygmuntowicz et al., 2016). The initial

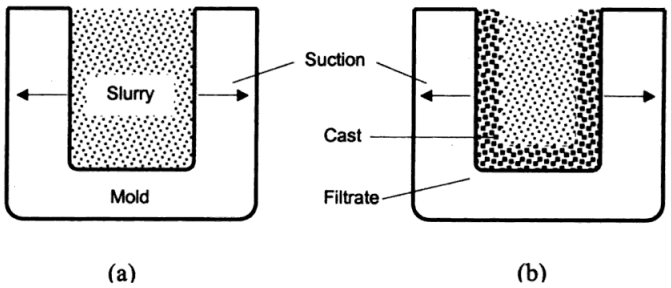

Figure 2.15: Schematic of the slip-casting system: (a) initial status, and (b) after the formation of a thin cast.

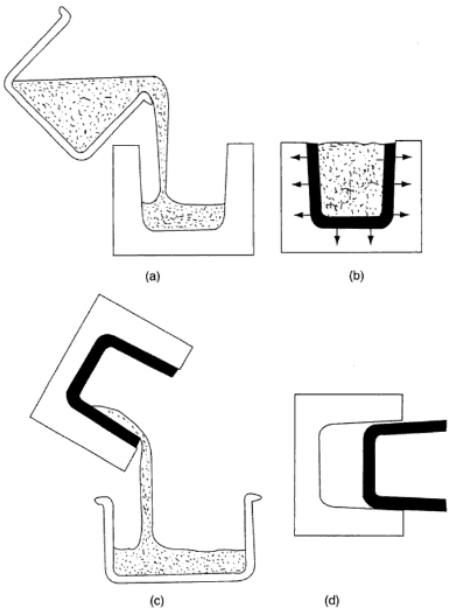

Figure 2.16: Schematic illustrating the drain-casting process; (a) the slip is poured into the mold; (b) the mold extracts the liquid and a compact is formed against the mold walls; (c) the excess slip is drained from the mold; (d) the casting is removed after some partial drying.

Table 2.3: Typical compositions of alumina slurries for different shaping techniques.

	slip casting (vol.%)	**tape casting (wt.%)**	**extrusion (vol.%)**
alumina powder	40-50	69.0	45-50
water	50-60	14.4	40-45
binder	0-0.5	6.9	5
dispersant	0.5-2	0.6	1-2
plasticizer		9.0	1
other additives		0.1	1

particle packing of the green parts is also a major advantage, in comparison to conventional dry-pressing techniques, see Fig. 2.17. Further, the slip-casting method has the lowest requirements in organic additives over other liquid or semi-liquid shaping methods. Typical compositions for Al_2O_3 slurries (alumina powder, water, and organics additives) are listed in Table 2.3. The disadvantages of the method include the long casting times, and the necessity to produce the molds and allow them to sufficiently dry between subsequent castings.

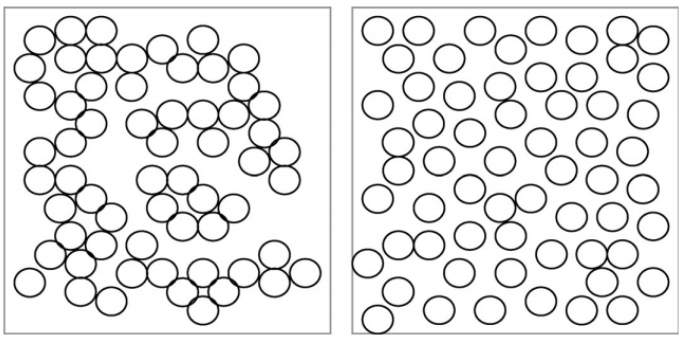

Figure 2.17: Initial particle packing for the same number of particles per unit volume for green bodies; pressing (left) and slip casting (right).

Drying

Drying describes the process of water removal from a fabricated body. The water molecules diffuse from the inner part of the sample to its surface and then evaporate. During this step various defects might appear, and therefore the rate of evaporation should be lower than the rate of diffusion in order to avoid cracking due to a fast loss of water, or crazing (network of lines or small cracks) due to CTE mismatch.

Drying is usually accomplished by thermal means and relates to the moisture that is removed from the green part due to evaporation. An important parameter is the amount of water present in each green part, which depends on the processing route. In dry pressing, for example, the required amount of water is rather low or non-existent, while for other methods, such as extrusion or slip-casting, more attention is required. Other factors that have an effect on the drying process are the shape and thickness of a sample. For instance long rod-shaped and large-diameter samples are prone to distortion and/or the formation of cracks on the surface layer.

2.3.3 Debinding

The binder removal (binder burn-out or debinding) is an important step that takes place prior the sintering of the green parts. It is a key stage that requires a thorough control in order to avoid the likely formation of defects such as bubbles, cracks, or distortion of the samples.

For the case of oxide ceramic materials, the binder burn out process is simply performed in air atmosphere under heat, and is, in general, completed without any difficulties. The binder is oxidized and forms compounds of H_2O, CO and CO_2. For non-oxide ceramics, or composite materials, however, this step is more demanding as it requires for the debinding to be performed under inert or reducing atmospheres. For composite materials that contain metal powders, in particular, debinding is a rather crucial step.

The aim of the debinding cycle is to melt, decompose and/or evaporate the organic binder, a process which may be more complicated for parts which include more than one organics, with different melting points, decomposition rates and temperatures. The burn-out of the binder can be achieved via a solvent or a thermal removal process (German, 1987; Todd and Sidambe, 2013):

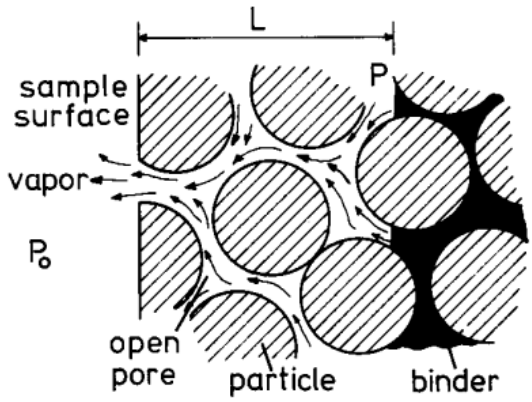

Figure 2.18: Thermal debinding model due to existence of pores.

solvent debinding is a process which can be realized via the extraction method, the high pressure solvent method, or a thermally assisted solvent method, and yields a high "brown" strength. Major disadvantages of the solvent debinding processes include the use of solvents which renders them not-environmentally friendly, and raises issues of toxicity and safety. In addition they have a relatively limited applicability; for instance the extraction method (in which the sample is immersed into a liquid that dissolves the binder material) cannot by utilized for slip-casted samples, as the solvent would dissolve the green compact.

thermal debinding is a process which has inexpensive equipment and is performed under a temperature-controlled environment, but requires long cycles and results in a poor "brown" strength. The thermal debinding can be described with three mechanisms: diffusion, permeation, or wickening, which can categorized depending on the state of the extracted binder. Diffusion and permeation are activated when the binder is a vapor, whilst wicking when the binder is a liquid. A schematic of the thermal debinding process due to diffusion or permeation is shown in Fig. 2.18. The binder decomposes due to the high temperatures, transforms into other compounds such as water and carbon dioxide, and is then removed from the sample. During the debinding step, the organics are free to travel from the inner body to the surface, and escape from the open pores in the form of vapour.

The choice of binder is very important as it should be easily removed from the green body and should not form toxic products upon decomposition. Further, the temperature and heating rates during the burn-out must by carefully adjusted: a fast heating rate might produce cracks on the surface of the samples, whilst a slow heating rate may be effective but not cost-efficient.

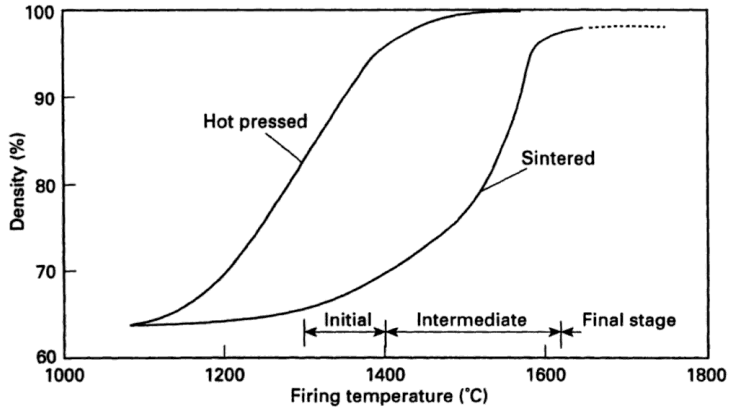

Figure 2.19: Density variation with temperature for reactive alumina powder showing the stages of sintering for hot-pressed and sintered Al_2O_3.

2.3.4 Sintering

Sintering is a processing technique during which a porous structure (green body) is fired at high temperatures and is transformed into a consolidated dense material via changes in the size and shape of pores (Basu and Balani, 2011). It is a rather complex phenomenon during which several processes take place simultaneously, thereby achieving the theoretical density is difficult, and ceramics usually contain a 5% residual porosity after sintering, see Fig. 2.19.

There are various parameters that are related to the sintering process such as the sintering pressure and atmosphere, the sintering temperature and dwell time, the heating and cooling rates, the sintering state (German, 2014):

pressure sintering can be performed with the simultaneous application of heat and pressure, such as the hot pressing technique, or without pressure, namely pressureless sintering,

atmosphere the sintering atmosphere can be hydrogen (reducing but costly), nitrogen (less expensive, neutral, with no reduction role), argon (costly, neutral, no oxidation, no reduction), air (oxidizing, no significant cost), vacuum (absence of atmosphere, no cost but maintenance), or combinations of the above such as nitrogen-hydrogen (reactivity, mixture of costs),

state sintering can be solid state or liquid phase: the solid state sintering describes the densification of a compact that is in a solid state at the sintering temperature, whereas the liquid phase sintering occurs when a liquid phase is present at the sintering temperature. Fig. 2.20 portrays

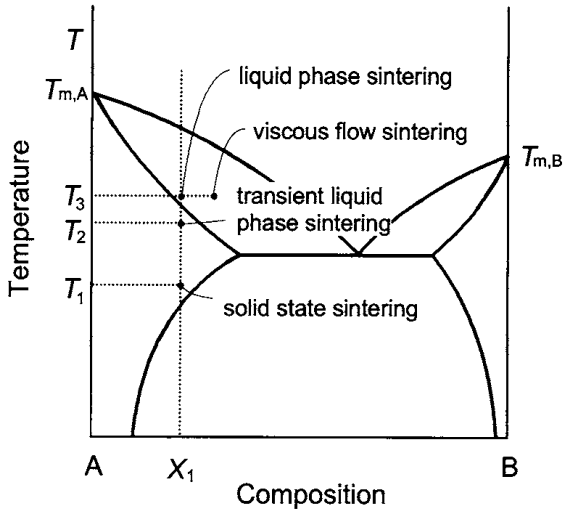

Figure 2.20: Schematic phase diagram showing the different types of sintering.

an A-B powder compact, with composition X_1. The melting point of the constituent material B is lower than the melting point of material A. At a sintering temperature T_1, the sample undergoes a solid state sintering, whereas at a sintering temperature T_3, liquid phase sintering occurs.

Solid state sintering

The solid state sintering process can occur through different mass transport mechanisms which can be categorized depending on whether they promote coarsening or densification (see Fig. 2.21). The increase in the average size of the particles leads to coarsening, whilst the shrinkage of the compact leads to densification. Ideally, in order to obtain near-theoretical densities, the sintering step should only lead to densification, and coarsening should be suppressed. However it is usual for a competition between the two mechanisms to occur, and materials will experience both densification and coarsening simultaneously (Barsoum and Barsoum, 2002).

The mechanisms that promote densification (densifying mechanisms) are driven through the grain boundary and these are: grain boundary diffusion, volume diffusion, and viscous/plastic flow. The material is removed from the grain boundary region, and this leads to shrinkage. The mechanisms that promote coarsening (non-densifying mechanisms) are driven from the particle surface, and these are: surface diffusion, volume diffusion, and evaporation-condensation. Changes in the microstructure might occur,

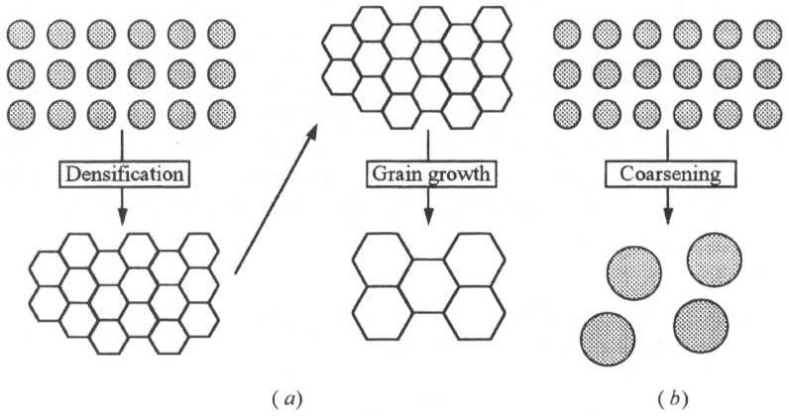

Figure 2.21: Schematic representation of two possible mechanisms: (a) Densification followed by grain growth, and (b) Coarsening.

without shrinkage. Fig. 2.22 shows the possible transport paths for two sintering particles.

Three major stages can be identified during the solid state sintering process: the initial, the intermediate, and the final stage, which can be discerned in Fig. 2.23. The initial stage is that of neck formation and grain boundary creation. The relative density increases from about 60 to 65%. The intermediate stage is that of neck growth. The relative density increases from 65 to about 90%. During the final stage the density of the sample reaches that of theoretical. During this stage grain coarsening occurs, although sintering should only result in densification.

Typical sintering temperatures for alumina powder are in the range of 1300 °C - 1600 °C. Fig. 2.24 depicts the variation of relative density with sintering temperature for a pure 0.3 μm alumina powder. The circles stand for alumina that was initially pressed, and then sintered in air at temperatures from 1350 °C up to 1550 °C for 2 h, while the triangles stand for alumina after (additionally) performing hot-pressing. It is evident that the relative density increases steadily with the sintering temperature from approx. 90 to 98% for the pressureless sintered samples, while the hot-pressed have attained a theoretical density at 1400 °C.

The effect of parameters on sintering

The key parameters that need to be controlled in order to optimize the sintering process can be classified into two main categories: the characteristics of the raw materials, and the processing characteristics (Kang, 2004):

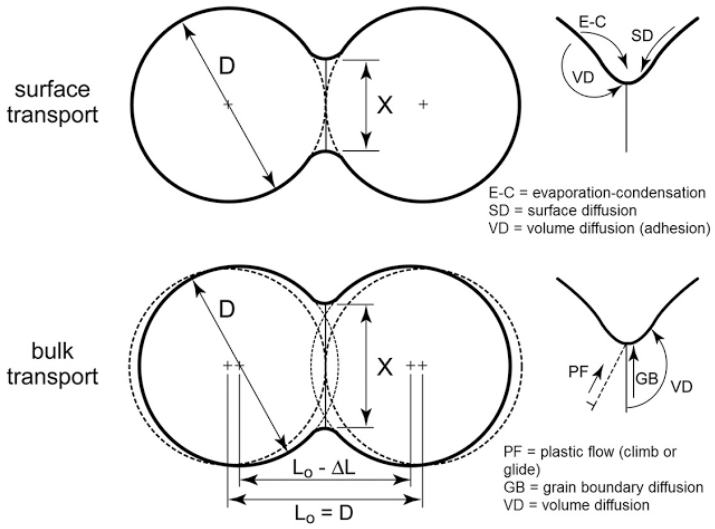

Figure 2.22: Solid state sintering mechanisms that promote coarsening (surface transport) or densification (bulk transport).

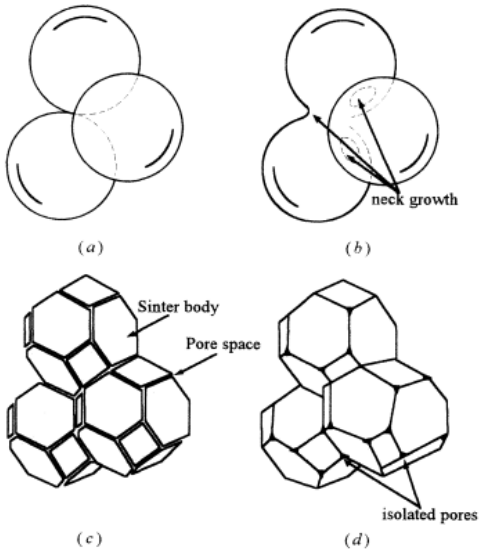

Figure 2.23: Stages of sintering process: (a) initial; (b) near end of initial; (c) intermediate; (d) final.

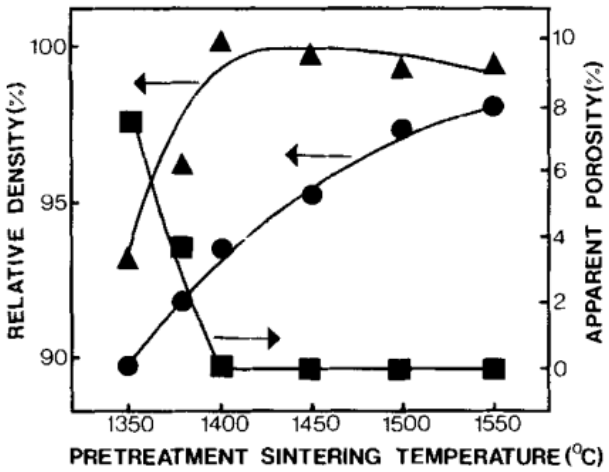

Figure 2.24: The effect of sintering temperature on the relative density of pure alumina powder before hot isostatic pressing (circles) and after hot isostatic pressing (triangles).

characteristics of raw materials these mainly include the powder characteristics such as particle size and size distribution, particle shape, and degree of agglomeration. The particle packing in the green body can be influenced by the particle shape: i.e. spherical particles require higher energy due to their shape owing the least surface area, whereas irregularly shaped particles enhance mass diffusion. In addition, the presence of agglomerated powder particles is not favoured as it might result in low green densities, and thereby low sintered densities.

The size of the particles also affects the degree of space, and the size distribution can influence the amount of porosity: small particles can fill the voids that are formed between the bigger particles. It can be deduced from Fig. 2.25 that in the case of sintering a bimodal mixture of powders, a maximum packing density can be achieved for a composition that involves both fine and coarse particles; the small particles are packed in the space between the large particles and the pores are filled (case iii). For 100% small particles (case i) or 100% large particles (case v), the packing density is the lowest.

processing characteristics these include the sintering temperature and time, sintering pressure and atmosphere, heating and cooling rates. For example, oxide ceramics are simply sintered in air, non-oxide ceramics are sintered under vacuum, whereas metallic samples require sintering in nitrogen (inert gas), or hydrogen (reducing agent) or a mixture

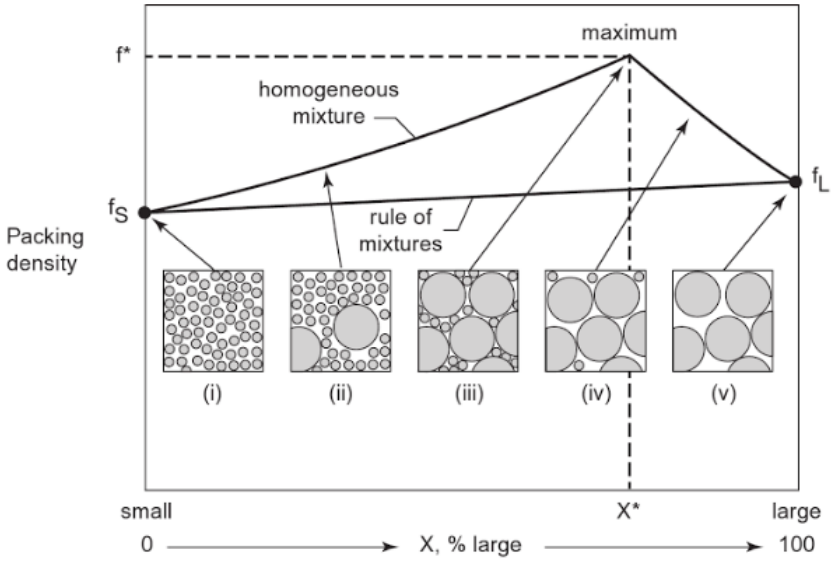

Figure 2.25: Packing density versus composition for a bimodal mixture of powders.

of gases such as Ar/H_2. Further, high sintering temperatures tend to enhance the mechanisms that promote densification.

2.4 Metal-particle/ceramic-matrix composites

2.4.1 Theoretical Considerations

2.4.1.1 Crack Propagation during fracture

The fracture toughness of ceramic-based composite materials has shown a significant improvement over the pure ceramic matrix material in several systems that have been studied over the past few years (Donald and McMillan, 1976). This section will provide the theoretical background for the toughening mechanisms that are activated due to the dispersion of the second-phase inclusions in the brittle ceramic matrix. Two different approaches can be followed to describe the effect of the distributed particles on the augmented toughness response: (a) the changing of the crack path (mechanisms of crack deflection, crack bowing, crack branching), or (b) the bridging of the tip of the crack. The different toughening mechanisms might be activated separately or in conjunction (Rödel, 1992).

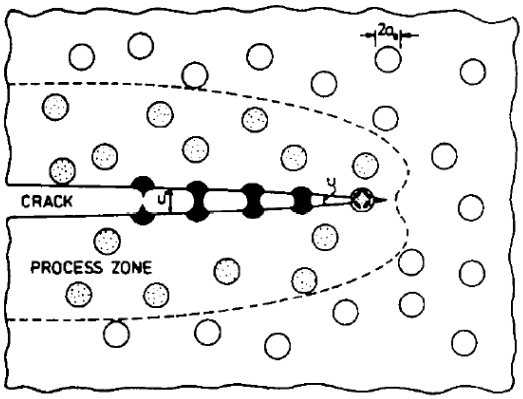

Figure 2.26: Ductile particles in a brittle matrix; note how they stretch as the crack opens.

The incorporation of ductile inclusions into brittle solids has been suggested to contribute to the toughness response of the material and is based on the assumption that the inclusions can be plastically deformed in order to bridge the propagating crack, and stretch until they fracture of decohere (Krstic, 1983; Sigl et al., 1988). The stress, σ_u, carried by the stretching particle is a function of the force, F, and the radius of the particle, α_o, (Ashby, Blunt, and Bannister, 1989):

$$\sigma_u = \frac{F(u)}{\pi \alpha_o^2} \,. \tag{2.27}$$

The function $\sigma(u)$ is directly related to the toughness increase of the composite:

$$\Delta G_C = V_f \int_0^{u^*} \sigma(u) du \,, \tag{2.28}$$

where V_f is the area fraction of the ductile material intercepted by the crack and u^* is the crack opening when the ductile particle fails (Fig. 2.26). A requirement for the bridging of the crack by the ductile inclusions is the partially debonded interface between the particles and the matrix, termed as "satisfactory" bonding. The ideal bonding between the two phases has been extensively studied from that perspective: a weak bonding between the particles and the matrix usually results in a weak contribution to the toughening, whereas a strong bonding imposes constraints on the particles. Neither of these extreme cases appear to exploit the full toughening potential of the ductile inclusions.

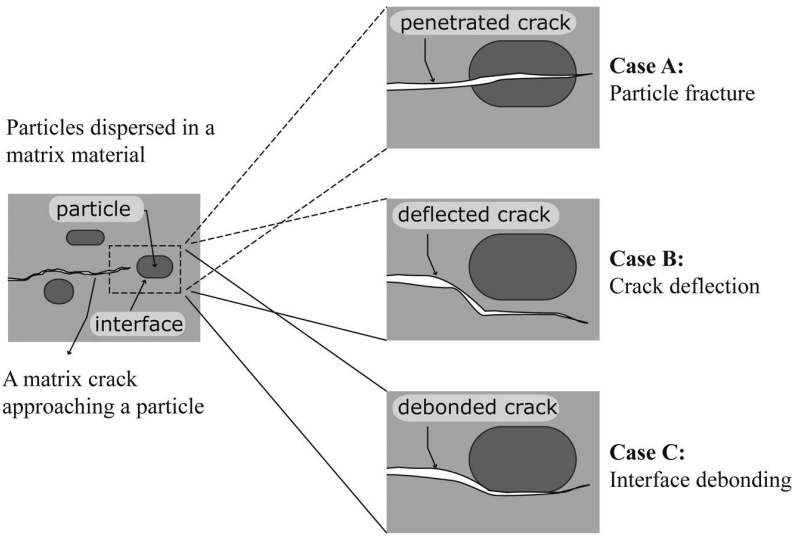

Figure 2.27: Crack-particle interaction in a particulate system showing three possible fracture mechanisms, namely particle fracture, crack deflection and interface debonding.

Other possible toughening mechanisms include the branching of the crack throughout the matrix material (Gao and Wang, 1990), the bowing of the crack between the dispersed particles (Green, 1983), the propagation of the crack along the interface, the deflection of the crack around the second-phase inclusions (Faber and Evans, 1983a; Faber and Evans, 1983b) which are considered as inhomogeneities in the structure, see Fig. 2.27. Although these mechanisms are reported to be less effective in comparison to the plastic deformation of the ductile particles, they rely on the increased tortuosity of the crack path and enhance the fracture resistance of the composite material.

2.4.1.2 Particle/Matrix Property Mismatch

The elastic moduli and thermal expansion coefficient mismatch between the second-phase inclusions and the matrix, and their effect on the propagation of the crack, have been extensively studied due to the major differences between the metallic and the ceramic phases (Khaund, Krstic, and Nicholson, 1977). Internal residual stresses might be developed in the matrix during cooling, after the sintering process, and these are attributed to differences in CTE (see Fig. 2.28 for some common ceramic matrix materials such as Al_2O_3, and common metallic reinforcement such as Cu and W). The solution for this stress, σ, can be calculated by employing the following relation (Selsing, 1961):

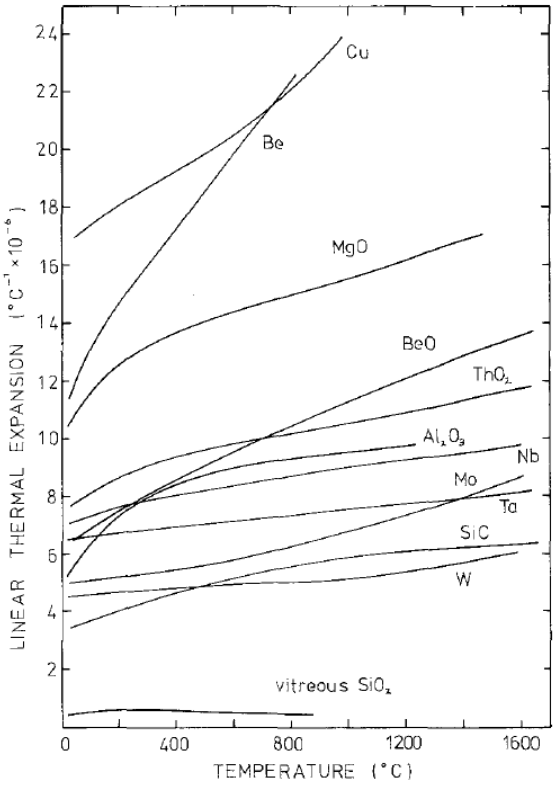

Figure 2.28: Variation of thermal expansion coefficient with temperature for various materials

$$\sigma = \Delta\alpha \Delta T \left(\frac{1+\nu_m}{2E_m} + \frac{1-2\nu_f}{E_f} \right)^{-1}, \tag{2.29}$$

where $\Delta\alpha$ is the CTE difference, ΔT is the temperature difference, E_m, E_f are the Young's moduli, and ν_m, ν_f are the Poisson's ratio of the matrix and filler, respectively.

Early studies on the propagation of a crack through a matrix material with dispersed particles included that of Davidge and Green, 1968 who studied two-phase glass-matrix materials with different CTE and E values. It was concluded that the thermal and elastic mismatch between constituent phases should be avoided. A major contribution was also that of Tirosh and Tetelman, 1976 who used a commercial rubber sheet and demonstrated the propagation of a crack in the vicinity of a disturbance (cavity or second-phase inclusion) that is weakly or strongly bonded to the matrix. Fig. 2.29 illustrates the crack arrest by a hole (case a), or the crack that bypasses the

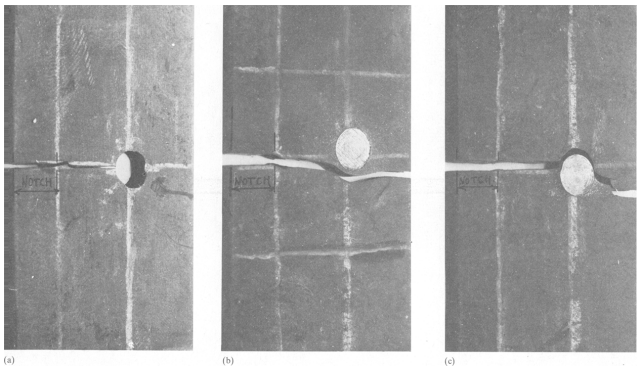

Figure 2.29: Fracture of a pre-notched rubber sheet with (a) a hole, (b) a perfect bonding of rigid inclusion and (c) weakly bonded inclusion.

inclusion due to perfect bonding (case b), or the crack propagation along a weak inclusion/matrix interface (case c).

Similar observations have been reported in different studies, by highlighting the importance of the metal/ceramic interface that determines the path of the propagating crack: either via the interface (weak bonding, negligible contribution to toughening), or through the particle, or by avoiding the particles and propagating only through the matrix (strong bonding, limited deformation of inclusions) (Bao and Chung-Yuen, 1990). Two glass-matrix composites with partly oxidized nickel or aluminum particles were used in the work of Krstic, Nicholson, and Hoagland, 1981 who studied the effect of thermoelastic properties mismatch on the interfacial bonding and the toughening of the brittle ceramic matrix by metallic inclusions. It was concluded that for metal/ceramic systems with a large thermal and elastic mismatch a poor interfacial bonding is usually formed (Krstic, 1983).

2.4.1.3 Metal/ceramic interface

As discussed earlier, in addition to the mismatch of the thermal and elastic properties, the interface of metal/ceramic composites is of great importance. The term interface is used to describe the surface between the reinforcement and the matrix material. It is a parameter that reflects the cohesion between the constituent phases, and controls the load transfer from the matrix to the second-phase inclusions. Hence, the overall mechanical properties of the fabricated composites may be affected by the interface.

The bonding between the two phases and the wettability of the particles by the matrix are two distinct factors closely related to term of the interface

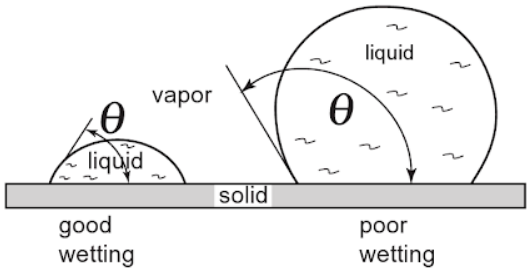

Figure 2.30: Wetting behavior for a liquid material on a horizontal plane of a solid material showing a low contact angle that supports wetting, in contrast to a high contact angle that resists wetting.

of metal/ceramic materials. The bonding between the matrix and the reinforcement can be mechanical, physical, chemical (Chawla, 2013b). The mechanical bonding can be correlated to the CTE differences and the contraction of phases. When the expansion of the matrix is higher than the inclusions, a mechanical bonding is formed, whilst when the expansion of the matrix is lower a mechanical bonding is not possible (Xia and Terence, 1994). The physical bonding might include weak forces, secondary or van der Waals forces, or hydrogen bonding, while the chemical bonding can include all types of bonding, i.e. covalent, ionic, metallic.

The wettability of liquids on a solid surface (i.e. the ability of liquids to spread on a solid surface) is rather important for the interface, and can be determined via the sessile drop technique:

$$\gamma_{SL} = \gamma_{SV} - \gamma_{LV} \cos\theta \,, \tag{2.30}$$

where γ_{SL} is the interfacial energy of the solid-liquid, γ_{SV} and γ_{LV} are the surface energies of the solid and the liquid phase, and θ is the contact angle. Two different cases are demonstrated in Fig. 2.30, depending on the value of the contact angle θ. A low contact angle (good wetting) induces the liquid material to spread over the grains of the solid material, while a high contact angle indicates a poor wetting.

It is well known that liquid metals usually do not wet the alumina ceramic (contact angle > 90°), and therefore the wettability is not sufficient for high densification of these composites during LPS (Nikolopoulos and Agathopoulos, 1992). The contact angle formed by some common liquid metals and polycrystalline alumina as a function of temperature is shown in Fig. 2.31. It can be observed that values above 100° are reported for silver, copper, nickel, and iron. The composite structure of Cu-Al_2O_3 in particular, has a contact

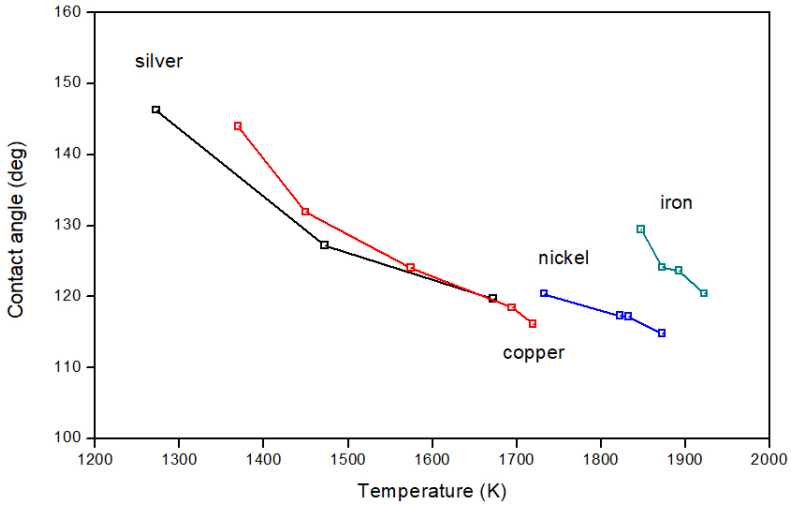

Figure 2.31: Effect of temperature on the contact angles formed by some liquid metals on polycrystalline alumina.

angle of 143° for a temperature that is just above the melting point of copper (1370 K), and a contact angle of 116° for a temperature of 1720 K (approx. 1447 °C) which is just below the sintering temperature for this study (Table 2.4).

2.4.1.4 Porosity in metal/ceramic composites

Porosity is a major issue not only in pure ceramic materials, but also in ceramic-based composites. The evolution of porosity for particle-reinforced metal/ceramic composites fabricated via pressureless sintering was studied in the work of Pines and Bruck, 2006 who selected nickel and alumina powders to prepare and study various compositions ranging from 0 vol.% Ni up to 100 vol.% Ni. They proposed two models in that work: the first model assumed that the residual porosity is associated only with the matrix material, see Fig. 2.32a, while the second model suggested that a fraction of the porosity is associated with the presence of the second-phase inclusions in the matrix and their degree of agglomeration, see Fig. 2.32b.

2.5 Metal/Al_2O_3 composites in practice

The fabrication of composite materials consisting of an alumina matrix reinforced with metallic particles is a research field that has drawn an enormous

Table 2.4: Contact angles in Al_2O_3/liquid-copper systems for different temperatures.

Temperature (K)	Contact angle (degree)
1370	143.87 ± 2.82
1450	131.86 ± 2.66
1575	123.97 ± 2.30
1695	118.42 ± 1.42
1720	116.10 ± 1.19

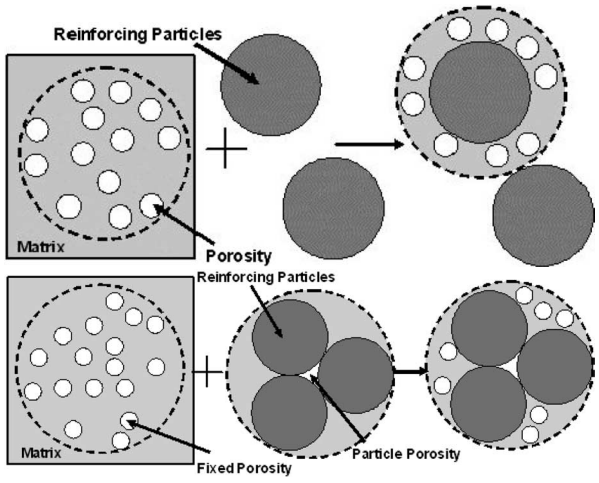

Figure 2.32: Porosity models: (I) All porosity is associated with the matrix. (II) An amount of porosity is associated to the matrix, and all remaining porosity is associated with the particles.

attention over the past few years (Moya, Lopez-Esteban, and Pecharromán, 2007).

It is well known that the increase in the volume fraction of the second-phase reinforcement has an impact on the sinterability of the matrix material. The inclusions hinder the densification process and contribute to the residual porosity of the matrix after sintering. This can take place either near the inclusions surrounding them, or within the bulk of the matrix. In addition, agglomerated particle regions might be formed with the further increase in particle volume fraction. The poor wetting of the ceramic matrix by the metallic phase is also an issue and usually results in low density.

The majority of metal-alumina composites have been fabricated via dry pressing followed by pressureless sintering, or hot-pressing with simultaneous application of pressure and heat. Spark plasma sintering and infiltration of Al_2O_3 preforms are alternative processing routes, less frequently employed for the synthesis of metal-Al_2O_3 composites. Some studies also report the use of (modified) slip-casting techniques for the synthesis of functionally graded materials. This section will discuss the fabrication methods cited in the literature towards the preparation of metal/alumina composites in terms of densification and mechanical properties.

2.5.1 Processing methods

Dry-pressing followed by pressureless sintering

The most frequently employed fabrication method for the synthesis of metal-alumina composites is that of dry pressing at room temperature and subsequent pressureless sintering. Several studies have employed this method to prepare ceramic-based composites with a dispersion of different metallic inclusions such as nickel (Tuan and Brook, 1992), molybdenum (Konopka, Maj, and Kurzydowski, 2003), silver (Dutta, Chattopadhyaya, and Ray, 2006; Tuan and Chen, 2002), iron (Konopka and Oziebo, 2001), niobium (Lane, Biner, and Buck, 1998). However, a typical disadvantage of this processing route is the low density of the sintered parts, which usually decreases with a further increase in the metal volume fraction.

Typical examples are the studies of (Tuan and Brook, 1990) and (Chou and Tuan, 1995) for the preparation of Ni-alumina and Ag-alumina composites, respectively. The specimens were formed by cold pressing which resulted in green relative densities of 55%, followed by sintering at different temperatures. Relative densities around 91% have been achieved for the highest metal content, and a relative density of <98% has been reported for pure alumina

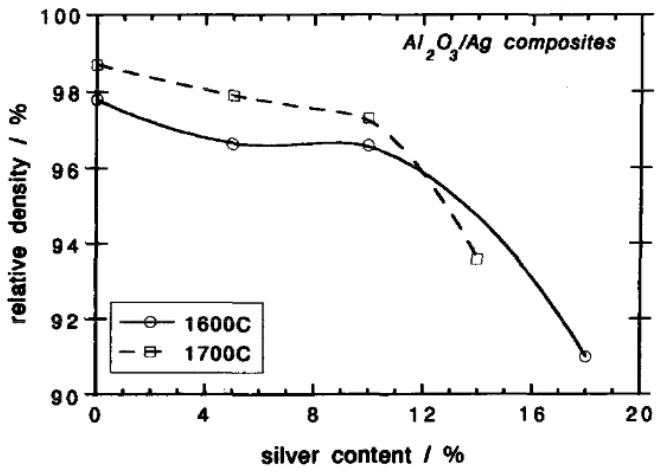

Figure 2.33: Relative density of Ag/alumina composites as a function of silver content sintered at two different temperatures.

after sintering at 1600 °C (see Fig. 2.33). The sintering temperature was found to have a mild effect on the densification process, with sintered densities at 1700 °C being slightly improved than those obtained after sintering at 1600 °C. Relative low densities of around 96% have also been reported for 5 vol.% nickel-alumina composites, after sintering at 1400 °C for 2 h (Chen and Tuan, 1999).

The effect of the sintering temperature on the density of the metal-alumina samples has been frequently cited in the literature. Indeed, low temperatures usually yield low densities for both the pure and the metal-reinforced alumina samples. A relative density of only 91% has been reported for pure alumina after sintering at 1450 °C, in contrast to densities >99% for sintering at 1550 °C. A low densification (85%) has also been achieved for 5 vol.% nickel particles and sintering at 1450 °C, in contrast to relative densities of 95% for sintering at 1500 °C, or higher (97%) for sintering at 1550 °C (Kafkaslolu and Tür, 2016).

Hot-pressing with simultaneous application of pressure and heat

Many studies have favoured hot-pressing as an alternative fabrication technique for the synthesis of alumina-matrix composites reinforced with metal particles of: chromium (Ji and Yeomans, 2002a), iron (Trusty and Yeomans, 1997), nickel (Lu et al., 2000; Fahrenholtz, Ellerby, and Loehman, 2000; Sekino, Nakajima, and Niihara, 1996; Sun and Yeomans, 1996; Breval and Pantano, 1992), molybdenum (Sbaizero and Pezzotti, 2000). The results of

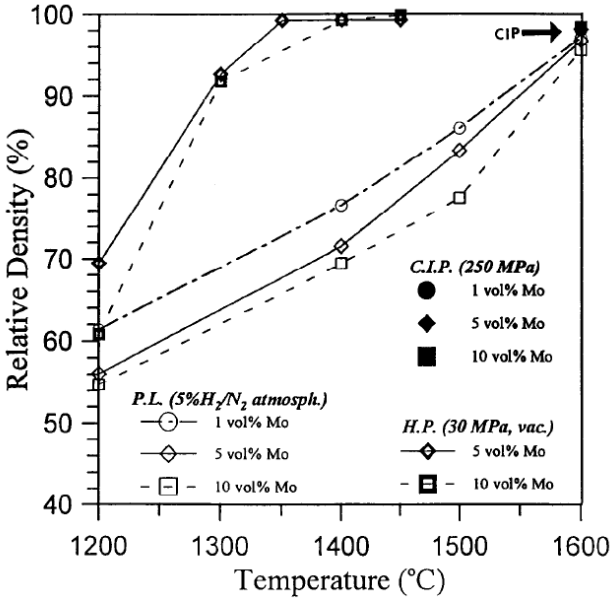

Figure 2.34: Relative density of sintered Mo/Al_2O_3 composites with various Mo contents and different processing routes.

these studies suggest that HP promotes the densification process and results in higher densities than those obtained via pressureless sintering.

Relative densities above 97% have been obtained for chromium-alumina composites, with Cr loading as high as 36 vol.%. The processing route involved sintering at 1400 °C, under a constant pressure of 30 MPa with a hold time of 30 min (Guichard, Tillement, and Mocellin, 1998).

A comparative study for the preparation of Mo/alumina composites with three different processing methods (sintering with or without hot-pressing) can be found in the work of Wei, Wang, and Cheng, 1998. It is evident from Fig. 2.34 that die-pressing followed by a hot-pressing route (HP) results in the highest values of relative density, in comparison to cold isostatic pressing and sintering (CIP) or die-pressing and sintering (PL). The hot-pressed composites can fully densify at temperatures of 1350 °C or above.

Differences in the sintered density of 20 vol.% chromium particles dispersed in Al_2O_3 matrix have also been reported in the study of Ji and Yeomans, 2002a for composites that were prepared either via conventional sintering at 1500 °C or via hot-pressing at 1400 °C. The study concluded that a better densification has been achieved via HP for both the pure Al_2O_3 matrix and the composites.

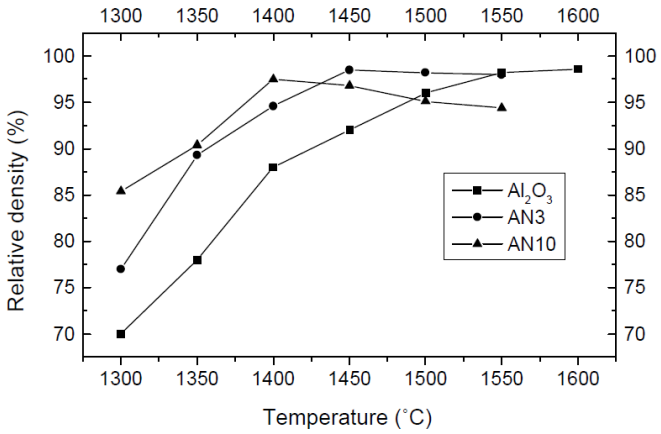

Figure 2.35: Relative density variation for Ni/Al2O3 composites with hot-pressing temperature.

Despite the followed processing route, performing the sintering cycle at different temperatures is usually attempted in order to decide the optimum temperature for the densification of the samples. A minor increase of only 50 °C (from 1400 °C to 1450 °C) has been reported to increase the fired density of Cr/alumina composites from 92% to approx. 97% (Ji and Yeomans, 2002b). Similarly, a sintering temperature of 1300 °C might result in only 70% RD, even for pure alumina hot-pressed specimens (Fig. 2.35), while densities of around 95% are only achieved for sintering temperatures above 1450 °C (Li, Huang, and Guo, 2003). Further, densities as low as 75-85% have been reached for Al_2O_3 samples at relatively low sintering temperatures (1300 °C), while near-theoretical densities have only been achieved for the lowest loading of metal phase (3 vol.%) at sintering temperatures above 1450 °C (Fig. 2.36) (Lu et al., 2000).

SPS and infiltration of alumina preforms

Despite the advantageous, near-theoretical densities derived via the hot-pressing method, its high cost and processing difficulties, as well as the limitation in the shape and complexity of the parts are major drawbacks. These have led to the exploration of alternative routes such as spark plasma sintering, and infiltration of metals into alumina preforms, in more recent years.

The spark plasma sintering is a novel technique that allows extremely high sintering rates, lower sintering temperatures and a minimum sintering time. Near theoretical densities have been achieved for nickel-alumina samples by employing the SPS method and sintering at only 1170 °C for hold time of

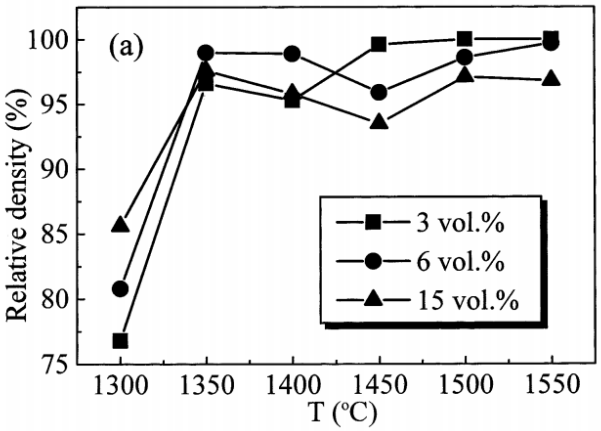

Figure 2.36: Relative density variation of nickel-alumina composites with sintering temperature.

10 min, and a fast heating rate of 200 °C/ min (Yao et al., 2005). However, this method is prone to the formation of carbides due to the sintering of the compacts in a graphite die, and the diffusion of carbon into the sample that is promoted by the applied pressure (Rodriguez-Suarez et al., 2009).

An alternative method is that of infiltration of ceramic preforms. The study of Lieberthal and Kaplan, 2001 reports the preparation of alumina slips and conventional slip-casting to produce alumina preforms, which are infiltrated with liquid salts. These are further reduced via pressureless sintering to form nickel metal particles. However, relatively poor densities were achieved (90%) due to the presence of closed pores in the matrix.

Slip-casting for the synthesis of FGMs

The slip-casting technique is a relatively new method used for the synthesis of metal/alumina composites. The alumina and the metallic powders are mixed, and a slurry is prepared with the addition of distilled water. The traditional slip-casting method has been widely used for the preparation of dense or porous ceramic composites (), however modified routes have emerged for the synthesis of metal/ceramic composite materials due to their major differences in terms of density. This variation can be exploited for the fabrication of functionally graded materials with a gradient concentration of metal particles. The composition of some slip-casting slurries and a brief description of the characteristics and processing routes are provided in this section.

A homogeneous structure with no gradient has been reported for a 5 vol.% Fe/alumina composite prepared via slip-casting of a slurry with 82.5wt% total solids content. A burn-out process was initially performed at 400 °C for 1 h in N_2 atmosphere, followed by vacuum sintering at 1470 °C for 1 h. Differences in the metal concentration between the top and bottom parts of the samples were only observed with the use of a magnetic field (Oziębło et al., 2004; Ozieblo et al., 2005).

W/alumina composites have also been prepared via slip-casting by forming a slurry of tungsten powder (1 μm) and alumina powder (0.1 μm) with total solids content of 68 wt%, and vacuum sintering at 1600 °C. Differences between as-received and oxidized tungsten powder were observed at the interface of the alumina and the tungsten phase (clear interface for as-received and gradual distribution of the heavy tungsten particles for oxidized powder) (Katayama et al., 2011).

Relevant structures have been studied for nickel-alumina composites with total solids content varying from 37-55 vol.% (Sánchez-Herencia, Hernández, and Moreno, 2006; Gizowska, Konopka, and Szafran, 2011).

Copper-alumina composites fabricated via different processing routes

Cu-Al_2O_3 composites with 5 vol.% copper have been prepared by mixing Cu powder (99.8% purity, 2 μm) and Al_2O_3 powder (CT3000SG, 0.6 μm) via two processing routes. The samples were either pressed uniaxially under 70 MPa followed by pressureless sintering at 1600 °C for 2 h, or hot-pressed to 1600 °C for 30 min. For pressureless sintering the maximum density that was obtained was 91.2%, in contrast to hot-pressing and 97.4% RD (Aldrich and Edirisinghe, 1998).

High relative densities that varied around 98-99% have been reported in the study of Oh, Sekino, and Niihara, 1998; Oh et al., 2001 for 5 vol.% Cu dispersed in the Al_2O_3 matrix. Fine powders were used (Cu powder 1 μm, Al_2O_3 powder 0.2 um) to form samples that were hot-pressed at 1400 °C - 1600 °C for 1 h under 30 MPa in Ar atmosphere.

Hot-pressing of coarse powders (Cu 30 μm, Al_2O_3 2.5 μm) that were packed in a graphite die at 1550 °C and 1650 °C for 1 h under 12 MPa pressure, in a flowing N_2 atmosphere also produced relative densities > 99% and a homogeneous distribution of copper particles (5 vol.%) with an irregular shape within a dense alumina matrix (Wang et al., 2001).

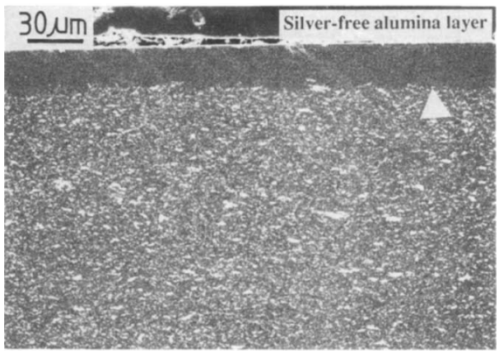

Figure 2.37: A silver-free-alumina sintered surface formed in Ag/Al_2O_3 specimens.

Pressure-assisted infiltration of molten copper into alumina preforms has also been cited in the literature, with copper phase solidifying during cooling (Travitzky, 1998).

Tungsten-alumina composites fabricated via different processing routes

High density tungsten-alumina composites have been fabricated via the hot-pressing route. The study of Sekino and Niihara, 1995 reported the preparation of W-alumina composites, with the use of tungsten-oxide powder, via hot-pressing at 1450 °C for 1 h under 30 MPa in Ar atmosphere, and relative densities over 98% for all specimens. Later, Sekino and Niihara, 1997 cited the synthesis of dense tungsten-alumina composites via hot-pressing at 1400 °C - 1600 °C under an applied pressure of 30 MPa for 1 h in Ar atmosphere by mixing fine tungsten (<0.4 μm) and alumina (<0.3 μm) powders. The spark plasma sintering has also been reported for the production of alumina-matrix composites reinforced with tungsten particles (Rodriguez-Suarez et al., 2009).

Metal-free alumina-surface

An interesting finding in the study of metal/Al_2O_3 composites relates to reports on the fabrication of silver-Al_2O_3 composite samples and the formation of a metal-free alumina surface layer after the completion of the sintering cycle (Wang, Ponton, and Marquis, 1993a; Wang, Ponton, and Marquis, 1993b; Chou and Tuan, 1995). The silver-free alumina-surface (see Fig. 2.37) formed in Ag/Al_2O_3 specimens was assigned to an increased loss in silver content due to evaporation, resulting from the high vapour pressure of molten silver at the sintering temperature.

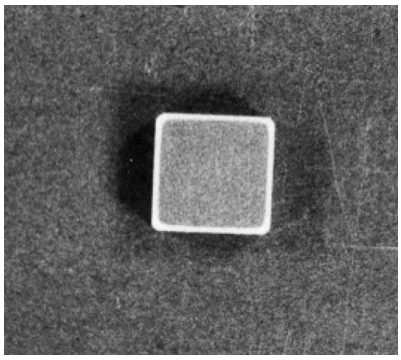

Figure 2.38: A typical rim-and-core macrostructure of an alumina/silver composite pellet.

Similar observations have been reported in the work of (Dutta et al., 2001) who stated that the evaporation of Ag after pressureless sintering at 1550 °C occurred primarily from the surface of the pellets resulting in an almost silver depleted surface layer and a silver-rich central region, as shown in Fig. 2.38, the thickness of which varied from 472 m for 1.6 vol.% Ag and decreased as the vol.% Ag increased (Dutta, Chattopadhyaya, and Ray, 2006). More recently, Chakraborty et al., 2009 studied both regions (core and skin) and cited the formation of a grade structure; i.e. that the core was more tough that the skin, and the skin was more hard than the core.

2.5.2 Mechanical properties

The fracture toughness of ceramic-based composite materials can be successfully enhanced due to the dispersion of the metallic second-phase inclusions which are usually characterized by high ductility and toughness. The dispersion of particles, however, can also decrease the stiffness of the composites given that metals usually have a much lower stiffness than ceramics. Further, the hardness of the composites also decreases due to the dispersion of the metallic phase that is softer than the hard ceramic matrix.

Fracture toughness

The majority of the studies on metal-particle reinforced alumina-matrix composites have reported an increase in the fracture toughness of the samples in comparison to the pure Al_2O_3 matrix values (Ighodaro and Okoli, 2008; Yeomans, 2008). The augmented fracture response is usually attributed to the plastic deformation of the metal particles and the activation of the crack bridging mechanism. However, the crack deflection, the crack bowing, and

the crack branching have also been found to enhance the toughness of the specimens due to the increased tortuosity of the crack path.

The presence of plastically deformed and stretched metal particles point towards the activation of the crack bridging mechanism in alumina composites reinforced with Mo particles (Sbaizero, Pezzotti, and Nishida, 1998; Simpson and Wasylyshyn, 1971). The deflection and the bridging of the advancing crack by dispersed nickel particles have been stated to improve the fracture toughness of hot-pressed alumina-matrix composites, albeit their low relative density that ranges from 97% for Al_2O_3 down to 74% for 50 wt% nickel content (Breval et al., 1992; Breval and Pantano, 1992).

Multiple types of interaction might occur simultaneously between the propagating crack and the dispersed particles in metal/ceramic composites. The deflection of the crack, the surrounding of the particle by the crack, the passing though a particle and the plastic deformation of the inclusions have been cited for Mo-alumina composites (Konopka, Maj, and Kurzydowski, 2003). The toughness enhancement has been a result of several types of interaction between the crack and the metal particles including crack deflection, crack branching, crack bridging and pull-out of the particles for hot-pressed Ni-alumina composites (Li, Huang, and Guo, 2003). Crack propagation along the metal/ceramic interface has been observed in several metal-Al_2O_3 systems, including tungsten-alumina (Sekino and Niihara, 1997), and iron-alumina composites (Konopka and Oziebo, 2001).

The weak interfaces between the molybdenum reinforcement and the alumina matrix have been reported to deteriorate the fracture toughness of the samples. It can be seen from Fig. 2.39 that small amounts of Mo particles lead to improvements in the fracture toughness, whereas higher amounts result to values that are lower than pure alumina (Diaz et al., 2003). It can also be observed from this graph that a previous study reported a different trend in the fracture toughness of the composites which verifies the viewpoint that the mechanical response of metal/ceramic composites is the result of multiple parameters and factors, and highlights the diversity of data available in the scientific literature.

Based on the previous observation, it has to be noted that many studies on similar metal-particle reinforced Al_2O_3-matrix systems have concluded that despite the initial enhancement of the fracture toughness of the samples for low metal volume fractions, a further increase in metal content deteriorates the mechanical behavior of the specimens. This can be attributed to the presence of agglomerated particles and/or a decrease in sintered density which might be accompanied with the metal content increase (Lu et al., 2000).

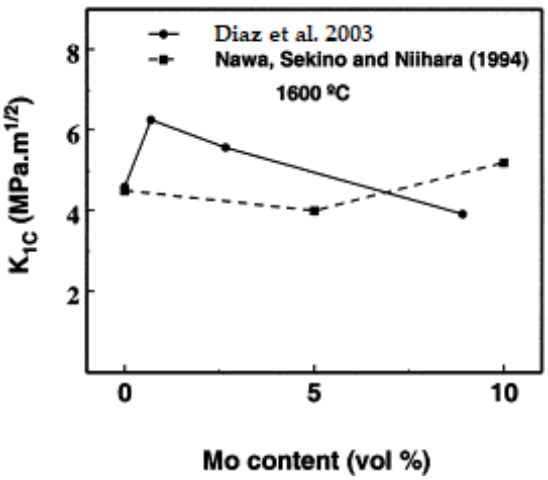

Figure 2.39: Variation of fracture toughness as a function of molybdenum content.

Fig. 2.40 portrays the fracture toughness of a Ni-alumina system (Tuan, Wu, and Yang, 1995). The toughness of alumina initially increases due to the addition of the nickel inclusions and the activation of the crack bridging and the crack deflection mechanisms. However, at 20 vol.% the inclusions are large and the density is low, leading, thus, to a deterioration of the fracture toughness response.

Modulus of elasticity

The distribution of ductile particles into the brittle alumina matrix is expected to decrease the modulus of the composite, given that the reinforcement has a lower elastic modulus than the ceramic matrix.

The published results usually concur with the theoretical predictions by applying simple rule of mixtures for alumina-matrix composites with: copper (Oh, Sekino, and Niihara, 1998; Wang et al., 2001), and molybdenum (Sbaizero and Pezzotti, 2003; Lucchini, Casto, and Sbaizero, 2003; Broniszewski et al., 2013). Similar observations have been reported for Al_2O_3 matrix reinforced with: nickel (Breval et al., 1992; Tuan, Chen, and Yang, 2007), and niobium particles (Portu et al., 2007). The Halpin-Tsai model was found to describe the results of the elastic modulus for the study of 25 vol.% Nb-Al_2O_3 (Chakraborty et al., 2000).

In other studies the elastic modulus was found to decrease further than the simple predictive formulations, and diverge from the predictions with an increase in the metal volume fraction. Lower values than anticipated have been

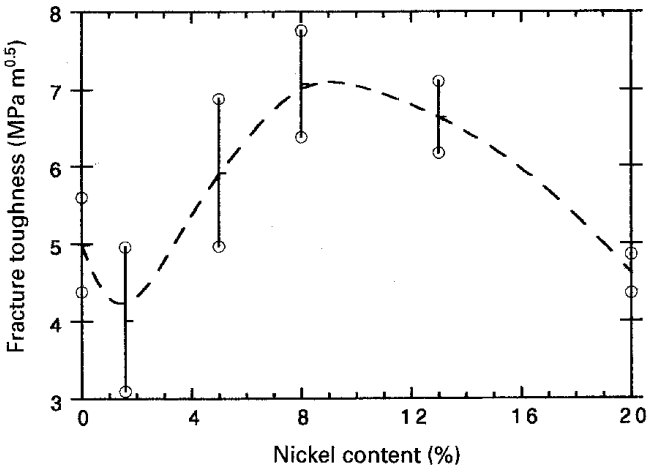

Figure 2.40: Fracture toughness of the Ni/Al_2O_3 composites as a function of nickel content.

noted in the study of Tuan and Chen, 2002 for nickel-alumina composites sintered at 1600 °C, as shown in Fig. 2.41. The lower values were attributed to the possible presence of microcracks in the composites due to CTE mismatch between the nickel particles and the alumina matrix.

The effect of both metal content and sintering conditions on the mechanical properties of the fabricated composites has been studied for hot-pressed W-alumina samples (Sekino and Niihara, 1997). For high temperature sintering at 1600 °C, degradation of properties due to grain growth and chemical reaction of tungsten were reported. The modulus values were lower than anticipated and did not obey the rule of mixtures equation, see Fig. 2.42. Despite the absence of a porosity-correction for the modulus of the matrix, the amount of total porosity was low and could, therefore, only account for a fraction of the deviation. The presence of residual stresses caused by CTE mismatch were also discussed.

A representative example of the effect of the processing route on the final structure of the composites can be found in the study of Aldridge and Yeomans, 1999. Two types of composites have been fabricated by reinforcing the Al_2O_3 matrix with 20 vol.% iron particles: one prepared via hot-pressing at 1600 °C for 30 min under 25 MPa, and one via pressureless sintering at 1700 °C for 1 h. The results showed a homogeneous distribution of iron particles within a dense Al_2O_3 matrix for the hot-pressed samples, in contrast to the conventionally sintered samples which showed increased levels of porosity. The values for the Young's modulus of the hot-pressed samples were 341 GPa,

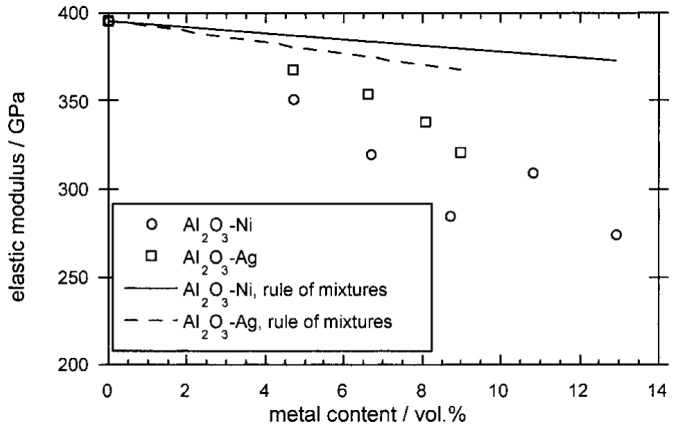

Figure 2.41: Elastic modulus as a function of metal content for Ni-alumina and Ag-alumina composites.

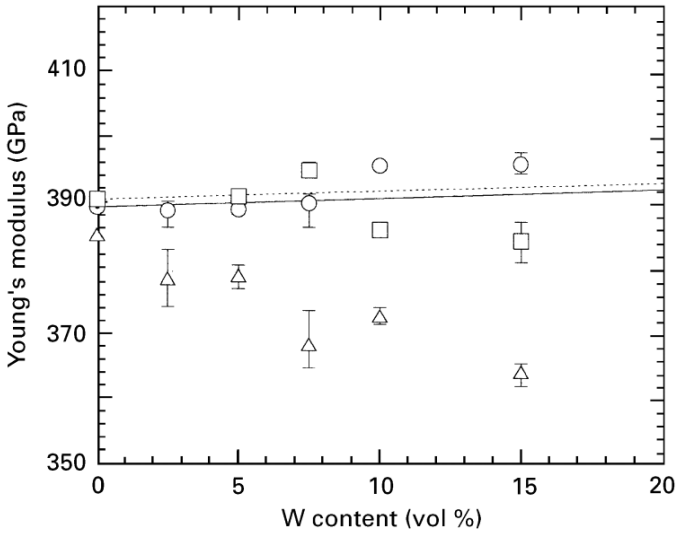

Figure 2.42: Young's modulus dependence on tungsten content for W-Al_2O_3 composites hot-pressed at three temperatures.

and in excellent agreement with the theoretical prediction of 344 GPa. On the contrary, the elastic modulus for the sintered samples was only 258 GPa, indicating a major declination of data from predictions. Despite the porosity correction (6 %) of the modulus of the matrix, the values were still lower than predictions, and were attributed to a poor interfacial bonding between the particles and the matrix. A more detailed analysis on the reasons for such behavior is given at the Appendix D of the present work.

Hardness

The hardness of the metal-Al_2O_3 composites usually decreases due to the dispersion of the ductile inclusions. The Vickers hardness of Mo-alumina composites hot-pressed at different temperatures is shown in Fig. 2.43. The data approximately obey the rule of mixtures (dotted line in graph). The hardness decrease is anticipated with the addition of the molybdenum phase of hardness lower than that of alumina. A decrease with increasing hot-pressing temperature for both Al_2O_3 and Mo/Al_2O_3 samples can also be discerned (Nawa, Sekino, and Niihara, 1994). Similar results have been reported for other metal/alumina composite systems, with an expected decrease in the overall hardness and data that approximately obey the rule of mixtures (Wang and Wei, 1998).

A degradation of hardness has been cited for tungsten-reinforced alumina composites in the study of Sekino and Niihara, 1997. Fig. 2.44 portrays the behavior of hardness with tungsten content, after sintering at three different sintering temperatures. For 1400 °C and 1500 °C the data can be roughly predicted by rule-of-mixtures, in contrast to the experimental results obtained after sintering at 1600 °C with an increased deviation from predictions.

2.6 Summary

This chapter initially presented a theoretical background concerning ceramic (Al_2O_3) and metallic (Cu, W) materials and noted important physical, mechanical and thermal properties. A brief description of composite materials, including micromechanics, was given and the importance of predicting their properties was highlighted.

The methodology for the synthesis of ceramics and ceramic-based composite materials was analyzed and the major steps including raw material selection, shaping techniques, debinding and sintering were investigated.

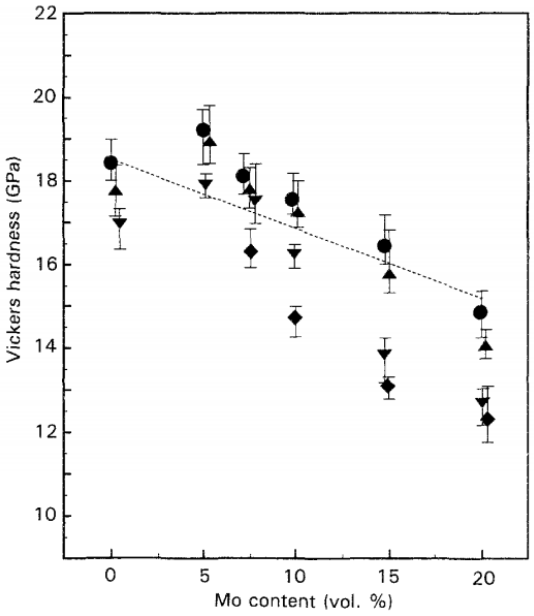

Figure 2.43: Variation of Vickers hardness with molybdenum content for Mo/alumina composites hot-pressed at different temperatures.

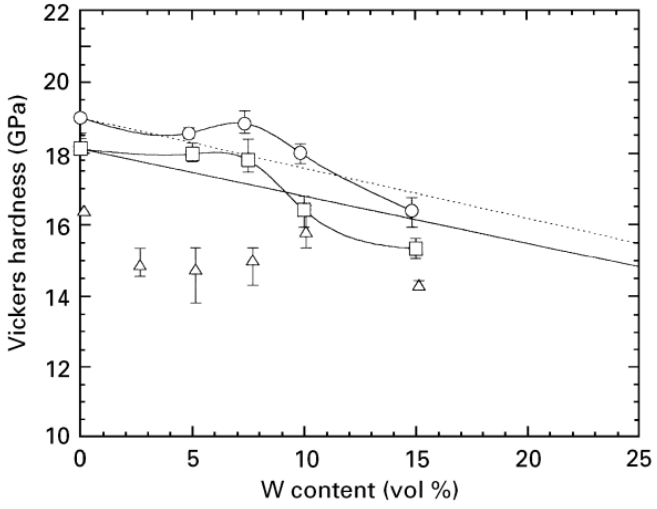

Figure 2.44: Variation of Vickers hardness with tungsten content and hot-pressing temperature for W/Al_2O_3 composites.

A theoretical background was given for metal-ceramic composites including the propagation of the crack and its interaction with the second-phase inclusions, the activation of different toughening mechanisms, and the importance of property mismatch and metal/ceramic interface. A review of the scientific literature concerning metal reinforced alumina-matrix composites was presented through the introduction of selected reports and studies. The processing methods that were employed, the resulting microstructure and mechanical properties were also cited.

It can be concluded that different processing routes can be employed for the fabrication of metal-Al_2O_3 composites. The optimization of each technique is of vital importance in order to obtain fully dense samples with augmented mechanical response. The resulting microstructure is the cumulative effect of a number of parameters that include both the powder characteristics and the processing characteristics.

3 Experimental Approach

3.1 Introduction

This chapter presents the experimental methods that have been followed for the synthesis of the different compositions (Al_2O_3, Cu-Al_2O_3, W-Al_2O_3, Cu-W-Al_2O_3), the characterization techniques, and the methods for the determination of the mechanical response. The first section outlines the fabrication process and discusses the steps: the materials that have been used, the slurry preparation, the casting, demolding and drying steps to produce green specimens, followed by debinding and sintering cycles to form sintered parts. The next section discusses the characterization of the initial raw powder materials, and the green and sintered samples in terms of density and microstructure. The experiments that have been conducted to determine the mechanical behavior of the composites, including elastic modulus, impact strength, hardness are also presented in the last section of this chapter.

3.2 Preparation of composites

3.2.1 Materials

The powder materials that have been used for the metal/Al_2O_3 composites were aluminum oxide, used as the ceramic matrix, and tungsten and copper powder, used as a reinforcement:

alumina A fully ground thermally reactive alumina with a mono-modal distribution, CT 3000 SG Almatis, was used in the present study. Almatis reactive aluminas have a number of advantages: high fired densities, good green machining properties, low sintering temperatures, controlled shrinkage, uniform microstructure, good corrosion and thermal shock resistance, excellent mechanical wear resistance and strength. These characteristics help to meet the demanding requirements of different sectors; technical and engineering ceramics, such as engine and pump parts, cutting tools, electronic ceramics, ceramic insulators.

Table 3.1: Characteristics of ceramic powder: α-alumina Almatis CT3000SG (as provided by the manufacturer).

Properties / method	**Typical Values**
Specific Surface Area / BET [$m^2\,g^{-1}$]	7.5
Particle Size / D50 [μm]	0.5
Particle Size / D90 [μm]	2.0
Press Density / 90 MPa [$g\,cm^{-3}$]	2.23
Fired Density [$g\,cm^{-3}$]	3.91
Firing Temperature / 1 h [°C]	1540
Shrinkage [%]	17.1

According to the manufacturers data, the alumina powder is of high purity (99.8%), with a typical particle size of 0.5 μm (Table 3.1).

tungsten The tungsten metal powder (WMP-D), supplied by H.C. Starck, is a soft, agglomerated powder with excellent cold pressing behavior and, in connection with additional components, improved mixing properties. The powder is of high purity (99.68%) owing a Fisher number of 0.7-0.9 μm.

copper The copper metal powder, supplied by Sandvik Osprey, is an oxygen-free high-conductivity powder with Cu $\geq$ 99.99% and O $\leq$ 0.15%, and a particle size distribution of 0 - 53 μm for most particles (98-100%) and 53 - 500 μm for the rest (0-2%).

A commercially available deflocculant was used to modify the electrical charge of alumina, so that the Al_2O_3 particles repel each other. Dolapix CE 64 (Zschimmer & Schwarz) is an organic water-miscible deflocculating agent (its chemical structure is shown in Fig. 3.1), free from alkali, that does not foam and is frequently employed for that purpose in slip-casting slurries. Its residue upon ignition is low (max. 0.1%), and suggested amount is in the order of 0.1-0.5% of the solids content.

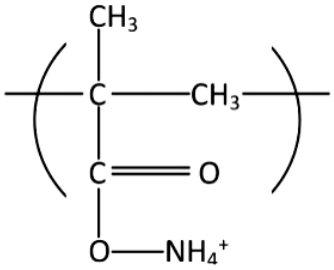

Figure 3.1: Chemical structure of the Dolapix CE64 deflocculant used in the slip-casting slurries.

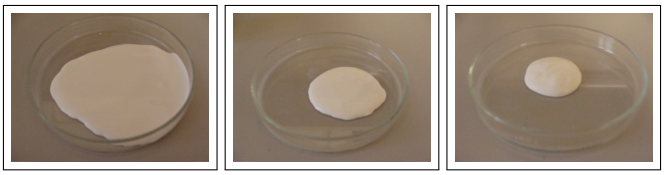

Figure 3.2: Images of the alumina slurries with (a) 72 wt.%, (b) 75wt.%, and (c) 80 wt.% solids content.

3.2.2 Compositions and preparation of slurries

Four different types of slurries which differ in metal volume fraction have been fabricated: pure alumina, copper-alumina, tungsten-alumina, and tungsten-copper-alumina composites, see Table 3.2. The theoretical density of each composite material was calculated using Eq. 2.13. The proportions of the powder materials were calculated by employing Eqs. 2.15 and 2.16, and by taking the theoretical densities as (Cardarelli, 2008):

alumina powder $3.987\,\mathrm{g\,cm^{-3}}$

copper powder $8.941\,\mathrm{g\,cm^{-3}}$

tungsten powder $19.293\,\mathrm{g\,cm^{-3}}$

Typical compositions of alumina slip-casting slurries that can be found in the scientific literature suggest 40-50 vol.% alumina powder, and 60-50 vol.% water (Table 2.3). Based on this suggestion, three different slurries were initially prepared, as listed in Table 3.3. The first slurry was composed of approximately 40 vol.% alumina and 60 vol.% water, in order to cover the lower suggested limit. The prepared slip had a good flow, but was considered liquid enough to allow the increase in the amount of the Al_2O_3 powder. The second slurry consisted of approx. 44 vol.% alumina, and was also satisfactory in terms of fluidity. In order to cover the upper suggested limit, a third slurry was also prepared, which consisted of approx. 51 vol.% alumina and 49 vol.% water. However, it was too thick and had no flow. Therefore the intermediate “recipe" was chosen in order to proceed with the experiments (Fig. 3.2).

Table 3.2: Composition in volume fraction and weight fraction, and theoretical density for the Cu/Al_2O_3, W-Al_2O_3, and W-Cu-Al_2O_3 composite samples.

Composite type	**metal volume fraction (%)**	**metal weight fraction (%)**	ρ^{theor} **(g cm^{-3})**
Al_2O_3	0	0	3.987
1Cu	1.0	2.22	4.037
3Cu	3.0	6.49	4.136
5Cu	5.0	10.56	4.235
8Cu	8.0	16.32	4.383
10Cu	10.0	19.95	4.482
05W	0.5	2.37	4.064
2W	2.0	8.99	4.293
4W	4.0	16.78	4.599
6W	6.0	23.60	4.905
1Cu - 1W	1.0 -1.0	2.13 - 4.60	4.189
3Cu - 01W	3.0 - 0.1	6.46 - 0.46	4.151
5Cu - 1W	5.0 - 1.0	10.19 - 4.40	4.388
10Cu - 05W	10.0 - 0.5	19.61 - 2.12	4.559
10Cu - 5W	10.0 - 5.0	17.04 - 18.38	5.248
20Cu - 2W	20.0 - 2.0	33.84 - 7.30	5.284

Table 3.3: Different compositions of alumina slurries for the slip-casting technique.

		Concentration	
Trials	**Material**	**wt.%**	**vol.%**
1	Alumina / Water	72 / 28	39.9 / 60.1
2	Alumina / Water	75 / 25	43.6 / 56.4
3	Alumina / Water	80 / 20	50.8 / 49.2

Another important step involved in the preparation of the slurries concerned the amount of the organic deflocculant, which was determined by preparing a test batch of pure alumina slurry and adding the organic drop-by-drop. It is known that the amount of organic additives should be kept as low as possible, and the producer's suggestion is 0.1 - 0.5 %, which translates to as low as 0.1 g for 20 g of alumina powder. Indeed, this amount was considered adequate as depicted in Fig. 3.3 which shows the appearance of the alumina slurries with different amounts of the deflocculant. The behavior of the slurry, as a function of the amount of the deflocculant, was:

no drop (0 gr) flocculated slurry and sticky behavior

1 drop (0.035 gr) flocculated slurry

2 drops (0.070 gr) deflocculated slurry but thick

3 drops (0.105 gr) deflocculated slurry with satisfactory flow

Based on these calculations and trials, different compositions were prepared by taking the appropriate amounts of powders, water and deflocculant. The slurries were homogenized in polyethylene bottles, with alumina balls, by utilising a laboratory flat horizontal shaker (HS 260 Basic, IKA), see Fig. 3.4. They were, then, sonicated (UP200S, Hielscher Ultrasonics) and cast into Plaster-of-Paris moulds to fabricate rod-shaped cylindrical samples with dimensions of around 5 mm in diameter and 50 mm in length. The required time for the mixing process was decided based on macroscopic observations and sedimentation rates, as well as in terms of a time-effective processing route.

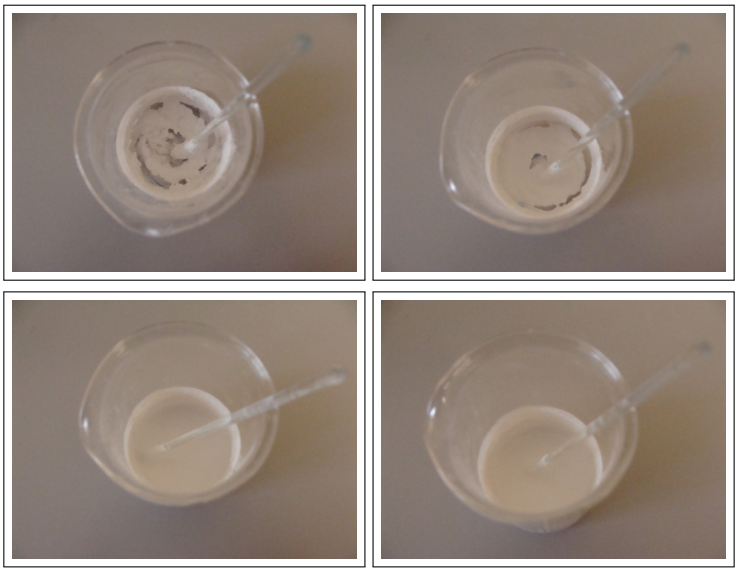

Figure 3.3: Images of the 75 wt.% alumina suspension with no deflocculant, 1 drop, 2 drops, and 3 drops (from top to bottom).

3.2.3 Mold preparation

The molds were prepared with distilled water and Plaster of Paris gypsum in appropriate proportions to form a slurry that was mixed for 3 min by hand. During this time, the consistency of the slurry changed from liquid to a thick solution. The solution was poured into a shaped prototype, and rubber bands were used to seal the pieces during the thickening of the mold.

The drying of the mold required approximately 20 min, during which the plaster become warmer. The formed piece was removed from the model, was placed for 2 min in water bath, and it was then left to dry on a filter paper. A similar process was followed for the production of the second half of the mold. The two-piece fabricated gypsum molds were left to dry for 72 h under ambient conditions. A top-view of a mold that was prepared to produce the rod-shaped cylindrical samples is shown in (Fig. 3.4).

3.2.4 Casting and drying

The next step of the experimental procedure is that of casting. The two-piece-molds should be clean and dry, and both surfaces should be slightly moistened with water to enhance the water absorbency from the slurry, and enable the capillary process. It is also is important for the pinholes of the mold to be aligned in order to ensure that it is properly sealed. For that

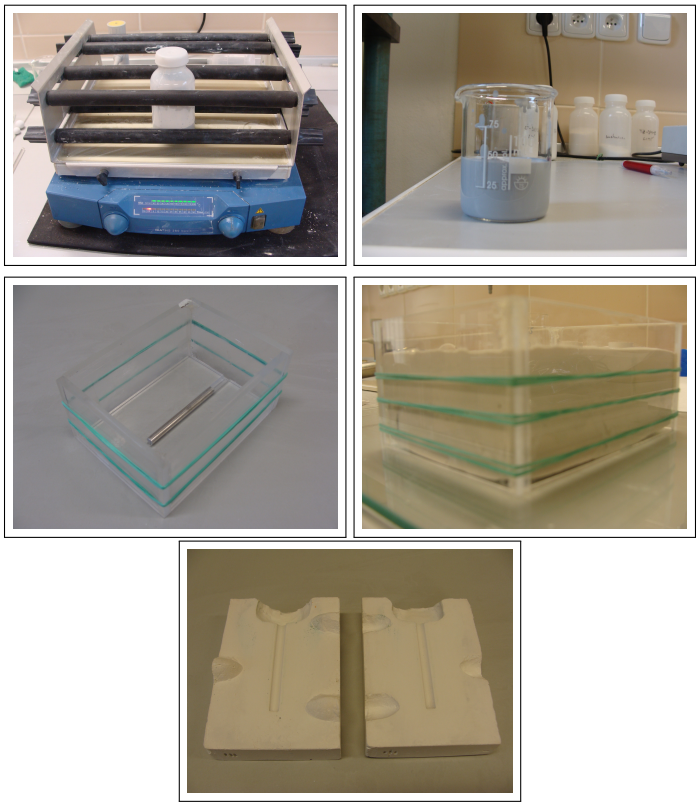

Figure 3.4: Laboratory shaker for homogenization of slurry in PE bottle, W/Al_2O_3 slurry, Plexiglas prototype used to make the molds, and top-view image of PoP mold.

purpose rubber bands are used to avoid any leakage of the slurry from the mold.

The slurry is slowly poured into the mold, to avoid the formation of any bubbles that might be created in the case of a fast casting. The mold is constantly filled, however, the level of the slip changes with time. The water of the slurry is absorbed instantaneously by the mold due to capillary forces, and attention is required in order to constantly add more slip in order to avoid the formation of a hollow (tube) sample.

After the casting step has been completed, a solid body begins to form against the mold walls. A sequence of images at various time intervals, after the slip was poured into the mold, is illustrated in Fig. 3.5. The absorbance of water with time is evident, and distinct rings can be easily observed due to color changes. The inner region represents the liquid slip, while the outer is a dried solid that has expelled the excess amount of water.

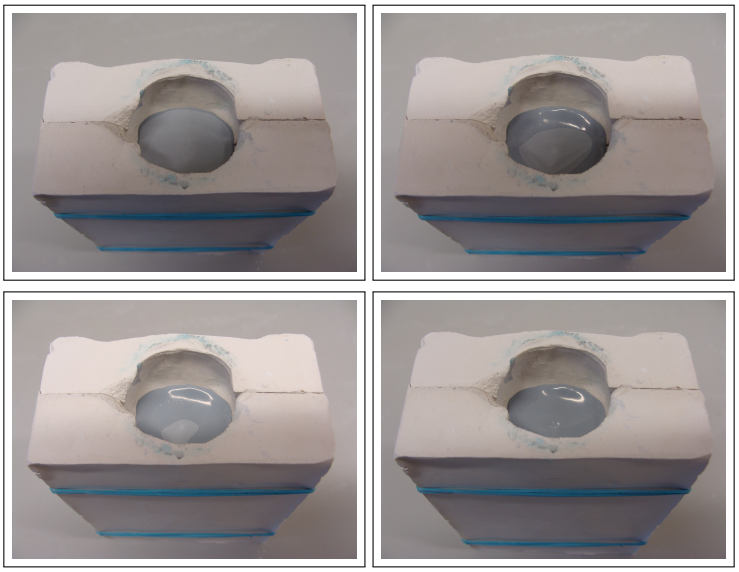

Figure 3.5: Sequence of time-dependent images of the slip-casting process. A dense layer begins to form next to the mold surface, the layer continues to thicken and the interior remains liquid, until total drying.

The demolding of the specimens can take place several minutes after the casting of the slip has been completed. The time depends on the slurry consistency and the mold characteristics. The green sample should be easily removed from the mold at that point. The drying of the sample into the mold is a rather critical step of the fabrication process, and the correct demolding time translates to an easy removal of the green sample due to shrinkage. A fast demolding might result in a sample that has not been properly dried, and therefore is not easy to handle.

The drying of the molds between the castings is of paramount importance. The molds are usually let to dry in room temperature for 24 h, but drying can also be hastened by placing them into a drying oven for a hew hours in order to accelerate the production process. It is critical to maintain the drying temperature below 40 °C to prevent any damage of the molds by the possible decomposition of the calcium sulfate dihydrate; the main constituent of Plaster of Paris.

Drying is another important step in the process of fabricating ceramic and ceramic-based materials. During this step a significant amount of water is removed from the sample, and this has to be a gradual process. A fast water removal could result in surface cracks or distortion of the samples.

The sequence that was realized included natural air drying of the green samples for 24 h at RT. The samples were then placed into a drying oven at 40 °C for several hours, followed by a gradual increase of temperature to 60 °C and then 80 °C. The temperature was maintained at 110 °C and the samples were only removed from oven when their weight was constant.

A fine sand paper was used to polish the surface of samples (top and bottom parts of the rod-shaped cylindrical specimens) and remove any possible contamination from the gypsum mold. The dimensions (length and diameter), as well as the mass of the green samples were noted, to allow the further calculation of the green densities and linear shrinkage of the specimens.

Experimental observations

Should we distinguish some important matters that relate to the slurry formation and the casting process, then these could be summarized as following:

slip characteristics Firstly, the density of the slips (solids content) should be rather high, and the amount of water should be as low as possible. Further, the fluidity of the slip should be adjusted accordingly; the slurry should be fluid enough to be properly poured into the mold, but not too fluid, while the successful preparation of deflocculated slurry is also a requirement.

casting samples The amount of slurry that is cast into the molds should be constant over time; a fast removal (absorbance) of water and/or not enough slurry in the mold will result in a hollow (tube) sample. Also, air bubbles might be formed during a fast casting.

green samples Attention is required to demold the green samples at a proper time, and avoid cracking inside the mold; this might happen in case the samples are left for an excess amount of time inside the molds.

3.2.5 Debinding and sintering

Prior to sintering of the green bodies, a cycle of debinding was performed under a pure dry hydrogen flow. The heating rate was adjusted to 1 °C/ min from room temperature up to a temperature of 600 °C, and the samples were maintained at this for 2 h. They were then cooled to RT with a cooling rate of 5 °C/ min. The efficiency of the heat treatment cycle and its effect on the organics that were present in the formed slurries was determined with analyzing the samples via CHNS analysis to determine any residual carbon content.

The sintering of the parts was performed under a reducing (H_2) atmosphere with a heating rate of 2 °C/ min up to a sintering temperature of 1500 °C, dwell time for 2 h, and cooling rate of 5 °C/ min. Sintering under hydrogen was realized to avoid the oxidation of the metallic reinforcement, since both metal powders are susceptible to oxidation and react with air, prohibiting, thus, a conventional sintering cycle. In addition, hydrogen sintering allows the reduction of any possible oxides that might have been formed on the surface of the green samples.

3.3 Characterization of materials and composites

Archimedes's principle; when an object is immersed in a fluid, the fluid exerts an upward force on the object that is equal to the weight of the fluid displaced by the object.

The characterization techniques that have been employed include the density measurement of the samples via mass/volume calculations and via the Archimedes' immersion technique. X-ray diffraction (XRD) has been performed for the powders, and both the green and sintered samples, as a common spectroscopy technique that reveals the chemical composition and the crystalline phases of materials.

Laser diffraction has been performed to determine the particle size and size distribution of the powders, and optical microscopy (OM) analysis to reveal the particle morphology of the powders and the structure of the sintered samples. Specific measurements were realized to determine any residual carbon content prior sintering of the samples.

The macroscopic testing methods involved the impulse excitation technique (IET) for the determination of the elastic modulus of the composites, and mechanical testing measurements via Vickers microhardness and impact strength apparatus. Prior to any analysis of the sintered parts, their visual inspection as a non-destructive evaluation technique was realized (Loehman, 2010).

3.3.1 Density measurement

The bulk volume of a material is the summation of its true volume and its total porosity which represents the volume fraction of both open and closed pores. The open porosity can be determined via the Archimedes immersion technique, and the closed porosity can be determined as an indirect assessment of the measurement.

The density of the green and sintered bodies was calculated from the weight and the dimensions of each sample. The sample mass was measured using a digital balance, and the sample volume was determined by measuring the external dimensions of the samples. The length and diameter of the rods were measured at various locations across the sample, and an average value was used.

Density by dimension and mass

For simple geometrical shapes such as rectangular bars and cylindrical rods, the bulk density, ρ_b, of a material can be determined via the mass-to-volume ratio, simply by weighing the dry material (mass) and determining the (bulk) volume via its dimensions:

$$\rho_b = \frac{\text{mass}}{\text{bulk volume}} \,. \tag{3.1}$$

Density by Buoyancy method; Archimedes' method

For a more accurate calculation, or in the case of more complex-shaped structures, the density of the samples can be determined by employing Archimedes' immersion principle, i.e. the buoyancy method[1]. The bulk density, ρ_b, is:

$$\rho_b = \frac{m_1}{m_3 - m_2} \times \rho_{fl} \,, \tag{3.2}$$

where m_1 is the mass of the (dried) sample weighted in air, m_2 is the mass of the saturated sample immersed in the fluid medium (water) after evacuation for 1 h, and (vacuum) saturation in water for 24 h, m_3 is the mass of the saturated sample in air (after being immersed in distilled water, and quickly surface-dried to avoid loss due to evaporation), and ρ_{fl} is the density of the

[1] DIN EN 993-1; Methods of test for dense shaped refractory products: Performing Density Determination using the Buoyancy Method.

Table 3.4: Temperature dependence of water density.

Temperature (°C)	**Density of water ($g\,cm^{-3}$)**
21	0.997992
22	0.997770
23	0.997538
24	0.997296
25	0.997044

medium (water) at a specific temperature (Table 3.4). The open/apparent porosity, expressed in % can be calculated via the equation:

$$P_{open} = \frac{m_3 - m_1}{m_3 - m_2} \times 100\ . \tag{3.3}$$

Linear shrinkage

The shrinkage of the specimens, during the sintering process, is an important factor of ceramic materials and can be determined empirically by:

$$\delta = \frac{\Delta L}{L_o}\ , \tag{3.4}$$

where L_o is the initial length, and $\Delta L = L - L_o$, where L is the length at a given time or temperature. The resulting ratio is negative, suggesting the decrease in length. Shrinkage is correlated to the density of the samples and is usually expressed simply by: %LS = $\delta \times 100$.

3.3.2 X-ray diffraction

X-ray diffraction is a non-destructive analytical technique used for the characterization and phase identification of crystalline materials. It provides information on the structure, phase and other structural parameters, and every XRD pattern is unique and is the fingerprint of a given material. Amorphous

materials, such as glass, do not produce sharp peaks, in contrast to other compounds that give distinct peaks. For mixtures or composite materials, the diffraction pattern is the summation of the individual diffraction patterns. It is important for a diffraction graph to contain all major peaks that are listed in a reference pattern. Further, the major peaks provided in a database should be observed in the constructed graph to verify that it is a good match.

Fundamental principles

The data from the XRD pattern can be exploited to calculate the lattice parameters of a material. Braggs law relates the wavelength, λ, to the diffraction angle, θ, and the lattice spacing, d, in a crystalline sample by:

$$n_\lambda = 2d \sin\theta. \tag{3.5}$$

The Miller indices (hkl) can then be determined by using the calculated value of spacing, d, via the equation:

$$d_{hkl} = \frac{\alpha}{\sqrt{h^2 + k^2 + l^2}}\,, \tag{3.6}$$

where α is the lattice constant.

Sample Preparation

The XRD analysis was performed with the use of a D8 Advance Bruker, with a Cu anode, and a detector with a LynxEye Ni filter. The scanning angle was between $4° \leq 2\theta \leq 80°$, the recording step was $0.02°$, and the time step $0.2\,\text{sec}$. The analysis was performed for the raw powders, as well as the fabricated green and sintered samples. The preparation required crushing a small piece of the sample, and then manual milling in agate mortar to produce a powder form of the material. The corresponding diffraction peaks were compared with the *American Mineralogist Crystal Structure Database*.

3.3.3 Determination of carbon content

Prior the sintering cycle, the possibility of any residual carbon content in the samples had to be clarified. This was accomplished by using the CHNS analysis (Vario EL Cube, Elementar GmbH) that is based on the simultaneous determination of four elements in a sample: carbon, hydrogen, nitrogen, and sulfur. The sample undergoes a high-temperature ($1200\,°\text{C}$) burning in

oxygen atmosphere which converts the elements into gaseous products. This method allows the detection of carbon in any inorganic form (CO_3^{2-}, HCO_3^-), making sure that any residue will be identified.

Sample requirements

The samples should be homogenized, and the mass should vary between 5 mg to 50 mg depending on the sample origin and composition. The detection limits of the method are < 40 ppm.

3.3.4 Laser diffraction analysis

Laser diffraction analysis, or laser diffraction spectroscopy, is an effective technique that determines the geometrical dimensions of a particle, and applies to materials ranging from hundreds of nm up to several mm in size. The analyzer measures the angle and intensity of light scattered from the particles of the sample, records the data and passes them to an algorithm. These data are then transformed into information about the particle size. Large particles scatter light at small angles, whereas small particles scatter light at large angles.

Wet and dry dispersion

The powder can either be dispersed in a liquid (wet laser diffraction), or a gas (dry laser diffraction). In the present work the wet laser diffraction was employed: a small amount of powder was dispersed in distilled water followed by ultrasonic treatment for a few minutes. The particle size distribution of the raw powders was calculated by determining all D values.

Data interpretation

There are three values that are typically used to characterize a size distribution derived via laser diffraction: the mean value that corresponds to the average value, the median value which stands for the value at which half of the population resides above this point, and half resides below this point, and the mode value which is the peak of the distribution.

The size distribution can be symmetric, in that all values are equal, and the mean, the median, and the mode values coincide (Fig. 3.6a). For non-symmetric distributions, the mean, the median, and the mode are three different values (Fig. 3.6b). In that case the non-symmetric distribution can be termed as left-skewed (the mean value is lower than the median value), or right-skewed (the mean value is greater than the median).

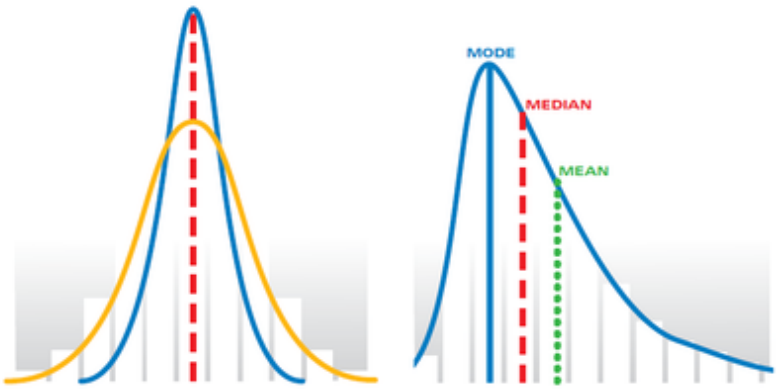

Figure 3.6: Symmetric and non-symmetric particle size distributions.

The particle size volume distribution is commonly defined by using three D-values: the D_{10}, the D_{50}, and the D_{90}. The D_{10} value, for example, is the diameter at which 10% of the particles have diameter less than this value, and the rest have a diameter higher than this value. Another common value of laser diffraction is that of span, used to express the width of the distribution, which is derived by applying the following equation:

$$\text{span} = \frac{D_{90} - D_{10}}{D_{50}} \,. \tag{3.7}$$

3.3.5 Optical microscopy

Optical microscopy is a useful tool that magnifies images of small samples and allows one to directly count and determine the size of particles ranging from less than 1 μm up to 1 mm (Fig. 3.7).

Transmitted OM for powders

There are two major types of mounting that can be followed to prepare a microscopy slide: the dry and the wet mounting. In the present study the wet mounting method was realized by placing a drop of an agitated suspension on the microscopy slide. Approximately 30 images were captured for the raw copper and tungsten powders by proper movement of the slide (Nikon Eclipse E400 POL).

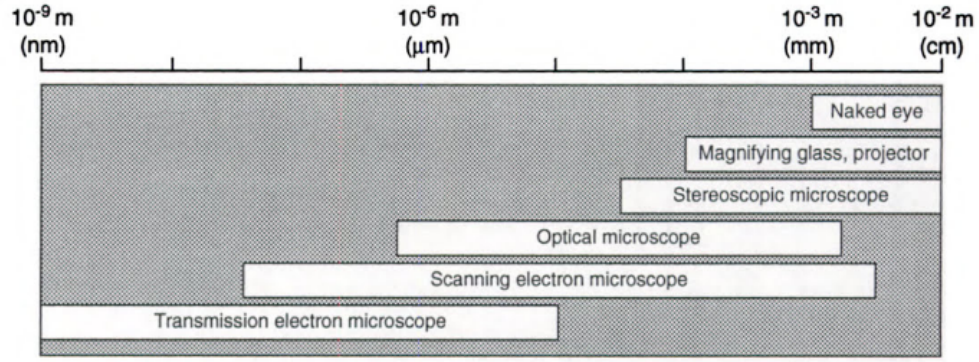

Figure 3.7: Range of microscopy.

Mounting and polishing of sintered samples

Fractions of the sintered samples were mounted in a resin to facilitate both the microstructure analysis via the optical microscope, as well as the Vickers microhardness test, see Fig. 5.1. An epoxy system composed of a resin and a hardener was used, suitable for casting and encapsulation to produce a water clear and high transparency finish. The resin system hardens at room temperature and exhibits very slow reactivity that allows the production of thick samples.

The process that was followed included the sectioning of the sintered rod-shaped cylindrical samples, followed by mounting into the resin medium. After complete curing of the resin, the cross-sections were prepared by coarse and fine grinding, followed by coarse and fine polishing of the surfaces to produce a smooth finish (DP-Paste Struers). This was performed by using a Struers Planopol V Grinder/Polisher machine, and water as a cooling media. The images that were obtained via the optical microscopy analysis were analyzed via an open source image processing program by converting them into an 8-bit type (more information on the process can be found in Appendix B).

3.4 Evaluation of Mechanical Properties

3.4.1 Elastic Modulus

IET is a non-destructive characterization technique that is employed to determine the elastic behavior of a material. It is a fast and reliable method, with a large temperature range (up to 1700 °C). The technique applies to porous and brittle specimens, and provides information about the structure and behavior of a material.

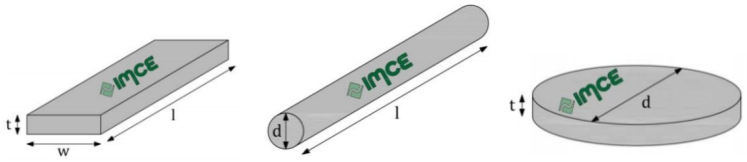

Figure 3.8: Sample shapes (rectangular bar, cylindrical rod, disc) for impulse excitation technique.

By using the resonant frequencies, the dimensions, and the mass of a sample, important parameters such as the Young's modulus, the shear modulus, Poisson's ratio and the damping coefficient can be determined. Accuracy of up to 1% can be achieved; the only parameters that introduce the uncertainty in the measurement are the ones related to the sample characteristics and these are its mass and dimensions.

The Young's modulus for a cylinder is given by:

$$E = 1.6067\left(\frac{L^3}{d^4}\right) m f_f^2 T \ , \tag{3.8}$$

where E is the Young's modulus, m is the mass, f_f is the flexural resonance frequency, L is the length, d is the diameter, and T is a correction factor.

Sample geometries and size requirements

The impulse excitation technique can be applied to a variety of specimen shapes such as rectangular bars, cylindrical rods, and discs (Fig. 3.8). For cylindrical rods in particular, only the Young's modulus values can be obtained. Table 3.5 provides some guidelines and suggested sample dimensions for IET room temperature measurements.

Measurement process

The measurement is performed by gently tapping the sample with a small hammer, as shown in Fig. 3.9. The vibration is recorded with the use of a microphone, and is then transformed into a frequency by a fast Fourier transformation (see Appendix C). An RFDA 23 IMCE (Resonant Frequency and Damping Analysis) software is used to calculate the elastic properties.

The setup that has been used in the present study is shown in Fig. 3.10. The IET measurements have been performed on all fabricated sintered samples according to ASTM E1259 (E 1876-15, 2015) (see Appendix A).

Table 3.5: Guidelines of sample dimensions for room temperature IET measurements.

Sample shape	Measured property	Advised length	Minimum length	ASTM ratio
Rectangular	E	$l \geq 50\,mm$	$l \geq 20\,mm$	$l/t \geq 5$
Rectangular	E, G, ν	$l \geq 50\,mm$	$l \geq 30\,mm$	$l/t \geq 5$, $w/t \geq 5$
Cylindrical	E	$l \geq 30\,mm$	$l \geq 20\,mm$	$l/d \geq 5$
Disc	E, G, ν	$d \geq 30\,mm$	$d \geq 20\,mm$	$d/t \geq 4$

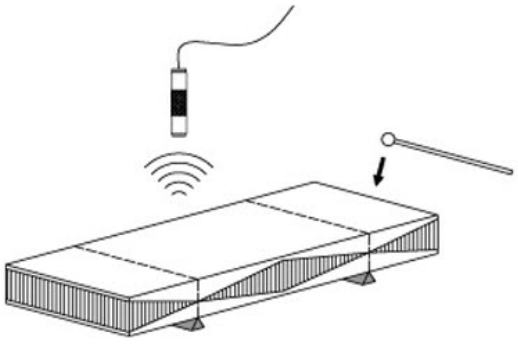

Figure 3.9: Impulse excitation technique.

Figure 3.10: Impulse excitation technique apparatus for Young's modulus evaluation.

3.4.2 Vickers MicroHardness

Hardness is an important engineering property of materials, especially ceramics, and is suitable for the evaluation of materials in terms of quality control. Hardness can also be an indicator of toughness and ductility of a structure.

Hardness tests are non-destructive, and the two types of indenters that are usually used include the Vickers and the Knoop. The loads can be low, ranging from a few g up to a few kg (micro-hardness), or higher up to 50 kg (macro-hardness) depending on the specimen dimensions. Micro-hardness is mostly suitable for microstructure gradients and macro-hardness for good average estimates.

Vickers microhardness

The Vickers hardness test was developed by Robert L. Smith and George E. Sandland in 1921.

The indentation test utilizes a square-based pyramidal-shaped diamond indenter as shown in Fig. 3.11. The hardness can be determined via the equation:

$$HV = \frac{2000F\sin(a/2)}{d^2} = 1.8544\frac{F}{d^2}\,, \tag{3.9}$$

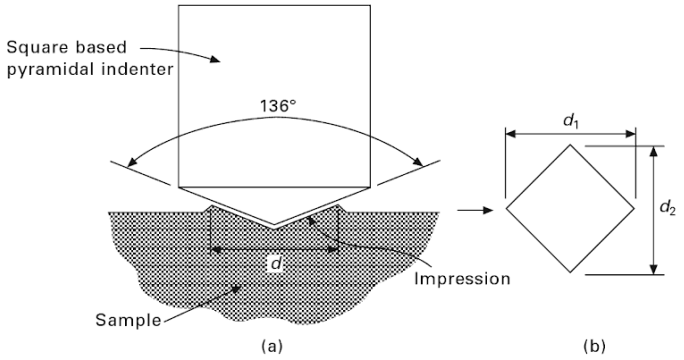

Figure 3.11: Vickers hardness test: (a) indentation, (b) impression diagonals.

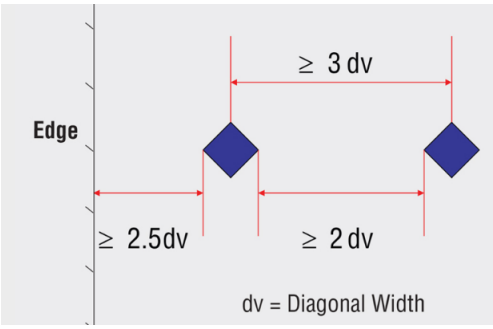

Figure 3.12: Minimum distance for the Vickers microhardness testing.

where F is the load in kgf, a is the face angle (136°), and d is the mean diagonal length (in mm).

It is important for the Vickers microhardness measurement test to maintain the minimum distance between two indentations at least 3 $\times$ the indentation's diameter. Further, the minimum distance from the indentation to the edge of the specimen should also be 3 $\times$ the indentation's diameter (see Fig. 3.12). Further, according to ASTM E384 (E 384-17, 2017), the operator should try to keep indents larger than 20 μm in length (see Appendix A).

Sample preparation & measurement

Each specimen was embedded in a resin block, as previously discussed in the optical microscopy analysis section. The indents were performed along the diameter of the cross-sections of the samples, and the distance between each subsequent measurement was such to abide by the aforementioned suggestions.

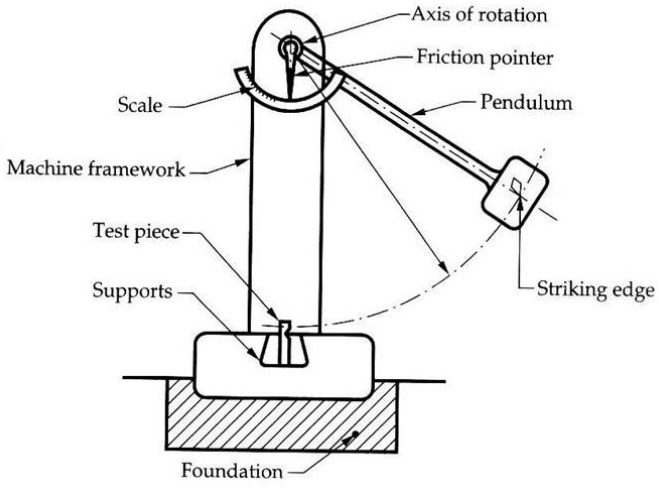

Figure 3.13: Izod impact testing apparatus.

3.4.3 Impact Strength

The Izod impact test was named for English engineer Edwin Gilbert Izod, who first described the test method in 1903.

The impact test measurement can be used to determine the impact resistance of a structure, and calculate its toughness which represents the ability of the material to absorb energy and deform plastically prior its fracture (Callister and Rethwisch, 2009). Two methods are the Charpy and the Izod impact tests, which are commonly used for the fracture evaluation of polymeric materials.

In the present study, impact test measurements were performed on the unnotched, sintered cylindrical specimens by utilizing an Izod setup similar to that of Fig. 3.13. The apparatus is comprised of a swinging pendulum that is released from a fixed position in order to strike through the specimen that is clamped into the test fixture. The kinetic energy required to initiate the fracture and to continue until the specimen is fractured is the impact energy. The amount of energy absorbed by each specimen is divided by its cross-section dimensions to yield the impact strength, expressed in $\mathrm{kJ\,m^{-2}}$ (Low, 2018).

3.5 Summary

This chapter has presented the raw powder materials that have been used for the fabrication of the Al_2O_3, Cu-Al_2O_3, W-Al_2O_3, and W-Cu-Al_2O_3 samples. The preparation of the different slurries and the overall processing route that has been followed for the synthesis of the samples were discussed. The characterization techniques that have been used throughout this study for both the powders and the samples (green and sintered) have been analyzed.

4 Characterization of Raw Powders

4.1 Introduction

The properties of the initial raw powder materials are of high importance as they have an effect on the densification process and overall sintering mechanism and resulting microstructure. For instance, a powder with a fine particle size may require a lower sintering temperature and/or a lower sintering dwell time or be sintered more efficiently, in comparison to a more coarse powder of the same material.

The characterization of a powder material might include the determination of various characteristics such as particle size and size distribution, particle morphology, and state/degree of agglomeration. The effect of these parameters has been discussed in previous sections: agglomerated powders, for example, are usually not desired as they might yield non-uniform microstructures and result in reduced sintered densities driven by various pore-rich regions (Fig. 2.10). Further, powders with a size distribution might result in the formation of sintered parts with high densities due to the presence of the smaller particles that fit in the void spaces formed by the larger particles (Fig. 2.25).

This chapter provides the results that have been obtained from the characterization of the initial (as-received) raw powder materials including the Al_2O_3 ceramic powder, and the copper and tungsten metallic powders.

4.2 X-ray diffraction analysis

The X-Ray diffraction pattern of the raw alumina powder is shown in Fig. 5.2. It can be seen that corundum has multiple peaks in the scanning angle range of 10° - 80°. These have been indexed with the theoretical angle values that

have been obtained from a database (Table 4.1), and are noted in the graph with open squares.

The XRD profiles of the copper and tungsten metallic powders are also shown in Fig. 5.2. The three characteristic peaks (up to 80°) of each metallic powder have also been matched with the database values (Table 4.1), and the illustrated squares represent the XRD pattern peaks of the reference materials.

It can be observed from these diffraction patterns that the data of the analysis of the as-received powder materials are in excellent agreement with the reference values according to the (*American Mineralogist Crystal Structure Database*), verifying, thus, the purity and crystallinity of each material.

4.3 Particle size distribution of the powders

4.3.1 Laser diffraction analysis

The particle size distribution of the as-received powders was measured using the laser particle sizer Analysette 22 Nanotec (Fritsch), a fully-automated instrument designed to measure both wet and dry samples. The preparation of the sample included making a dilute suspension of the powders that were dispersed in water, and then ultrasonicated for a few minutes to break any agglomerates.

Fig. 4.2 displays the results obtained for the powders showing the relative and cumulative volume distributions. The average size (median or D_{50}) of the Al_2O_3 particles was measured as 0.734 μm, while D_{90} was less than 2 μm. These results agree well with the data provided by the producer (Table 3.1).

The results for the copper and tungsten powders are also shown in Fig. 4.2. The copper powder has a size distribution with a median particle size of approx. 17 μm, and D_{90} around 35 μm. The suspension of the tungsten powder in distilled water produced some artifact peaks, due to the very high density of W, which was overcome by measuring a dilute W/Al_2O_3 slurry. The results showed an average particle size of 0.7 μm.

The size distribution was non-symmetric for all three powders, with different mode and median values, all of which are listed in Table 4.2. In total, the calculated values are in good agreement with the data provided by the producer of each raw material.

Table 4.1: Data obtained from the AMCSD to index the peaks of the XRD patterns (scanning angle up to 80°): Diffraction angle (2θ), lattice spacing (D), and Miller indices (HKL).

	2-θ [°]	**D-spacing [**nm**]**	**H K L**
Corundum, α-Al_2O_3			
	25.59	0.348	0 1 2
	35.17	0.255	1 0 4
	37.80	0.238	1 1 0
	43.38	0.209	1 1 3
	46.21	0.196	2 0 2
	52.58	0.174	0 2 4
	57.54	0.160	1 1 6
	59.78	0.155	2 1 1
	61.17	0.152	1 2 2
	61.35	0.151	0 1 8
	66.56	0.140	2 1 4
	68.25	0.137	3 0 0
	70.46	0.134	1 2 5
	74.36	0.128	2 0 8
	76.94	0.124	1 0 10
	77.30	0.123	1 1 9
Copper, Cu			
	43.35	0.209	1 1 1
	50.49	0.181	2 0 0
	74.20	0.128	2 2 0
Tungsten, W			
	40.30	0.224	1 1 0
	58.31	0.158	2 0 0
	73.26	0.129	2 1 1

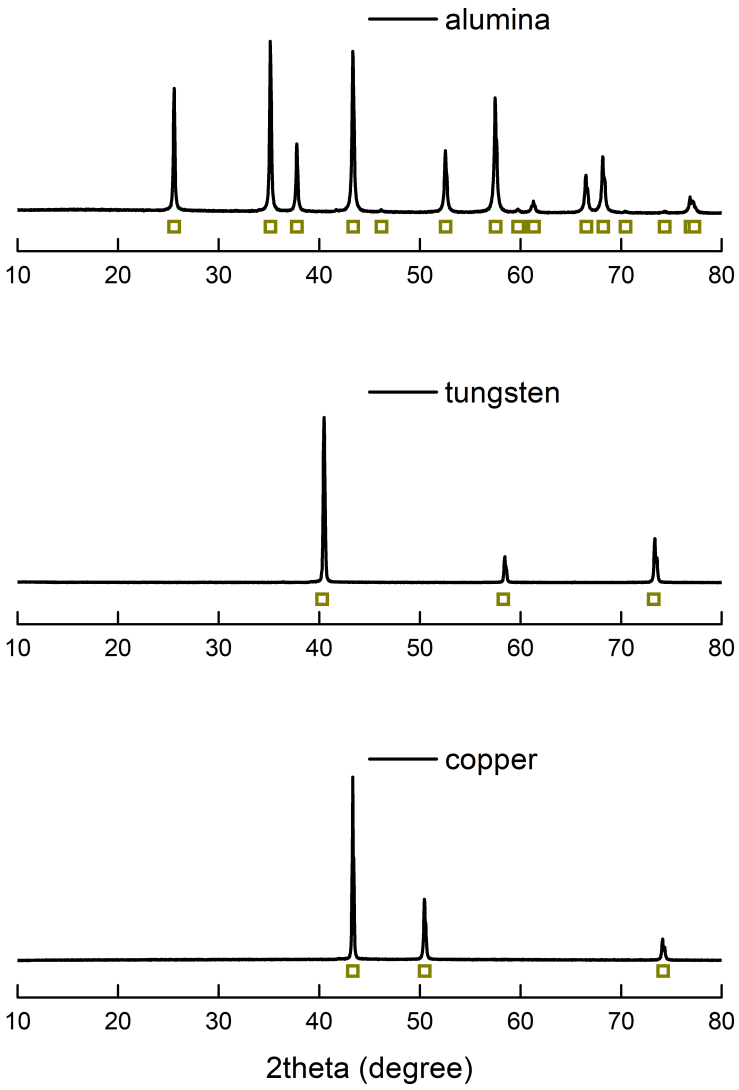

Figure 4.1: XRD patterns of the powders: alumina, tungsten, and copper.

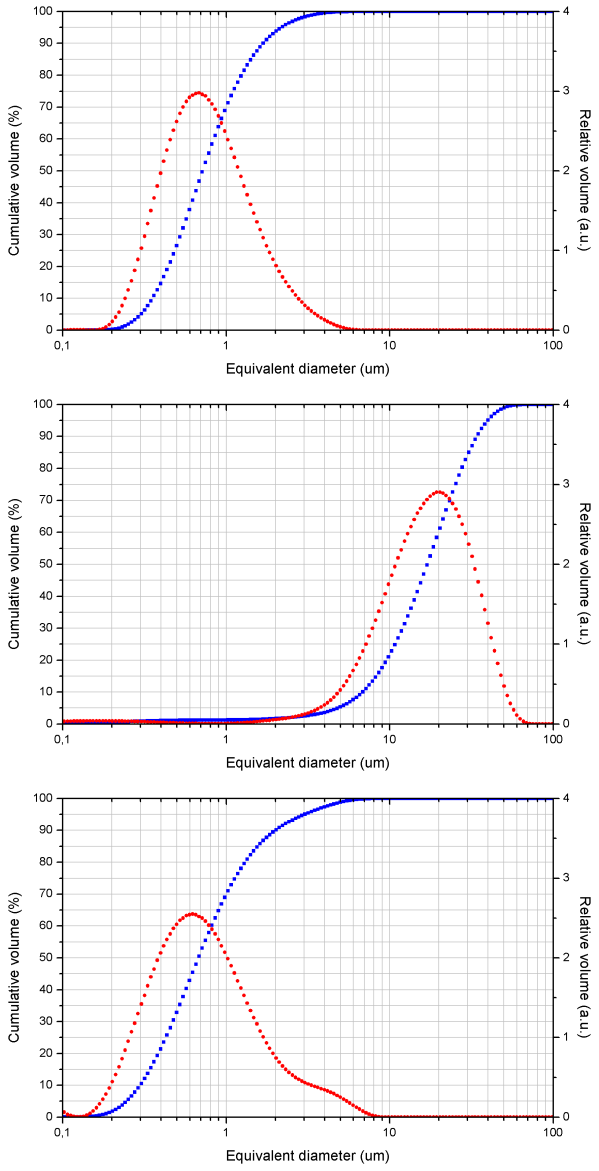

Figure 4.2: Particle size distributions for: alumina powder, copper powder, tungsten/alumina slurry.

Table 4.2: Characteristic sizes obtained via laser diffraction analysis of the starting materials.

Characteristic sizes	**Al_2O_3 powder**	**Cu powder**	**W/Al_2O_3 slurry**
Median (μm)	0.734	17.376	0.692
D_{10} (μm)	0.362	6.964	0.304
D_{50} (μm)	0.734	17.376	0.692
D_{90} (μm)	1.720	34.850	2.040
Span	1.853	1.605	2.508

4.3.2 Optical microscopy

The optical microscopy examination was conducted to gain information regarding the morphology of the metal powders in terms of particle shape, rather than particle size, since the size distribution was already determined via laser diffraction analysis and the results were in agreement with the producers data.

A minimum amount of each metallic powder was mixed with distilled water to form an agitated suspension, a drop of which was placed on a microscopy slide to facilitate the wet mounting method. A total of 30 images were captured for each metal powder with the use of an optical microscope (Nikon Eclipse E400 POL). An image processing and analysis program with a freely available source code was used to convert the captured optical micrographs into images that can be processed.

Some representative optical micrographs of the copper and the tungsten powders are provided in Fig. 4.3. The distribution of sizes of the copper particles can be observed, while it is also clear that the particles are roughly spherical according to the ISO classification for common shapes. As for the tungsten powder, agglomerated regions can be discerned, while the shape of the particles is rather irregular.

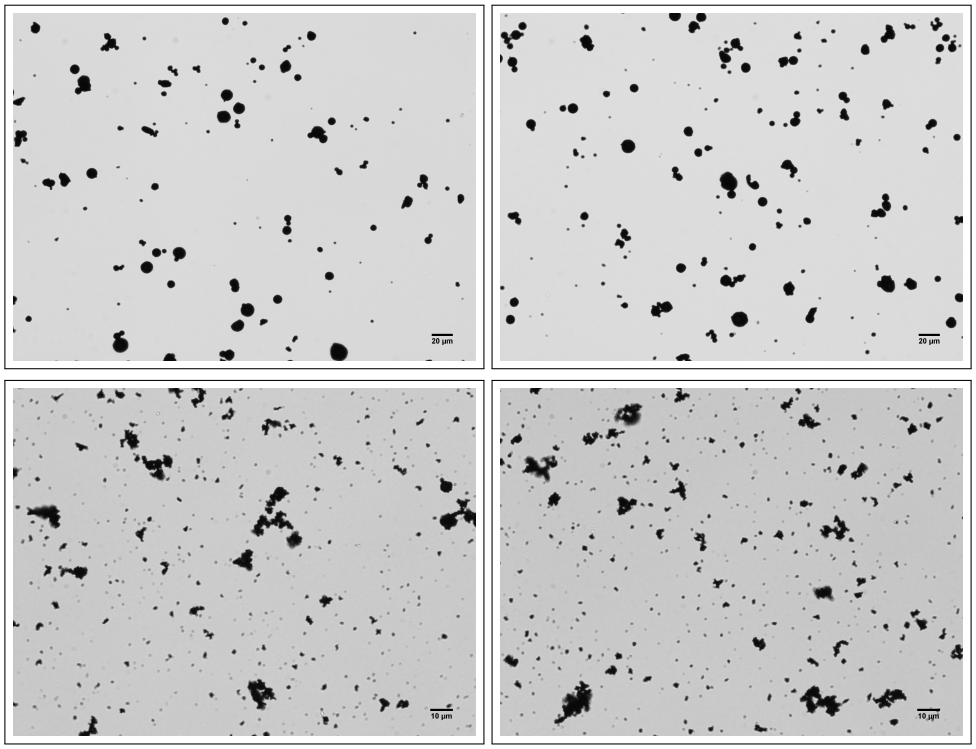

Figure 4.3: Optical microscope images of the metallic powders: copper (top) and tungsten (bottom).

4.4 Summary

The X-ray diffraction analysis of the as-received powders confirmed the purity of each material, and did not detect any additional peaks other than the characteristic ones for each phase. Their crystal structure was also verified by comparing and indexing every peak with relevant database values. The laser diffraction analysis that was performed to determine the size and size distribution of the raw powders showed a fine size for both alumina and tungsten powders with a median size below 1 μm, and a more coarse copper powder with bigger particles and sizes that ranged from a few up to several μm. The optical microscopy examination of the slides provided information regarding the shape of the powder particles: copper is nearly spherical with isolated particles, whilst tungsten is irregular with agglomerated regions.

5 Structure of the Composites

5.1 Introduction

This chapter presents the observations that have been made and the results that have been obtained concerning the characterization of the green and sintered samples including pure Al_2O_3, copper–Al_2O_3, tungsten-Al_2O_3, and tungsten-copper-Al_2O_3 composite materials. The phase composition, the green and sintered density, the open porosity, and the linear shrinkage of the composite samples are evaluated. The dispersion of metal particles throughout the Al_2O_3 matrix, as well as the particles' characteristics are also examined. The results are discussed and are correlated in terms of processing/microstructure.

5.2 Macroscopic examination

A significant physical characteristic of ceramic bodies relates to their aesthetic quality after fabrication and sintering, i.e. the formation and presence of any surface flaws or imperfections, such as cracks or blisters. Besides the sintering cycle, the pre-sinter thermal cycle performed for the binder burnout process is usually another step during which defects are formed on the surface of the samples, and these defects have the potential to affect the overall properties of the parts including their mechanical response.

The external characteristics of the specimens can be detected via visual inspection. The green parts were initially examined, and were found to have a good overall appearance and a satisfactory green strength that allowed handling of the samples without any concern such as possible disintegration or fracture.

It is important to note that the samples have preserved their original cylindrical shape after sintering, without any indication of distortion, which is not unusual for samples of such geometry. A core-skin macrostructure was discerned for the Cu-Al_2O_3 samples with a distinct color variation; a red

Figure 5.1: Images showing some specimens after sintering: (a) pure Al_2O_3, (b) core-skin macro-structure for Cu-Al_2O_3, (c) W-Al_2O_3.

copper-core and a white alumina-surface. A homogeneous macro-structure was observed for the W-Al_2O_3 samples, and some color differences among the different compositions depending on the content of tungsten. Similarly, there were not any surface flaws observed macroscopically for the three-phase W-Cu-Al_2O_3 composites, with only exception some specimens with a high total metal loading (20Cu-2W composite type) which developed surface cracks. Fig. 5.1 is a macro-photograph of the sintered cylindrical specimens reflecting the above observations.

5.3 X-ray diffraction analysis

The X-ray diffraction analysis has been performed for both the green and sintered parts to clarify the formation and/or presence of any additional phases, such as metal oxides. Despite the aqueous processing route that has been followed, there were not any oxides formed in the green samples. Similarly, only pure phases of Cu, W, and Al_2O_3 were detected in the patterns of the sintered parts. Fig. 5.2 portrays the XRD patterns of the Cu-Al_2O_3, W-Al_2O_3, and W-Cu-Al_2O_3 composites. All corresponding peaks that can be discerned in the patterns have been indexed according to the AMCSD. The dots that appear on the graphs correspond to the characteristic peaks of the copper and the tungsten metallic phases (Table 4.1).

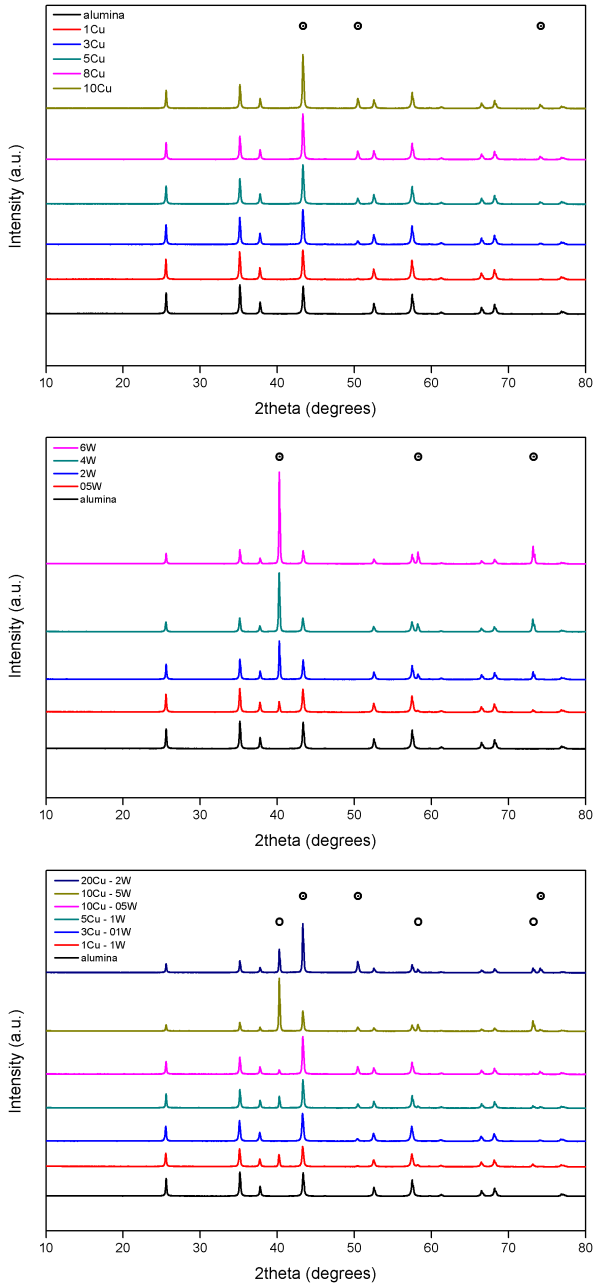

Figure 5.2: X-Ray diffraction patterns of green and sintered samples for alumina matrix reinforced with Cu, W, and W-Cu particles. Note the increased intensity of the characteristic peaks for higher contents of metallic phase.

5.4 Residual Carbon Content

The CHNS elemental analysis was performed on selected Al_2O_3 and metal-Al_2O_3 samples after the completion of the binder burn-out process (pre-sinter thermal cycle) in order to determine the presence of any residual carbon content. The quantitative method did not detect any amount of carbon (any amount would be below the detection limit of the instrument) and this enabled the continuation of the fabrication process with the sintering cycle.

5.5 Density and Shrinkage

5.5.1 Relative Green and Sintered Density

The density of all green and sintered samples was determined using the dimensions and the mass of the cylindrical specimens, given their geometric shape which enabled the mass/volume measurement. The mass was recorded with a high precision balance and the dimensions (length and diameter) were measured at different locations across each sample to assure a good average value. Archimedes' volume displacement method was utilized to estimate the density of the sintered parts, as the green bodies would disintegrate in water. The values are listed consecutively in Table 5.1 for the Al_2O_3-matrix composite samples reinforced with Cu, W, and W/Cu particles.

Green bodies | Alumina samples

The relative green density that has been attained for the pure alumina specimens is reasonably high and reaches approx. 60%. This value agrees with the results that have been reported from similar studies. A relative green density of 61% has been reported for slip-casting a 0.2 μm Al_2O_3 powder (Pabst et al., 2012) and a value of 62% has been attained for slip-casting a 0.35 μm Al_2O_3 powder with 50 vol.% solids content (Sánchez-Herencia, Hernández, and Moreno, 2006). Therefore, the value is rather satisfactory given that the alumina powder employed in this work had a median particle size of 0.7 um, and the solids content were lower.

Green bodies | Metal-Alumina samples

It can be observed from the data provided in Table 5.1 that the green density of the pure Al_2O_3 samples is higher than most of the metal-alumina composite samples. The relative densities of the green parts varied around 53-56% for copper-alumina, 55-60% for tungsten-alumina, and 57-63% for tungsten-copper-alumina composite samples.

Table 5.1: Relative green density via mass/volume measurements, and sintered density via the Archimedes immersion technique and mass/volume measurements.

Composite type	**Relative green density (%)**	**Relative sintered density (%) - A**	**Relative sintered density (%) - m/v**
Al_2O_3	59.7 ± 1.9	97.4 ± 0.1	97.7 ± 1.6
1Cu	54.0 ± 0.6	96.4 ± 1.9	95.9 ± 1.0
3Cu	53.5 ± 1.2	94.9 ± 0.5	94.6 ± 0.7
5Cu	53.6 ± 1.4	94.6 ± 0.3	94.0 ± 1.2
8Cu	55.3 ± 0.8	93.8 ± 0.2	93.8 ± 0.6
10Cu	54.7 ± 1.1	91.1 ± 0.4	91.4 ± 0.7
05W	59.8 ± 0.8	97.4 ± 1.8	97.7 ± 1.7
2W	56.8 ± 2.1	96.5 ± 1.6	95.8 ± 1.6
4W	56.2 ± 3.4	95.1 ± 1.0	94.2 ± 1.9
6W	55.0 ± 1.3	92.5 ± 0.7	93.2 ± 1.3
1Cu - 1W	58.1 ± 0.9	94.4 ± 0.9	95.4 ± 0.8
3Cu - 01W	59.1 ± 0.7	95.9 ± 0.7	96.1 ± 0.9
5Cu - 1W	58.3 ± 0.8	93.3 ± 0.3	94.0 ± 0.8
10Cu - 05W	61.7 ± 1.2	91.3 ± 1.5	90.2 ± 1.5
10Cu - 5W	57.7 ± 0.4	91.3 ± 1.0	90.0 ± 0.2
20Cu - 2W	63.3 ± 0.5	83.3 ± 2.0	80.3 ± 1.3

The W-alumina slurries resulted in higher green densities in comparison to those of Cu-Al_2O_3 slurries. This may be related to the initial powder characteristics, i.e. the size of powder particles. The Cu powder had an average particle size of 17 μm, whereas the W powder had an average size of less than 1 μm. It should also be noted that the highest green density was obtained for the lowest metal loading; that of 0.5 vol.% W-Al_2O_3 composite, and the value was approx. 60%, i.e. same value as that of pure alumina. It can also be observed from the data, that high green densities were achieved for the W-Cu-Al_2O_3 samples with relative densities above 57% for all compositions despite the high metal loading. This should be related to the presence of powders with dissimilar sizes which have presumably favored the packing density (Fig. 2.25).

The relative green densities of metal-alumina composite samples are seldom reported in the relevant studies. Green compacts with a relative density of 55% were reported for nickel-alumina after cold isostatic pressing in the study of Tuan and Brook, 1990, and relative densities of approx. 60% have been cited in the work of Tuan, Chen, and Yang, 2007 for nickel-alumina samples with nano-sized nickel particles of low content (< 0.25 vol.%). Therefore, the results of this work are in accordance with literature data and similar studies on metal/Al_2O_3 samples with reported values in the range of 55-60%. This validates the suitability of the aqueous slip-casting technique for the synthesis of metal-dispersed alumina-matrix composites. Optimization of the process is certainly welcome, however even if the green densities are reasonably high, this does not necessarily guarantee near theoretical densities after firing, as an amount of porosity still exists in the green compact.

Sintered bodies | Alumina samples

The sintering cycle was maintained the same for all fabricated samples, including the pure alumina specimens. The processing steps were intentionally performed under identical conditions, to facilitate the scope of the study and compare structures that have emerged by following identical routes.

The sintering temperature (T_s = 1500 °C) was chosen based on a number of parameters. At first, the producer's information suggested that sintering the Al_2O_3 powder for 1 h at 1540 °C would result in a compact with 98% RD (Table 3.1). Further, it was the low melting point of copper (T_m = 1084 °C), in contrast to the extremely high melting point of tungsten (T_m = 3414 °C), that had to be taken into consideration. This factor did pose some limitation in terms of sintering, given that the higher the sintering temperature the more risk to lose a fraction of the copper content. Nonetheless, the processing characteristics, as have been discussed in previous sections, require fine adjustment

in order to satisfy a number of requirements; i.e. high sintering temperatures are required to obtain near-theoretical densities due to the activation of mechanisms that promote densification of the green parts, while these high temperatures are time-consuming and might also result in particle size enlargement which is not beneficial. In conclusion, the sintering temperature of 1500 °C was considered the lowest required temperature for the successful densification of the Al_2O_3 matrix, and at the same time it was not that high to cause for concern regarding copper that was used as a second-phase inclusion in most of the fabricated compositions.

The sintered density of alumina was measured to be 3.88 - 3.90 g cm^{-3} via the immersion technique and the mass/volume calculations. The values adequately compare to the theoretical value of 3.987 g cm^{-3} that can be found in the scientific literature for α-alumina (corundum). Taking into consideration the followed processing route and the absence of any applied pressure during the sintering cycle, the results are consistent with published data that have been derived from similar studies.

A fired density of 3.88 g cm^{-3} has been cited in the work of Ji and Yeomans, 2002a obtained after pressureless sintering at 1500 °C for 1 h and heating rate of 5 °C/ min, while pressureless sintering under vacuum at 1700 °C for 1.5 h has resulted in values of 3.89 g cm^{-3} for pure Al_2O_3 compacts in the study of Konopka and Oziebo, 2001. The same value (3.88 g cm^{-3}) has also been cited for hot-pressed Al_2O_3 samples at 1400 °C for 30 min (Guichard, Tillement, and Mocellin, 1998), while relative densities just below 98% have also been obtained in the studies of Tuan and Brook, 1990 and Chou and Tuan, 1995 for alumina samples prepared via cold-pressing and pressureless sintering at 1600 °C.

Sintered bodies | Metal-Alumina samples

The relative densities of the samples in the green state and after sintering are shown in Fig. 5.3 as a function of the metal volume fraction for copper, tungsten, and tungsten/copper reinforcement.

Copper-Alumina

The relative densities of the copper-alumina samples are shown in Fig. 5.3a. The sintered density decreases with an increase in copper content and this is related to the poor wetting of liquid copper on alumina. The contact angle between the liquid Cu and the Al_2O_3 substrate is 144° at the temperature of 1097 °C (just above the melting point of copper), and 116° at T = 1447 °C (just below the sintering temperature) (Nikolopoulos and Agathopoulos, 1992).

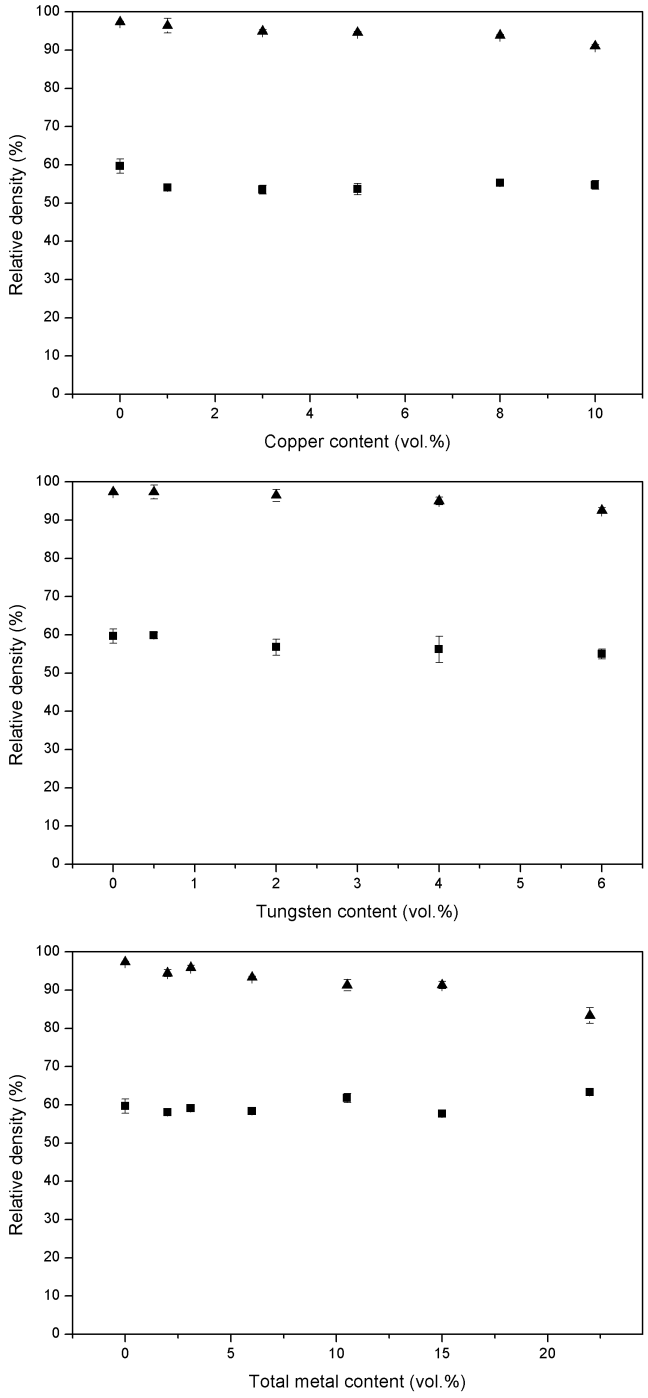

Figure 5.3: Relative green and sintered density of the (a) Cu-Al_2O_3, (b) W-Al_2O_3, (c) W-Cu-Al_2O_3 composites.

Therefore the contact angle remains > 90° for the entire sintering schedule (Table 2.4) and this hinders the densification of the samples.

Further, the effect of the differences in CTE between the two phases can not be ruled out: copper has a higher thermal expansion coefficient than that of alumina, and this translates to copper particles that will contract more than the matrix material during cooling from the sintering temperature. This might result in some residual porosity around the inclusions. Nickel-alumina is another metal/ceramic system with $a_f > a_m$. The volume shrinkage of the nickel particles is larger than that of the alumina matrix during cooling and this results in the formation of pores and void spaces at the interface where the particles are located (Li, Huang, and Guo, 2003; Lu et al., 2000).

In total, the sintered densities of the Cu-Al_2O_3 samples are reasonably high given the pressureless sintering that has been preformed in this study. Lower values have been attained in the work of Aldrich and Edirisinghe, 1998 for the same Al_2O_3 matrix material and a much finer (2 μm) copper powder: a relative density of 97.9% was obtained for pure Al_2O_3 at 1700 °C, and 91.2% for 5 vol.% Cu, in contrast to the value of 97.4% obtained for the same samples prepared via hot-pressing.

Tungsten-Alumina

Fig. 5.3b portrays the relative densities for the W-Al_2O_3 composite samples. It can be seen that the sintered relative density decreased with increasing tungsten volume fraction. However, the highest attained value was that for the 0.5 vol.% W content, with the same sintered density value as for pure alumina, which was anticipated based on similar observations for the density of the green parts (Table 5.1). This suggests that high densities can be achieved for low contents of second-phase inclusions.

In terms of expansion coefficients, in the case of the W-Al_2O_3 samples, tungsten has a lower CTE than pure alumina, which means that the matrix exerts a force on the particles during cooling. This might have contributed to the increased density values (> 95%) that have been achieved for most compositions. Similar metal/ceramic systems with af < am include Mo/alumina (Nawa, Sekino, and Niihara, 1994), and Cr/alumina composites (Ji and Yeomans, 2002a).

In contrast to the copper-Al_2O_3 composites, there are no relevant literature data (to the best of the author's knowledge) for the preparation of W-Al_2O_3 samples via pressureless sintering. Density results have been reported for tungsten-reinforced alumina-matrix composites prepared only via hot-pressing (Sekino and Niihara, 1995; Sekino and Niihara, 1997) or spark

plasma sintering (Rodriguez-Suarez et al., 2009) which usually result in near-theoretical densities.

Tungsten-Copper-Alumina

The relative densities of the W/Cu/Al_2O_3 composites are depicted in Fig. 5.3c as a function of the total metal content. Despite the enhanced density values of the green parts, some compositions exhibited a relatively low density after firing. This is clearly attributed to the presence of the three phases and the fact that W and Cu are completely immiscible (Kim and Moon, 1998; Johnson, Brezovsky, and German, 2005), and termed as non-interacting (German, 2014). The negligible solubility of W in molten Cu (Shabalin, 2014), in addition to the low affinity of each metal for alumina, have hindered the densification of the parts.

Further, the major mismatch in thermal expansion coefficient between the three constituent phases has caused the formation of cracks that were visible macroscopically for compositions with a high metal loading. This also accounts for the poor densification of the 20Cu-2W composite type (Table 5.1), and explains the minor variation of the sintered values obtained via the mass/volume calculations and immersion technique; the cracks that have been formed on the body have contributed to a higher calculated volume and, therefore, a lower calculated mass/volume density.

5.5.2 Open Porosity and Linear Shrinkage

The open porosity of the sintered bodies was determined via the immersion technique (Eq. 3.3), while the linear shrinkage was calculated by comparing the length of the cylindrical specimens before and after sintering (Eq. 3.4). These characteristics are listed in Table 5.2 for all compositions.

Copper-Alumina Fig. 5.4a depicts the variation of open porosity with metal volume fraction for the copper-reinforced Al_2O_3-matrix composites. It is evident from this graph that the values increase with increasing copper content. Low values (max. around 1%) have been calculated for copper content up to 8 vol.%, whereas a relatively high value was noted for the samples with the highest copper loading, that of 10 vol.% (Table 5.2).

Tungsten-Alumina The open porosity of the samples is shown in Fig. 5.4b as a function of tungsten content. The samples had almost no open porosity and all values remained below 0.5%. The amount of tungsten in each composition had no effect on this microstructural characteristic.

Table 5.2: Open porosity of the sintered samples, and linear shrinkage after sintering.

Composite type	**Open porosity (%)**	**Linear shrinkage (%)**
Al_2O_3	0.41	13.8 ± 0.3
1Cu	0.53	15.8 ± 0.1
3Cu	0.77	16.3 ± 0.2
5Cu	1.19	15.9 ± 0.2
8Cu	1.44	15.8 ± 0.3
10Cu	3.91	15.3 ± 0.3
05W	0.35	15.1 ± 0.3
2W	0.31	14.7 ± 0.2
4W	0.28	15.5 ± 0.3
6W	0.46	15.5 ± 0.2
1Cu - 1W	0.43	15.1 ± 0.2
3Cu - 01W	0.44	14.9 ± 0.2
5Cu - 1W	1.09	14.6 ± 0.2
10Cu - 05W	4.48	12.7 ± 0.3
10Cu - 5W	5.44	14.4 ± 0.1
20Cu - 2W	12.27	10.1 ± 0.2

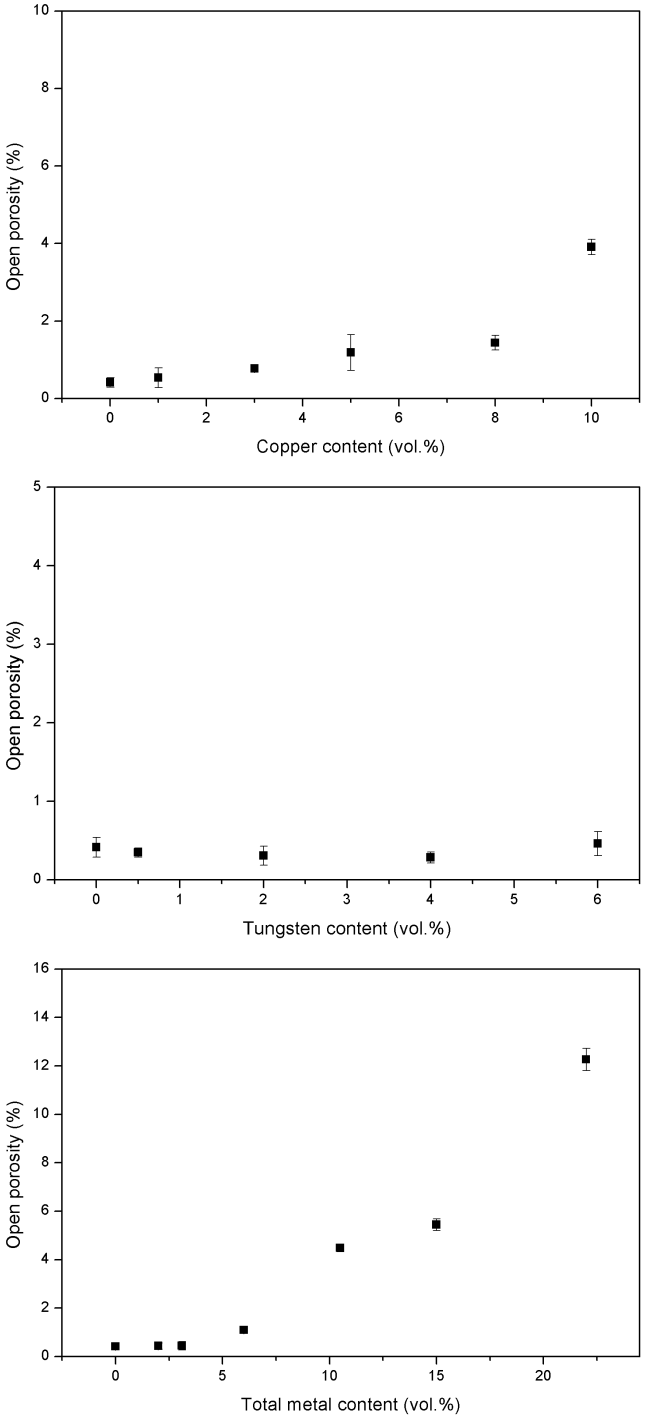

Figure 5.4: Open porosity of the (a) Cu-Al_2O_3, (b) W-Al_2O_3, (c) W-Cu-Al_2O_3 composites.

Tungsten-Copper-Alumina Fig. 5.4c shows the results for the W-Cu-Al_2O_3 samples as a function of the total metal content. It can be observed that the values increase with the further addition of metallic particles. The open porosity remains low (maximally around 1%) up to total metal contents of 6 vol.% (composite type 5Cu-1W), but increases up to around 4-5% for contents above 10 vol.%. Further, the open porosity of the 20Cu-2W composite type is rather high, but corresponds to samples with macroscopic defects and extensive surface cracks.

The calculated open porosity values of most of the metal-alumina composites have remained close to the value of pure alumina, while higher amounts have been recorded only for copper contents $\geq$ 10 vol.%. Further discussion will take place in the following sections.

The linear shrinkage of the parts after sintering is another important characteristic of ceramic-based materials. The lowest value was calculated for the pure Al_2O_3 samples (approx. 14%), while most of the metal-alumina samples exhibited slightly higher values. The linear shrinkage of the copper-alumina samples varied around 15-16%, for the tungsten-alumina samples the values varied around 15%, while the shrinkage of the W-Cu-Al_2O_3 samples was around 14-15%, see Fig. 5.5.

5.5.3 Comparison and Discussion

It has been shown in the earlier sections that the green density of ceramic materials is a valuable parameter which provides important information for the sintered composites. Usually some correlation between the green and the sintered density of the parts can be noticed, i.e. the higher the green density, the less the pore volume that has to be eliminated during sintering (Barsoum and Barsoum, 2002). This implies that a high green density is usually accompanied by a low shrinkage due to the reduced pore volume. Fig. 5.6 depicts the linear shrinkage vs the relative green density of all compositions, and comes to verify this assumption. Indeed the higher the relative density of the green parts, the lower the linear shrinkage.

Further, the fired density might also be affected by the green density; i.e. the former is often observed to decrease with decreasing green density, but this usually applies for green densities below 55-60% (Somiya et al., 2003). Thus, the relative green densities of the pure Al_2O_3 samples and metal-Al_2O_3 composites samples achieved in this study were within acceptable limits, and high enough to yield good sintered densities.

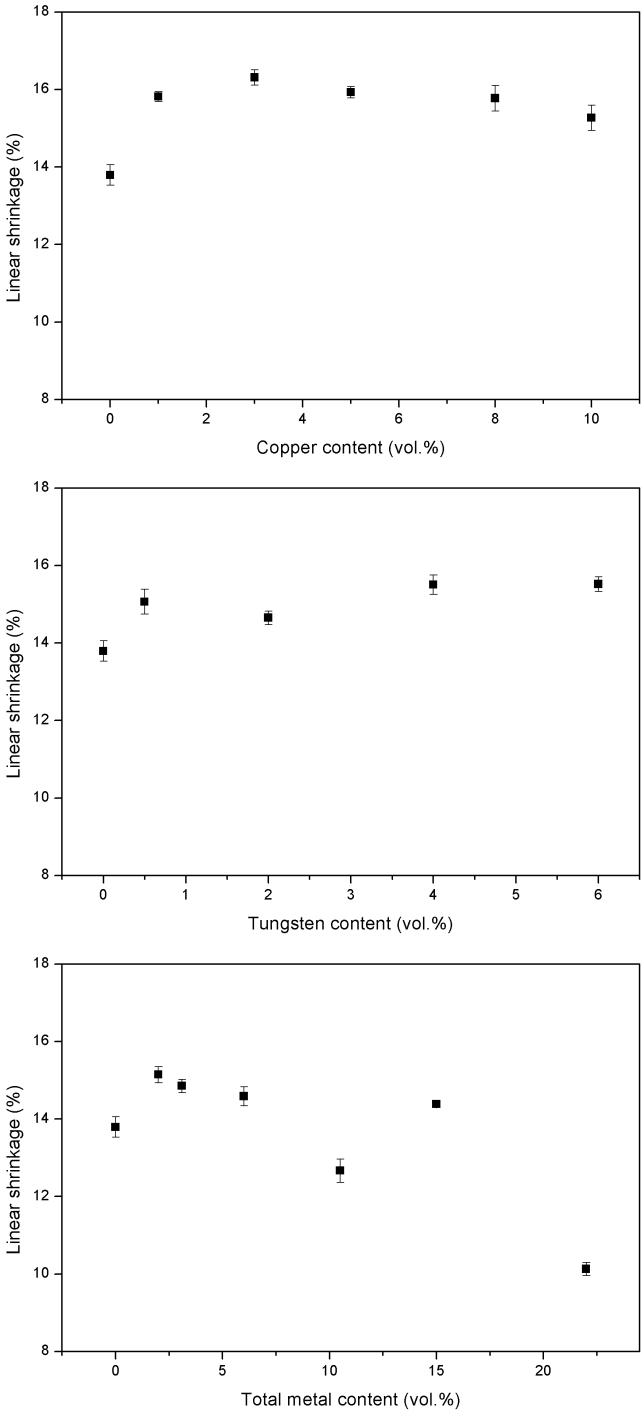

Figure 5.5: Linear shrinkage of the composites.

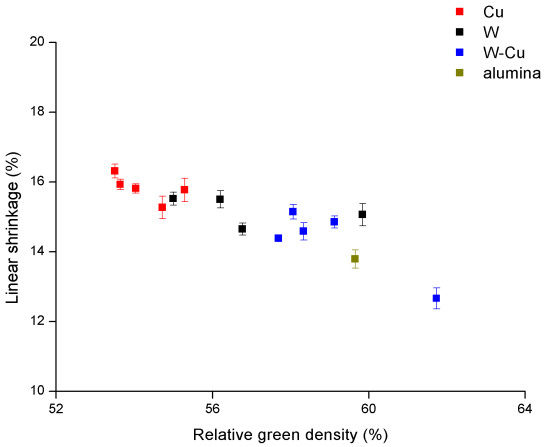

Figure 5.6: Linear shrinkage vs green density for all samples.

W-Cu-Al_2O_3 samples

The fabrication of the various W-Cu-Al_2O_3 compositions enables the comparison between these and the Cu-Al_2O_3 and/or W-Al_2O_3 compositions in terms of various parameters including the following:

Relative density: Fig. 5.7 depicts the relative green and sintered density of the Cu-Al_2O_3 and the W-Cu-Al_2O_3 samples, as a function of either copper or tungsten content. It can be seen (first graph) that the addition of small amounts of tungsten powder in the aqueous copper-alumina slurry increased the green relative density. Unfavorably, this did not apply for the sintered density as well, presumably due to the considerable CTE differences Additionally, it can be deduced (second graph) that the addition of copper did not alter the green density, while it may have lowered the sintered density of the parts.

Open porosity: Fig. 5.8 is a comparison between the different compositions in terms of open porosity. The first graph shows the open porosity values of the Cu-Al_2O_3 and W-Cu-Al_2O_3 samples as a function of copper content, while the second graph shows the values of the W-Al_2O_3 and W-Cu-Al_2O_3 samples as a function of tungsten content. It can be deduced that it is the presence of copper that has an effect on the open porosity values, possibly related to some diffusion and evaporation of Cu particles from the surface of the specimens due to the sintering above its melting point. The first graph shows similar values of open porosity for the same content of copper regardless the addition of some W, whereas the second graph shows large differences mostly for the samples containing tungsten content of 0.5 vol.% and 5 vol.%, which

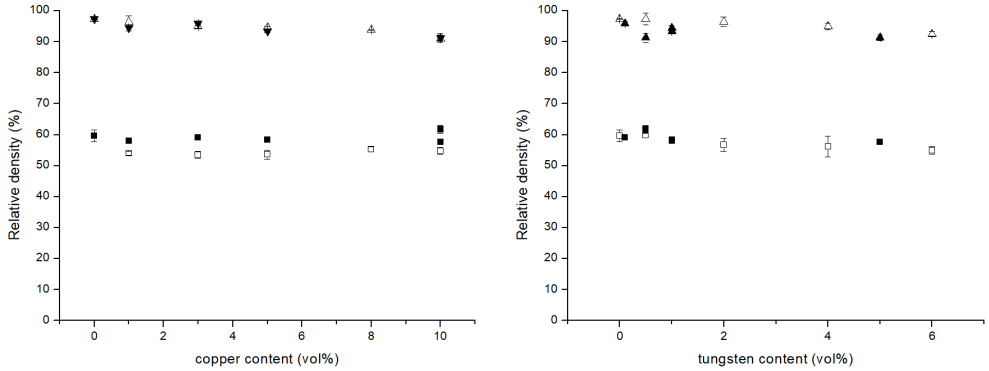

Figure 5.7: Relative green (squares) and sintered (triangles) density of Cu-Al_2O_3 and W-Al_2O_3 (open symbols) in comparison to W-Cu-Al_2O_3 (solid symbols) as a function of copper and tungsten content.

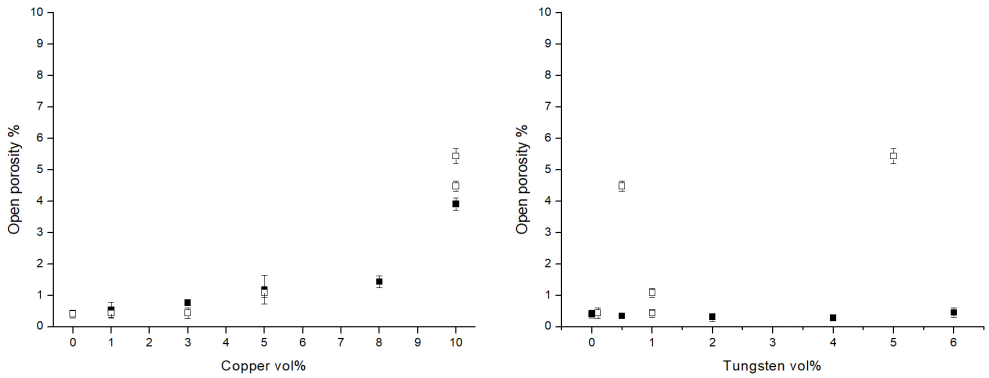

Figure 5.8: Open porosity of sintered W-Al_2O_3 and Cu-Al_2O_3 (solid squares) in comparison to open porosity of sintered W-Cu-Al_2O_3 (open squares) as a function of copper and tungsten content.

correspond to an addition of 10 vol.% copper.

Weight loss: Fig. 5.9 portrays the weight loss of the specimens recorded after sintering; the data have been normalized to exclude the weight loss due to the organic additive and any residual water or vapor. It can be seen from the first graph that the tungsten content has no effect on the weight loss, and that similar values are recorded for the same amounts of copper content. Further, the second graph suggests that the W-Al_2O_3 samples exhibited zero weight loss and that any differences are solely attributed to the presence of copper. For instance, the weight loss of approx. 1-2% for 0.5 vol.% and 5 vol.% tungsten corresponds to composites with copper content of 10 vol.% in both cases. However, the weight loss in total is only minimal: it remains around 0.5% for most of

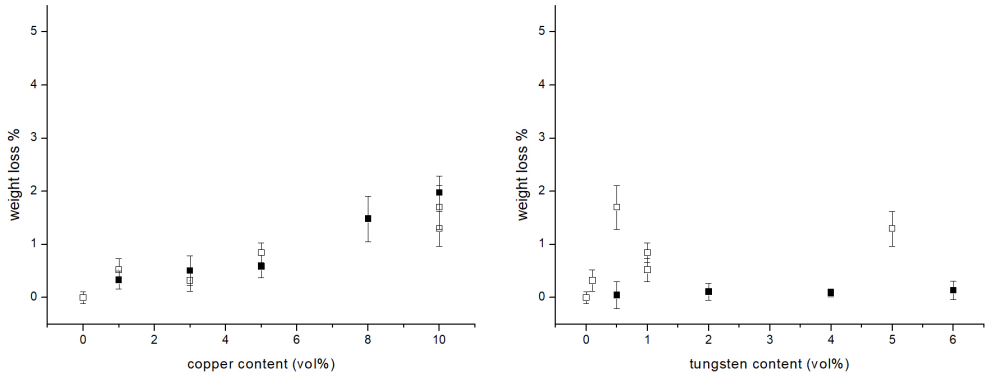

Figure 5.9: Weight loss after sintering for W-Al_2O_3 and Cu-Al_2O_3 (solid squares) in comparison to weight loss after sintering for W-Cu-Al_2O_3 (open squares) as a function of copper and tungsten content.

the Cu-Al_2O_3 compositions, and is only higher for the highest copper loading, but still maintains below 2%.

5.6 Spatial distribution of particles

The examination of the polished sections was performed to evaluate the degree of distribution of second-phase particles in the matrix, i.e. if a homogeneous dispersion of the metallic inclusions throughout the Al_2O_3 material has been achieved. In addition, the analysis of the optical micrographs facilitates the evaluation of the morphology of the particles; their shape, size and/or size distribution, as well as the identification of any fluctuations in view of the metal volume fraction increase.

A microstructural characteristic exhibited by the copper-alumina samples was the core-skin structure that was initially discerned via the macroscopic observations of the sintered samples (Fig. 5.1). The skin had virtually zero copper content and its thickness varied slightly with composition, while it remained below 100 μm for all samples (95 μm for 1Cu, around 80 μm for 3Cu & 5Cu, and around 70 μm for 8Cu & 10Cu). A representative image captured with the use of an optical microscope is provided in Fig. 5.10c.

A similar core-skin structure has been reported for Ag/alumina composites, however it was solely attributed to the sintering above the melting point of silver and the increased weight loss of the metallic phase due to evaporation (see section 2.5.1). In this study though, the copper-free skin of the cylindrical samples can be, only partially, attributed to copper evaporation during the sintering process. Given the minimal weight loss after sintering it can be argued that the core-skin structure might have been formed in the green parts

while water was being absorbed by the PoP moulds during the slip-casting process. It seems, thus, that the escaping liquid water might have dragged some particles with it. Given the smaller and lighter alumina particles over the larger and heavier copper particles, it is possible that the former were carried away faster than the latter.

The copper-alumina samples exhibited a homogeneous distribution of copper particles (in the core), while the increase in copper volume fraction did not result in an increase in particle size. Likewise the Cu powder, the copper particles remained near-spherical after sintering and exhibited a size distribution with average particle size of approx. 12 μm ± 9 μm for all compositions (see Fig. 5.10b and Appendix B for the number-weighted distribution derived via the image analysis of the optical micrographs).

A homogeneous dispersion of tungsten particles in the Al_2O_3 matrix has been achieved in all prepared W-Al_2O_3 composites. It is interesting to note that for the lowest content of 0.5 vol.%, the tungsten particles were faintly visible via the optical microscope, while the samples with a higher loading exhibited an increase in particle size. This is attributed to the characteristics of the raw tungsten powder in terms of agglomeration. Unlike the copper particles, tungsten was not spherical but rather irregular in shape, see Fig. 5.10d. The average size of the particles varied around 30-35 μm for the short diameter and around 50-55 μm for the long diameter.

The analysis of the micrographs of the three phase composite samples suggest that both metal particles were evenly distributed in the alumina matrix. Fig. 5.10e portrays the 10Cu-05W composite type with a copper-rich surface and Fig. 5.10f shows the 20Cu-2W composite type in which several cracks can be discerned.

5.7 Discussion

A series of different metal-reinforced alumina-matrix composites have been successfully fabricated using the aqueous slip casting technique followed by pressureless sintering in a reducing hydrogen atmosphere.

Compositions

The total metal loading of the composites was chosen with primary scope not to increase significantly the density of the samples in comparison to the density of the pure Al_2O_3 matrix material. The theoretical values for the maximum densities are around 4.5 g cm^{-3} for Cu-alumina, less than 5.0 g cm^{-3}

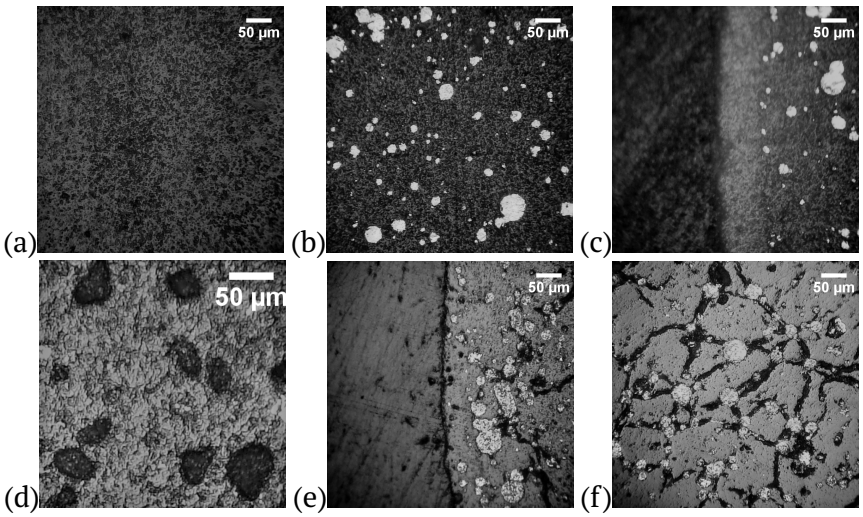

Figure 5.10: Selected optical micrographs of the microstructure of the samples: (a) pure alumina matrix, (b) dispersed spherical copper particles in the alumina matrix, (c) alumina-rich surface and copper-rich core in Cu-Al_2O_3 samples, (d) dispersed tungsten particles in the alumina matrix, (e) copper-rich surface for the 10Cu-05W composite type, (f) spherical copper particles and cracks that spread throughout the bulk of the alumina matrix for the 20Cu-2W composite type.

for W-alumina, and below $5.0\,\mathrm{g\,cm^{-3}}$ for most of the W-Cu-alumina compositions.

Processing Route

A series of different metal/alumina composites were prepared and characterized towards their green and sintered density, open porosity and linear shrinkage, as well as in terms of particle dispersion and distribution throughout the matrix. The results suggest that the aqueous slip-casting technique is a suitable processing route for the synthesis of composite samples consisting of an alumina matrix and metallic copper and tungsten as second-phase inclusions.

After a thorough literature survey it can be argued that this particular processing method is seldom used/reported for the synthesis of metal-ceramic composites. Its advantages, though, render it an interesting route and these include: the minimum amount of organic additives that are required over other liquid or semi-liquid methods, the use of water as a suspension medium which renders slip-casting non-hazardous, the ability to form parts with a desired shape, in addition to the better packing capacity compared to conventional dry-pressing routes which posses several drawbacks. Further, the

shaping/sintering process that has been followed in this study is more cost-efficient than the hot-pressing method that is often used for the fabrication of metal/ceramic composite materials.

The optimization of the slurries was made on the basis of: (a) water content, and (b) content of organics. Both had to be minimized to avoid residual porosity and residual carbon content and possible contamination of the samples. Although suitable, the disadvantages of slip-casting include the slow production and demand of preparation of the PoP molds. In addition, long times are required for casting and drying of the samples, as well as drying of the molds between subsequent castings. Lastly, the PoP molds can be damaged after several castings which brings about the need for preparation of new ones.

Pre-sinter and Sintering Cycle

The firing schedule was optimized based on relevant studies from the literature, the producers data for the Al_2O_3 powder, the physical characteristics of the metallic powders, and personal considerations for the most advantageous schedule. The sintered samples exhibited reasonably high densities, although they did not reach near theoretical values, as anticipated for the pressureless sintering.

The samples have maintained their geometric shape after firing, without any visible flaws such as distortion or cracks and blisters. The binder burnout cycle successfully removed all organics and allowed the continuation towards the sintering cycle. The hydrogen sintering enabled the preparation of composites consisting of pure phases, free from oxides or other additional phases that might deteriorate the mechanical behavior of the specimens. The slow heating and cooling rates assured the relief of stresses during firing and cooling.

The structure of the composites

A total of 16 different compositions were prepared to reveal any differences and facilitate the comparison among them. These include pure Al_2O_3 samples, copper-alumina composites with Cu content of 1-10 vol.%, tungsten-alumina composites with W content of 0.5-6 vol.%, and W-Cu-alumina composites with total metal content ranging from 2 vol.% up to 22 vol.%.

The copper-reinforced composites exhibited a core-skin structure with an alumina-rich surface, while the Cu particles were uniformly distributed throughout the matrix material (in the core). Further, the increase in copper

content did not result in an increase in the size of the spherical Cu particles. The tungsten-reinforced composites, on the contrary, did not exhibit a core/skin structure, while the W particles were homogeneously dispersed in the matrix material and increased in size with the further increase in volume fraction. As for the W-Cu-alumina composites, both copper and tungsten particles were evenly distributed in the alumina matrix.

The principal characteristics of the materials have been examined throughout this chapter, paving the way for the evaluation of their mechanical response that will be discussed in the following chapter.

6 Mechanical Properties

6.1 Introduction

This chapter presents the results of the mechanical testing of the sintered alumina samples and metal-alumina composite samples. The measured data correspond to the average value (and standard deviation) that was calculated for each composition. The results are discussed and compared, and are further correlated to the microstructure of each composition.

Toughness is an important mechanical property of solids that describes a material's resistance to fracture, i.e. its ability to absorb energy and deform plastically prior its fracture. Accordingly, the amount of absorbed energy, per unit volume, can be an indication of the toughness response for a given material.

In this study, the determination of the fracture energy of the Al_2O_3 samples and the metal-Al_2O_3 composite samples was realized by using an Izod impact test apparatus, commonly used for polymeric materials. The measurement involves the release of a pendulum that strikes through the specimen, and records the initial height (at which the pendulum is released) and the final height (at which the pendulum swings after striking the specimen). The height difference, multiplied by the pendulum weight, is recorded (scale indication in kg cm), and when multiplied by the gravitational force it yields the energy required to fracture a specimen. This, in turn, divided by the cross-sectional area of each cylindrical specimen, results in the impact strength expressed in $\mathrm{kJ\,m^{-2}}$.

We should note here that the specimens were cylindrical and unnotched, and therefore, the evaluation of the fracture energy and the impact strength via this testing apparatus is used as a quality control method to assess the toughness response of the reinforced samples over the pure Al_2O_3 upon the addition of the metallic inclusions. Further, the data should be used for comparison reasons, rather than as absolute values. Yet, the Izod test is rather useful for the determination of the dynamic toughness of a material

under high loading rates as it simulates an impact event, such as a bird strike, i.e. a collision between an airborne animal and an aircraft (Mouritz, 2012).

The elastic modulus was determined via the impulse excitation technique, which was performed on all fabricated samples to evaluate their elastic response. Young's modulus is a well-defined mechanical property of primary importance and is of great interest in order to assess the potential of a new composite material (Ashby, 1993). During the IET measurement, the sample was mechanically excited with the use of a small hammer, and a vibration was induced which was detected with a microphone. The software calculated the frequency and, in combination with the mass and the dimensions of the specimen, determined the elastic properties of the sample. An image of the IET measurement is displayed in Appendix C showing the vibrational signal, the fast Fourier transformation, and the calculated elastic modulus value for a particular, under-examination, metal/alumina composite specimen.

Another significant feature that characterizes ceramic materials and ceramic-composites is their high hardness; an important mechanical and engineering property that measures their resistance to indentation, i.e. their ability to withstand surface penetration via an indenter. In this study, the Vickers microhardnes of the pure Al_2O_3 samples and the metal/Al_2O_3 composite samples was evaluated under an applied load of 9.81 N (1 kg) for a loading time of 10 sec. The indent traces were observed via the optical microscope of the apparatus and the values of the mean diagonal lengths were recorded to yield the hardness in $kg\,mm^{-2}$. The hardness values were determined accordingly by multiplying the results with the gravitational force to derive results expressed in GPa.

We should note at this point that the Vickers microhardness testing method exerts a much lower load than the macrohardness method (loads up to 50 kg) and it, therefore, produces higher hardness values. However, this apparatus was ideal in this study, given the dimensions of the prepared specimens.

6.2 Results

6.2.1 Pure Alumina

The pure Al_2O_3-matrix specimens exhibited an average Young's modulus of 374 GPa, which is in excellent agreement with relevant literature data. The modulus values that can be found in similar studies for Al_2O_3 samples are 373 GPa for hot-pressed samples at 1550 °C and residual porosity of less than 1% (Wang et al., 2001), and 390 GPa for hot-pressed samples at 1550 °C-1650 °C with porosity < 2% (Chakraborty et al., 2000; Sekino and Niihara, 1995). Lower modulus values (339 GPa) have also been cited for pressureless

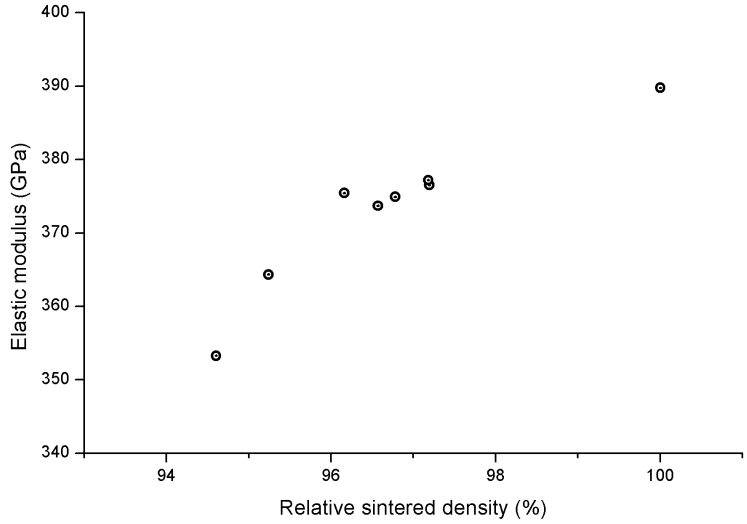

Figure 6.1: Young's modulus of the sintered alumina samples as a function of their relative density.

sintered Al_2O_3 samples at 1700 °C and a fired density of 3.89 g cm^{-3} (Konopka and Oziebo, 2001).

Fig. 6.1 portrays the experimental modulus values as a function of relative density for all sintered alumina samples that have been measured via IET. The highest modulus is attained for the most dense specimen and reaches the value of 390 GPa, while most data reside around 375 GPa for samples with a relative sintered density of approx. 97%.

Taking into consideration the average relative density of the sintered Al_2O_3 specimens (97.4%) and the formulations that have been discussed in a previous section for the porosity-correction of the modulus, it can be concluded that the linear approximation in the form of Eq. 2.5, as well as the exponential relation in the form of Eq. 2.8, can be used to successfully fit the measured values, as these suggest a reduced modulus of 379 GPa for ϕ=0.026.

The average impact strength of the pure Al_2O_3 samples was evaluated via the impact test method and was calculated to be 4.9 $\pm$ 0.8 kJ m^{-2}. Despite some variation in the densification of the different specimens, no correlation among the sintered density and the impact strength of the samples could be detected (unlike elastic modulus), indicating that the amount of energy required to fracture a specimen is dependent upon various parameters; residual porosity being only one of them.

Fig. 6.2 portrays the hardness variation as a function of porosity according to

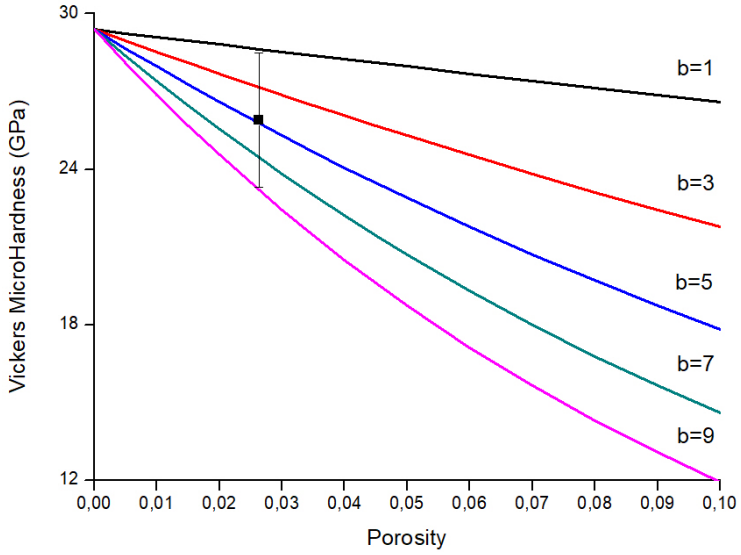

Figure 6.2: Variation of hardness with residual porosity according to Eq. 2.9 by assigning different values to the constant b. The measured hardness of pure Al_2O_3 is also shown (solid square).

the prediction of Eq. 2.9. Different values have been assigned to the correction parameter, b, that varies among 1 and 9. The average hardness value of the pure alumina specimen that was measured in this study is also shown in this graph. It can be seen that, for b=5, the theoretical calculation coincides with the measured value of Al_2O_3. Lower values (b<5) appear to overestimate the hardness, whereas higher values (b>5) seem to underestimate it.

6.2.2 Metal-Alumina composites

The experimental data of the mechanical response of the metal-reinforced Al_2O_3-matrix composites are listed in Table 6.1. The results of the Cu-alumina, W-alumina, and W-Cu-alumina composites are discussed in this section consecutively.

The elastic modulus data are initially compared with the theoretical predictions that are estimated by employing the formulations of Voigt and Reuss (Eqs. 2.18 and 2.19, see section 2.2.1.2). When these bounds are widely-spaced, their arithmetic mean in the form of Eq. 2.20 is also used to describe the measured data. The values that have been used for the theoretical modulus of each phase correspond to: E_m=400 GPa for polycrystalline Al_2O_3 (Pabst, Tichá, and Gregorová, 2004; Green, 1998), E_{f1}=130 GPa for copper, and E_{f2}=411 GPa for tungsten (Cardarelli, 2008).

Table 6.1: Mechanical response of the composites with listed data of impact strength, elastic modulus and Vickers microhardness.

Composite type	**Impact Strength** (kJ m^{-2})	**Elastic Modulus** (GPa)	**Vickers MicroHardness** (GPa)
Al_2O_3	4.9 ± 0.8	374.4 ± 10.8	25.9 ± 2.6
1Cu	7.6 ± 1.8	353.9 ± 5.4	23.5 ± 4.5
3Cu	7.1 ± 1.4	332.7 ± 4.0	21.4 ± 4.6
5Cu	2.9 ± 0.4	334.8 ± 17.7	19.4 ± 3.0
8Cu	2.3 ± 0.2	323.7 ± 14.2	20.6 ± 2.1
10Cu	3.1 ± 1.1	293.1 ± 15.6	20.3 ± 4.4
05W	5.4 ± 0.3	384.0 ± 4.6	23.0 ± 2.6
2W	5.7 ± 1.3	379.0 ± 13.8	23.7 ± 3.1
4W	3.8 ± 0.7	347.4 ± 21.5	20.0 ± 2.8
6W	4.7 ± 1.0	338.4 ± 34.6	21.2 ± 4.3
1Cu - 1W	6.8 ± 1.0	367.5 ± 12.3	23.4 ± 3.7
3Cu - 01W	3.5 ± 0.5	363.6 ± 7.0	21.3 ± 3.9
5Cu - 1W	3.8 ± 1.6	323.6 ± 13.9	17.8 ± 2.2
10Cu - 05W	7.4 ± 1.0	222.1 ± 14.7	-
10Cu - 5W	2.0 ± 0.5	267.6 ± 8.8	15.4 ± 4.0
20Cu - 2W	-	96.1 ± 12.7	-

Taking into consideration the residual porosity of the Al_2O_3 matrix material of each composition, the value of the elastic modulus has to be adjusted accordingly. To account for this effect, Eq. 2.8 (section 2.1) was used as it best described the experimental data.

In the case of the W-Cu-alumina composites, Eqs. 2.18 and 2.19 had to be adjusted to describe three-phase composite materials. Therefore, the upper and lower bounds can be calculated as following:

$$E^{+} = E_c = E_m V_m + E_{f1} V_{f1} + E_{f2} V_{f2} \,, \tag{6.1}$$

$$E^{-} = E_c = \left(\frac{V_m}{E_m} + \frac{V_{f1}}{E_{f1}} + \frac{V_{f2}}{E_{f2}} \right)^{-1} . \tag{6.2}$$

The Vickers microhardness data are also compared to the theoretical predictions. To facilitate this comparison, the rule of mixture approach (Eq. 2.26) is utilized to take into account the contribution of both phases, in combination to the porosity-correction formulation (Eq. 2.9). These yield the following equations for two-phase (Cu-Al_2O_3, W-Al_2O_3), and three-phase (W-Cu-Al_2O_3) composites, respectively, that are used to estimate the theoretical hardness values of each composition given its metal content and void fraction:

$$HV = V_f HV_f + (1 - V_f) HV_{Al_2O_3} \exp(-bP) \,, \tag{6.3}$$

$$HV = V_{f1} HV_{f1} + V_{f2} HV_{f2} + (1 - V_{f1} - V_{f2}) HV_{Al_2O_3} \exp(-bP) \,. \tag{6.4}$$

The parameters HV_f and $HV_{Al_2O_3}$ are substituted by 0.37 GPa for copper, 3.53 GPa for tungsten, and 29.4 GPa for alumina (Cardarelli, 2008).

Cu-Al_2O_3 composites

The impact test data for the copper-reinforced alumina composites are depicted in Fig. 6.3a as a function of the content of copper. It can be seen that the impact strength initially increases (composite types 1Cu and 3Cu), but reduces considerably for higher copper loading (above 5 vol.%). The average values for the low compositions exceed 7.0 kJ m^{-2} suggesting a toughness ratio (over the pure alumina) of around 1.5. However, the specimens with higher copper content exhibited an average impact strength of around 3.0 kJ m^{-2},

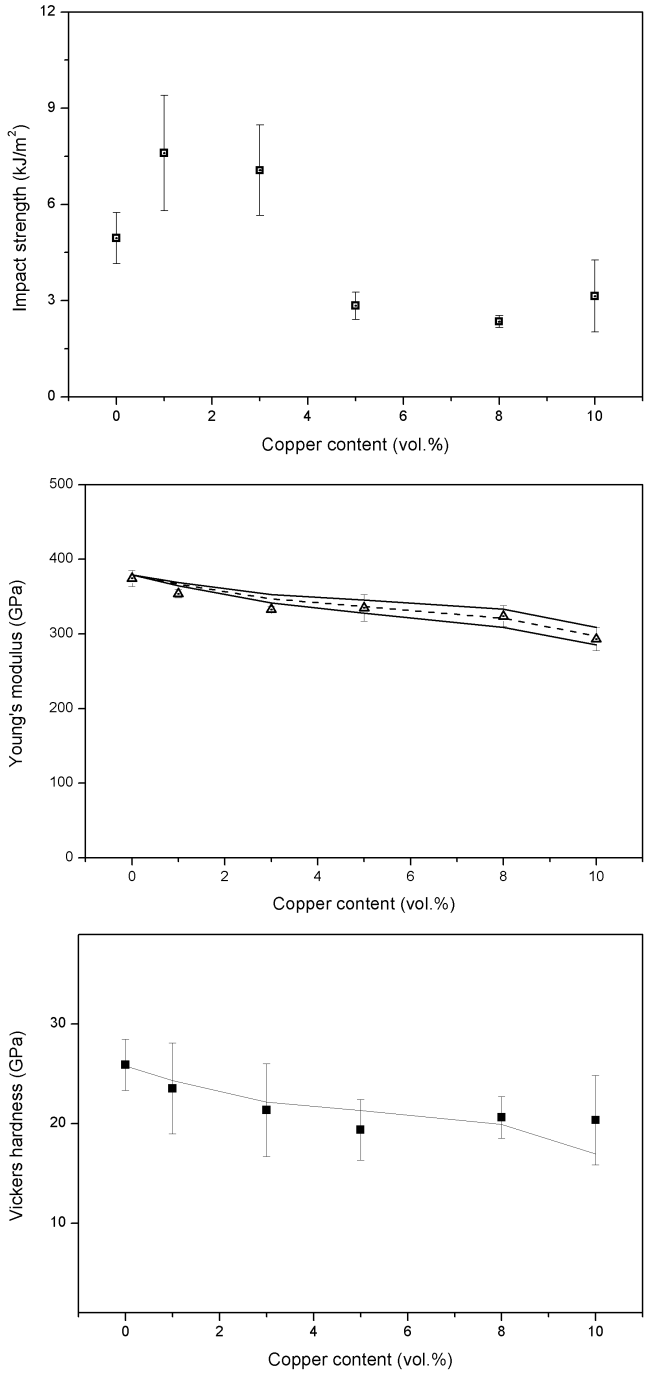

Figure 6.3: Mechanical response (Impact Strength, Young's Modulus, and Vickers MicroHardness) of the Cu-Al_2O_3 composites.

which is a notably reduced value in comparison to the impact strength of pure Al_2O_3.

The enhancement in the toughness response of the composites may be attributed to the activation of different mechanisms that relate to the interaction of the propagating crack with the dispersed copper particles. Crack bridging may be the most possible mechanism given the ductility and high elongation ratio of copper, however, the contribution of other mechanisms should not be ruled out. Reports on copper-reinforced alumina-matrix composites have attributed the augmented fracture toughness to the deflection of the cracks by the particles (Wang et al., 2001) and the debonding along the particle/matrix interface (Aldrich and Edirisinghe, 1998), the effect of residual stresses in the matrix along with crack bridging (Oh, Sekino, and Niihara, 1998), as well as the concurrent effect of bridging and deflection of the crack by the particles, with the former being considered as the dominant mechanism, and the latter having only a small toughening potential (Travitzky, 1998).

A decrease in the modulus of the samples can be observed in Fig. 6.3b, from the average value of 374 GPa measured for pure alumina to approx. 300 GPa for 10 vol.% copper loading. These results are compared to the porosity-corrected upper and lower bound predictions, among which the VRH line can be discerned. The compositions with the lower copper content (i.e. 1 and 3 vol.%) are close to (and below) the lower bound, while the ones with the higher copper content coincide with the VRH theoretical line. This behavior is related to the overall mechanical response of the composites, which will be discussed later in this chapter. The modulus values that have been attained in this work can adequately compare with values that have been measured for similar metal-alumina systems. (Wang et al., 2001) measured the modulus of Cu-Al_2O_3 composites to be 351 GPa for 5 vol.% copper content, with copper particle size around 21 μm, and residual porosity of less than 1%.

The Vickers microhardness test performed on the copper-alumina samples included approximately 15 indentations per composition. Fig. 6.3c depicts the measured data as a function of the copper volume fraction. The solid line represents the theoretical calculation that takes into account both the copper loading and the porosity of the alumina matrix. It is evident that the values are reduced as the copper content increases, and this is attributed to the addition of the soft copper phase, as well as the formation of voids upon the dispersion of the metallic particles in the matrix material. An overall good agreement between the theoretical values and the measured hardness data can be discerned in this graph.

W-Al_2O_3 composites

Fig. 6.4a shows the results of the impact strength of the tungsten-alumina composites as a function of W volume fraction. The impact strength initially exhibits a mild increase for low W contents (composite types 05W and 2W), while the values are slightly reduced for higher contents (4W and 6W composites). Unlike the noticeable variation of the Cu-Al_2O_3 samples, the tungsten-alumina composites exhibited a rather restricted trend. The enhanced values are in such range that result in a toughness ratio of approx. 1.1. This points towards the deflection and/or the branching of the crack and its propagation through the matrix by avoiding the dispersed tungsten particles. Although tungsten has a substantially higher fracture toughness than alumina, its ductility is low (having an elongation ratio of only 2%) which strongly suggests that the bridging of the crack by the tungsten particles is rather unlikely to be realized. In addition, the fact that its elastic modulus is proportional to that of the alumina matrix does not favor the attraction of the crack to the particles.

Comparable results have been reported in similar studies regarding tungsten-alumina nanocomposites prepared via SPS (Rodriguez-Suarez et al., 2009). In their work, (Sekino and Niihara, 1995) measured only a slight increase in the toughness of hot-pressed W-Al_2O_3 nanocomposites and reported a toughness ratio of approx. 1.1 for 2.5 vol.% W, and 1.2 for 5 and 7.5 vol.%. Later, (Sekino and Niihara, 1997) showed a small increase for hot-pressed samples with tungsten content of more than 7.5 vol.% and observed the bridging and/or the pulling out of tungsten particles.

Fig. 6.4b depicts the Young's modulus data of the tungsten-alumina composites in comparison to the theoretical predictions of the rule of mixtures, as a function of tungsten content. It can be observed that the modulus values initially increase with the addition of tungsten particles for content of 0.5 vol.% and 2 vol.%. This is attributed to the dispersion of a second-phase that is relatively stiffer than the matrix material, and the fact that the total residual porosity is quite low for these two compositions. For the 0.5 vol.%, in particular, the relative density was as high as that of plain Al_2O_3. The further addition of tungsten particles (content of 4% and 6%) reduces slightly the modulus and this is related to the higher amount of residual porosity in these samples. In total, the measured data are in accordance with the theoretical lines (upper and lower bounds) which coincide and overlap in the case of the W-Al_2O_3 system due to contiguous modulus values between the two phases.

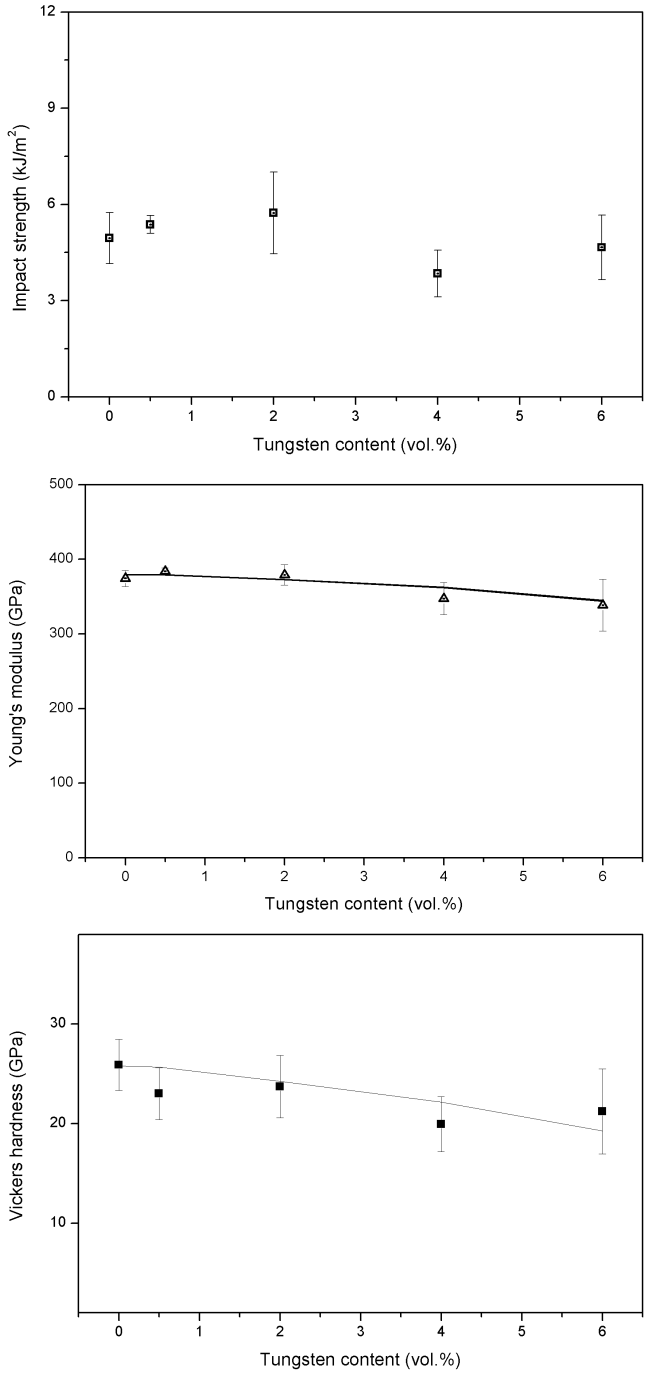

Figure 6.4: Mechanical response (Impact Strength, Young's Modulus, and Vickers MicroHardness) of the W-Al_2O_3 composites.

Literature data for tungsten-reinforced Al_2O_3-matrix composites display relatively higher values for the elastic modulus of the samples than those obtained in this study, but these correspond to the presence of tungsten particles with average sizes that lie in the nm range (Sekino and Niihara, 1995; Sekino and Niihara, 1997). In addition, the porosity in these studies was low (less than 2%) and therefore, did not have an effect on the elastic response of the specimens. Nevertheless, both reports discussed the mismatch between measured values and predictions, with either higher or lower values than expected, and these were related to internal residual stresses deriving from the thermal expansion mismatch between W and Al_2O_3 phases.

The Vickers microhardness of the sintered tungsten-alumina samples was determined by recording an average of 18 indentations per each composition. Fig. 6.4c shows the comparison of the data with the theoretical values as a function of tungsten loading. Similarly to the copper-reinforced alumina composites, the W-Al_2O_3 samples exhibit a reduction in the hardness values, which can be fitted by the predictive rule-of-mixtures line.

W-Cu-Al_2O_3 composites

The impact test data of the three-phase W-Cu-Al_2O_3 composites are shown in Fig. 6.5a as a function of the total metal loading. It can be seen in this graph that the 1Cu-1W and 10Cu-05W composites exhibited a higher impact strength than that of the unreinforced Al_2O_3 matrix. The measured values, around $7.0\,\mathrm{kJ\,m^{-2}}$, are reminiscent of the values obtained for the copper-alumina composites with a low Cu content, suggesting a high possibility of copper particles contributing to the toughness via the bridging of the crack.

We have mentioned that the addition of two different metallic inclusions in the brittle Al_2O_3 matrix has not been widely studied (yet), and, as a consequence, three-phase composites remain a rather unexplored complex structure in terms of fracture and resistance to crack propagation. In a similar study, (Ji and Yeomans, 2002a) reported a toughness increase for Al_2O_3-matrix composites with dispersed chromium/nickel inclusions which was attributed to the deflection of the advancing crack by the particles. The Cr/Ni/Al_2O_3 composite is a comparable system to our W-Cu-Al_2O_3 given the CTE differences among the three constituent phases, i.e. Cr has a lower and Ni has a higher CTE than alumina. Nonetheless, in view of the fact that all metal/alumina composites exhibited a higher toughness than the neat alumina, the residual stresses around the particles were considered to have only small effect on the fracture toughness behavior of the samples in their work.

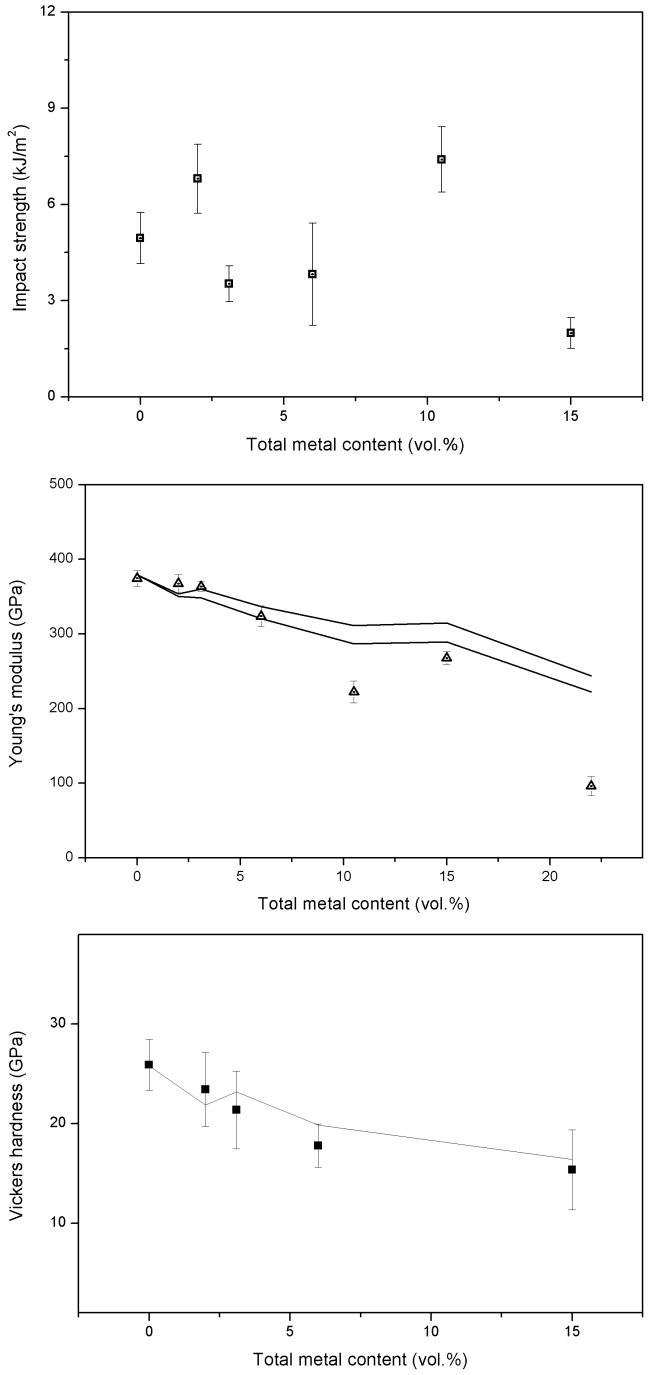

Figure 6.5: Mechanical response (Impact Strength, Young's Modulus, and Vickers MicroHardness) of the W-Cu-Al_2O_3 composites.

The measured elastic modulus data of the mixed W-Cu-alumina composites are shown in Fig. 6.5b. The results are in good agreement with the theoretical calculations after taking into consideration the residual porosity of the matrix for the composites with relatively low contents of metal phase. However, a deviation can be observed for the composites with the highest metal loading, which maximizes for the 20Cu-2W composite type and is related to the presence of cracks that have been formed on the samples.

The Vickers microhardness of the W-Cu-Al_2O_3 samples was estimated by taking an average of 17 indentations per composition. However, due to the presence of some cracks and increased amount of porosity for the composites with the highest metal loading (20Cu-2W) no definite measurements could be realized and the results are not included. It can be seen in Fig. 6.5c that the trend resembles that of the other metal-alumina composite samples studied in this work; i.e. a reduction in the hardness of the composites is exhibited due to the presence of the less hard second-phase inclusions and the consequential presence of pores and voids, while the theoretical estimation concurs with the measured data.

6.3 Toughness

The results of the impact strength of the two-phase metal-alumina composites correlate well with published data: i.e. initial increase for samples that contain a relatively low amount of second-phase inclusions, followed by a reduction exhibited for composites with a relatively higher metal loading. This implies that toughness does not conform to a linear response, but follows a rather non-linear trend. This urges us to forward the discussion on two levels: (i) the factors that contribute to the toughness enhancement, and (ii) the factors that bring about the reduction of toughness.

Recapping from earlier sections, we should note that toughness is a structure-sensitive mechanical property that depends on multiple microstructural features of the material. Unlike the rather structure-insensitive modulus of elasticity, dependent mostly on composition (i.e. metal loading), toughness might also depend on particle size, particle/matrix interface, and/or other parameters as well (Ahmed and Jones, 1990; Fu et al., 2008). This renders the exploitation of the full potential of the second-phase particles a particularly demanding and difficult task in the preparation of metal/alumina composites with enhanced resistance upon fracture, and not so simple as the rule of mixture.

We have discussed that the introduction and dispersion of a metallic second-phase throughout a brittle ceramic matrix intends to form an interaction between the particles and the propagating crack in order to "postpone" the sudden catastrophic failure of the material. This is usually accomplished either via the bridging of the tip of the crack by ductile inclusions, or via the change of its path through the deflection by the particles, the bowing or the branching of the crack, its propagation along the particle/matrix interface, the pull-out of the particles, or other possible processes.

A well-developed formulation, suggested by (Ashby, Blunt, and Bannister, 1989), can be used to calculate the fracture toughness of metal/ceramic composites assuming that the metallic particles can stretch during fracture and that the mechanism of crack bridging is activated. According to the following relation:

$$\Delta K_{ic} = \left(C V_f \sigma_o \alpha_o E\right)^{1/2}, \tag{6.5}$$

the fracture toughness increase (ΔK = K_{comp} - K_m) is equal to the product of the parameters: C; a constant that depends on the degree of constraint of the particle, V_f; the area fraction of the metallic particles that are intersected by the crack, σ_o; the yield strength of the particle, α_o; the particle radius, and E; the elastic modulus of the particle.

Accordingly, a higher contribution to toughening is derived from the dispersion of metallic particles with a high yield strength, a high elastic modulus, a large diameter, and a high content. For instance, one can simply calculate that the dispersion of 5 vol.% tungsten particles with 10 μm diameter and a maximum constraint will contribute to as high as 13.4 MPa$\sqrt{\text{m}}$ (lets remind here that the toughness of Al_2O_3 is only around 3 - 5 MPa$\sqrt{\text{m}}$). Yet, the same amount of copper particles with same size and degree of constraint will only contribute as high as 2.7 MPa$\sqrt{\text{m}}$, while nickel and iron around 4.5 - 4.9 MPa$\sqrt{\text{m}}$. This calculation is, of course, only valid in case the crack is attracted to the particles and does not by-pass them.

The study of actual metal/alumina systems, though, implies that toughness improvement is not as simple and, certainly, not linear. For instance, albeit tungsten has a higher yield strength than copper, its elongation ratio is negligible compared to that of copper, and this should drastically affect the overall response of the particles. It is clear at this point, that this formulation triggers the introduction and discussion of several parameters and their effect on the toughness response of a composite material:

6.3.1 Particle Loading

In theory, the higher the particle loading the higher the toughening effect, provided that we have a highly ductile inclusion and a notable possibility for crack bridging to occur. Nonetheless, it appears that there is usually a threshold (critical metal volume fraction) beyond which the contribution of the particles is not beneficial, but diminishes the mechanical behavior of the composites. The reduction in the fracture toughness exhibited by various metal/Al_2O_3 composites at a relatively high metal loading is dependent upon the effect of various factors and parameters such as: enlargement of particles or formation of agglomerated regions, decrease in sintered density, weak particle/matrix interfaces (Lu et al., 2000; Tuan, Wu, and Yang, 1995; Diaz et al., 2003). Therefore, it is not the actual presence of more particles in the matrix that is detrimental for fracture toughness, but the latter can be the result of their presence. In addition, it should be noted that not all particles interact with the propagating crack, as there is the possibility for the crack to propagate around some inclusions, resulting in a fraction of them that will remain relatively undisturbed by the fracture process (Tuan and Brook, 1990). This, of course, does not apply solely to the crack bridging mechanism, but all possible toughening mechanisms.

6.3.2 Particle Size

Based on the suggestion of Eq. 6.5, the dispersion of bigger particles in a brittle ceramic matrix should yield a higher toughening increment than that of smaller ones. Indeed, by keeping fixed the rest of the parameters and only changing the value of the particle size, one can easily estimate the major difference that is derived even among small differences in size. However, based on published data, one can deduct that the dependence of toughness on particle size is not always linear. There are studies that report a higher fracture toughness accompanied by: a reduced particle size (Konopka and Oziebo, 2001), a fixed particle size (Tuan, Chen, and Yang, 2007), as well as an increased particle size (Tuan and Chen, 2002). In addition, the particles are usually getting more coarse with an increase in metal volume fraction, while usually increasing the volume fraction yields a higher toughness response. Therefore, the effect of each parameter (particle loading and particle size) can not be veritably isolated.

6.3.3 Particle/Matrix Interface

The interface, i.e. the surface that is formed between the particle and the matrix, includes the cohesion and bonding strength between the two phases. According to the work of (Ashby, Blunt, and Bannister, 1989), the constant C (Eq. 6.5) varies from 1.6 for maximum constraint, up to 6 for minimum constraint, although other values have also been ascribed to the parameter (Tuan and Brook, 1990). This implies that a moderately bonded particle-matrix (high C) allows for interface debonding and exploitation of the second-phase, while a perfect bonding (low C) poses limitations and does not allow the full exploitation of the toughening effect of the particles. The benefit of an appropriately bonded particle/matrix interface for toughness enhancement has been thoroughly discussed in the work of (Li and Zhou, 2013a; Li and Zhou, 2013b).

We have previously argued that, in the case of the copper-Al_2O_3 composites, the bridging of the cracks by the copper inclusions must have mainly contributed to the enhanced impact strength (1Cu and 3Cu composites) in view of the high fracture toughness and high elongation ratio of copper. Further, the fact that the Cu modulus is substantially lower than the Al_2O_3 modulus promotes the attraction of the crack by the particles and facilitates the effectiveness of the mechanism (Budiansky, Amazigo, and Evans, 1988). An additional observation relates to the elastic moduli data of the particular compositions that are in agreement with the lower bound prediction, in contrast to higher compositions fitted by the VRH model, suggesting some degree of freedom for the copper particles to stretch. This relates to the requirement for an appropriate bonding between the metal and ceramic phases in order for the crack bridging mechanism to operate, as well as the debonding along the particle/matrix interface.

The larger volume contraction of the particles than the matrix, during cooling, results in the formation of voids around them. Fig. 6.6 verifies the formation of an empty space between the smooth surface of a spherical copper inclusion and the grains of the alumina matrix. This apparently comes from the larger contraction of the copper particle during cooling from the sintering temperature. While the density of solid copper is $8.941\,\mathrm{g\,cm^{-3}}$, the density of liquid copper at its melting point (1083 °C) is $7.992\,\mathrm{g\,cm^{-3}}$ and near the sintering temperature (1527 °C) it is $7.636\,\mathrm{g\,cm^{-3}}$ (Cahill and Kirshenbaum, 1962). As a result, a droplet of liquid copper shrinks around 12% when cooled from the sintering temperature to its solid state. Therefore, the difference in shrinkage between the surrounding alumina and a liquid copper droplet of 40 μm in diameter would be around 1,5 μm (Fig. 6.6 suggests an interfacial void of the same order of magnitude for such a particle), whereas for a smaller particle of around 5 μm the interfacial gap would only be 0.2 μm.

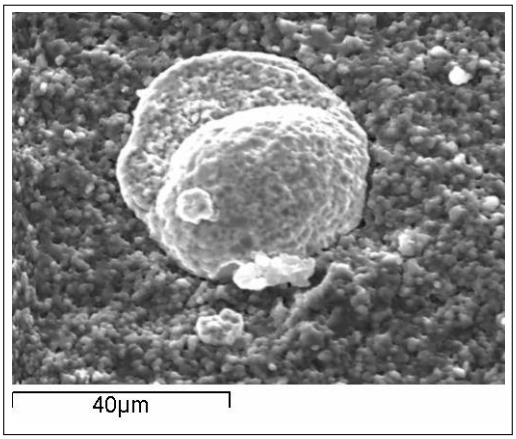

Figure 6.6: A spherical copper particle between the alumina matrix grains.

Comparable systems to Cu/Al_2O_3 (in terms of af>am) are those of Ni/Al_2O_3, Ag/Al_2O_3, and Fe/Al_2O_3 (Li, Huang, and Guo, 2003). A weak interface is induced among the two phases, and in combination with the ductile nature of the metallic inclusion, is believed to contribute to the toughening of metal/alumina composites via a void-induced crack-tip blunting mechanism (Lu et al., 2000).

6.3.4 Porosity

The discussion, so far, was an attempt to elucidate the effect of a summation of parameters on the toughness response of metal-reinforced alumina-matrix composites. Albeit these were closely related to the proposed formulation of Eq. 6.5, an additional and rather associated factor that should also be examined is that of porosity.

It is well known that both modulus of elasticity and hardness are mechanical properties affected by porosity and exhibit a reduction upon the increase of void spaces in a material. An analogous approach may be used for the toughness of monolithic ceramic materials by employing exponential formulations to correct for the residual porosity (Rice, 1996). Yet, these may be considered simplistic in the case of metal-reinforced ceramic-matrix composites considering a plethora of studies with published results of: (i) augmented toughness behavior despite some porosity in the matrix, and (ii) minimal porosity but not any substantial toughness increase. Therefore, the preparation of fully-dense samples does not ensure an effective interaction of the propagating crack with the second-phase particles, while some porosity should not be directly considered detrimental for the fracture toughness response of the composites.

Tuan and Brook, 1990 measured a toughness that was twice that of pure alumina for 13 vol.% Ni/Al_2O_3 composites prepared via pressureless sintering and a relative density around 95%. Similarly, a toughness increase of 20% was measured for 5 vol.% Ni/alumina composites with RD of approx. 96% (Chen and Tuan, 1999). Comparable results can be found in the study of Chou and Tuan, 1995 for Ag/Al_2O_3 composites and sintered densities that varied in the range of 91-98%, as well as in the work of Breval et al., 1992; Breval and Pantano, 1992 who measured a toughness of 8.3 MPa$\sqrt{m}$ for 50 wt.% nickel content in Al_2O_3, albeit the reported relative density of only 74%. The increase was attributed to the deflection and the bridging of the crack by the Ni particles, which were considered to be the predominant toughening mechanisms, in conjunction with crack bowing and microcracking.

These studies are an indication that, although achieving a near theoretical density after sintering is of paramount importance, given that the flaw might be pinpointed under a fracture toughness test, yet the toughness response of a composite material may be improved via the addition of a second-phase despite some porosity that has remained in the compact after sintering. Besides, porosity is only one defect among several possible flaw types present in ceramics that are induced during: (i) processing (inclusions, pores), (ii) design (sharp corners), (iii) service (thermal stresses, environmental degradation) (Chawla, 2013a). Further, it is important to discern the type of pores, i.e. open or closed pores, fine, large or clusters of pores, as well as their association with the matrix and/or the dispersed particles (pores located throughout the matrix material, around or within the inclusions).

At this point, we should also introduce the possibility of fracture enhancement via a crack-tip blunting mechanism (Deng et al., 2004). Crack blunting describes the interaction of the cracks with the pores that are present in the specimen, i.e. the crack might move towards a pore during its propagation and cause blunting which enhances the fracture resistance.

In this study, the increase in particle loading brought about an increase in the amount of porosity, as the dispersion of the second-phase particles hindered the densification process of the matrix material. In addition, the absence of an applied pressure during sintering did not assist the elimination of voids. Nonetheless, the evenly distributed particles throughout the matrix served their purpose by prolonging the crack path and by forming a more tortuous route during which any of the aforementioned mechanisms, or the concurrent operation of more than one was activated (Xia and Terence, 1994). For higher contents of metallic particles, though, a summation of factors might have acted as stress raisers and facilitated an effortless propagation of the crack through the Al_2O_3 matrix.

6.3.5 The metal inclusions

Regarding the reduced impact of the Cu-Al_2O_3 composites, albeit the size distribution of the copper particles, their size was approximately fixed and did not change significantly with particle content. This is a strong indication that other parameters must have an effect upon the reduction of the fracture resistance. These relate to the surface characteristics that have been discussed in earlier sections, i.e. the increase of open porosity with copper content, and the formation of a core-skin structure (see Fig. 5.10) which has not assisted the beneficial contribution of the dispersed ductile particles in the bulk of the specimens. Further, the alumina-rich surface (i.e. copper-depleted) in combination with some open pores must have expedited the initiation of the crack.

Concerning the tungsten-alumina composites, two factors that need to be taken into consideration relate to: (i) the mechanical response of tungsten, and (ii) the bonding of tungsten with alumina. The first parameter suggests that, although the fracture toughness of W is higher than the fracture toughness of Al_2O_3, its elongation ratio is rather low and, therefore, the bridging of the crack by the tungsten particles is unlikely. Further, the modulus of tungsten is comparable to the modulus of alumina discouraging the attraction of the crack by the particles. The second parameter relates to the CTE differences of the two phases, i.e. the mechanical bonding that must have been formed between the tungsten particles and the Al_2O_3 matrix, as the matrix contracted relatively faster than the inclusions ($a_m > a_f$) and must have gripped the particles during cooling. This also suggests that debonding along the interface is not highly possible, and that the mild increase in fracture resistance may be related to the deflection or the branching of the crack caused by the presence of the particles. Further, the presence of agglomerated particles as well as the reduced density measured for higher W contents may be considered responsible for the lower impact strength of the particular samples.

As for the three-phase W-Cu-Al_2O_3 composites, the impact response of the 10Cu-05W is rather interesting and comes to verify the previously discussed studies relating to samples that exhibit an enhanced toughness despite some porosity that has remained in the sintered body. For this particular composition both the open and total porosity were around 4%, while the measured modulus of elasticity fell far from predictions. A highly possible toughening mechanism in that case is that of microcracking, which renders the ceramic matrix more compliant around the inclusions by reducing the modulus of elasticity locally. This may cause the shielding of the crack from the applied load and enhance the fracture resistance of the matrix (Evans and Faber, 1981; Hutchinson, 1987; Giannakopoulos and Breder, 1991). Further, the

core-skin structure of the copper-alumina samples was not present in the W-Cu-alumina specimens (see Fig. 5.10), and the absence of a copper-depleted surface has assisted an effective contribution of the copper inclusions i.e. the crack initiation demanded additional energy and contributed, thus, to the toughness.

6.4 Elasticity

As discussed in previous sections, the dispersion of the (usually) softer particles in the stiff Al_2O_3 matrix results in reduced Young's modulus values. Most of the relevant studies on metal/Al_2O_3 composites have found a relatively good or an excellent agreement between the measured data and the theoretical calculations, usually be employing simple mixtures rules. A number of studies, though, has discussed the effect of possible parameters on the modulus of elasticity, in an effort to interpret the deviation that has been observed (see Appendix D for further discussion concerning the modulus of elasticity).

Tuan and Chen, 2002 reported an elastic modulus value of 396 GPa for pure Al_2O_3, that reduced to as low as 285 and 274 GPa for 8.7 vol.% and 12.9 vol.% nickel content, respectively. Although the predictions were not porosity-corrected, the low amount of porosity (<3%) could only account for a fraction of the deviation which exceeded 20% for these particular compositions. Accordingly, in the work of Aldridge and Yeomans, 1999 a major mismatch was reported among measured modulus data and theoretical calculations for iron/alumina composites, which did not change significantly after the corresponding porosity correction, and was attributed to a poor interfacial bonding between the particles and the matrix. The lower (than anticipated) values have also been correlated to the possible presence of microcracks and/or residual stresses attributed to CTE mismatch for various metal reinforcements dispersed in the Al_2O_3 matrix, such as nickel (Tuan and Chen, 2002) and tungsten (Sekino and Niihara, 1995; Sekino and Niihara, 1997). Some thoughts on possible causes for this discrepancy are given in Appendix D.

In the present study, the experimental modulus data of most of the fabricated composites lie within the theoretical predictions of Voigt and Reuss bounds. This suggests a satisfactory load transfer from the matrix material to the reinforcement phase. The homogeneous dispersion of the metallic particles in alumina must have contributed to an even distribution of stress throughout the matrix material and the second-phase inclusions. However, the compositions that have exhibited an augmented toughness behavior (mostly composite samples reinforced with copper particles) have also lower modulus

values than the theoretical predictions. This observation relates to the 1Cu and 3Cu composite samples, which show some minor difference between the measurements and the predictions, as well as to the 10Cu-05W composite type. The latter is related to some degree of freedom for the particles to stretch during fracture.

The results concur with published data of similar composite systems, where these are applicable. For instance, the values of the copper-alumina samples (5Cu) can be sufficiently compared to the study of alumina samples reinforced with copper particles of similar size. On the contrary, relevant studies on metal/alumina nanocomposites, with finer metallic particles (average sizes in the nm range), reported higher modulus values and can not be directly compared to the composites prepared in this work. The elastic modulus is mostly dependent on the volume fraction of the particles, rather than the particle size, yet, when the particles are in the nanometer range, the surface area increases and may affect the composite modulus (Lewis and Nielsen, 1970).

Although, in theory, the elastic and thermal mismatch among the constituent phases is considered a limitation, given that it produces residual stresses in the matrix, it has been found that it can have an advantageous effect on toughness and contribute to its enhancement via the activation of the microcracking mechanism (Evans and Fu, 1985) or a crack blunting mechanism (Wang et al., 2001; Yao et al., 2005). Low residual stresses appear, thus, to be essential in the toughening of brittle ceramic materials by ductile inclusions (Krstic, Nicholson, and Hoagland, 1981). Oh, Sekino, and Niihara, 1998 applied in their study a formulation proposed by Taya et al., 1990 and reported the contribution of the residual stresses in the augmented toughness response of copper/alumina composites. This must have been the case for the 10Cu-05W composite type, in view of the high content of the ductile copper particles. Further, the residual stresses in the three-phase composites are expected to be particularly high bearing in mind the notable contrast in values for both elastic and thermal properties.

The effect of internal residual stresses caused by the thermal and elastic mismatch is an issue that has frequently preoccupied authors. Microcracks are frequently formed in the matrix during the manufacturing process, and these can either enhance the fracture response of the composite material or diminish it. This depends on their location and distribution in the matrix material, as the various microcracks are free to nucleate away from the main crack (Faber and Evans, 1983b). If the microcracks are only situated around the inclusions and reduce the elastic modulus locally, then they induce the attraction of the crack to the particle. On the contrary, if the microcracks are

present throughout the bulk of the matrix, then the global modulus is reduced and the fracture response is diminished (Roesler, Harders, and Baeker, 2007).

6.5 Hardness

Clearly, the dispersion of metallic particles throughout a hard alumina matrix will also reduce its hardness values. The Vickers microhardness measurement suggests that the hardness of all sintered samples is reasonably high, although one should keep in mind that the values tend to appear slightly higher on account of the low load that has been applied during the measurement. The metal-reinforced composite samples are (as expected) less hard than the pure alumina matrix. However, the combination of low content of metallic particles and low porosity values has maintained the hardness at relatively high values, and has not drastically reduced it. Contrariwise, the higher contents of metallic phase have produced a more pronounced reduction with values around or below 20 GPa. In total, the measured data are compatible with the predictions by setting b=5 in Eqs. 6.3 and 6.4 for two-phase and three-phase composites, respectively, as this value best describes the hardness of the pure alumina specimens.

It should be noted that even though the microhardness measurement was performed on alumina-rich regions by avoiding the metallic particles, the result is affected by the overall structure of the composite, including both second-phase inclusions and residual pores. Therefore, although the indent is applied to a specific (visible) area, the result is influenced by its underlying structure: matrix material, "hidden" particles and "hidden" voids under the examined surface.

We have demonstrated through the hardness evaluation of the different compositions that the reduction is more or less independent of the reinforcing metal; i.e. copper or tungsten or both. All metals that are frequently used to prepare metal-Al_2O_3 composites have a much lower hardness than alumina. For instance, tungsten is considered a hard metal (among other metals) yet its Vickers hardness is only around 3.5 GPa. Similarly, the hardness of molybdenum is around 1.5 GPa, while for softer metals HV is < 1 GPa, such as nickel with 0.64 GPa, copper with 0.37 GPa, and silver with 0.25 GPa (*Vickers Hardness of the Elements*). This is also reflected in the calculated theoretical lines among the different compositions, that do not vary significantly for similar low metal contents and low porosity values.

Although hardness is a property of vital importance with regard to ceramic materials, it has not been extensively studied in relevant studies of metal/ceramic composites. Nawa, Sekino, and Niihara, 1994 and Wang and Wei,

1998 measured the Vickers hardness of Mo/Al_2O_3 composites and found that the values approximately obey the rule of mixtures, opposed to the work of Sekino and Niihara, 1995 and Sekino and Niihara, 1997 who reported that the hardness variation of the tungsten-alumina composites did not obey a linear relationship. A reduction in the Vickers hardness, measured under a load of 100 N for 15 sec, has been reported for Fe/Al_2O_3 composites (Konopka and Oziebo, 2001), as well as for Cr/Al_2O_3 composites measured under a load of 196 N applied for 10 sec (Ji and Yeomans, 2002a). Nonetheless, we have discussed that hardness is dependent upon a summation of factors including the applied load and loading duration, the geometry of the indenter, the properties of the material, the sample preparation, and, therefore, a comparison between measured and cited values is not advisable.

6.6 Summary

This chapter has presented the results that have been obtained from the evaluation of the mechanical response of the sintered Al_2O_3 and metal/Al_2O_3 samples including the elastic modulus determined via the impulse excitation technique, the microhardness according to Vickers, and the strength under an impact load.

It has been found that the experimental data of the modulus correlate well with the upper and lower bound predictions, and that the observed decrease is consistent (for most of the types) with porosity-corrected theoretical calculations for two-phase (Cu-Al_2O_3, W-Al_2O_3) and three-phase (W-Cu-Al_2O_3) composites. The homogeneous distribution of metallic particles in the alumina matrix has assisted an even load transfer between the constituent phases.

The microhardness of the composites decreased with metal loading, as anticipated, while the reduction was mild and indicated the fabrication of hard composite materials. The experimental data were in good agreement with the porosity-corrected calculations.

The impact strength of the metal/alumina composites was augmented for different compositions, while it followed a rather non-linear dependence on the amount of metallic particles, in contrast to stiffness and hardness.

The copper-reinforced alumina-matrix composites exhibited an enhanced impact strength for low Cu contents which was attributed to the low elastic modulus of copper that enabled the attraction of the crack by the particles, and its high CTE that resulted in some void space around the particles, during cooling. These have induced the propagation of the crack towards the particles, as well as its propagation via the particle/matrix interface and its

possible debonding. The void space around the inclusions, and the relatively weak bonding between the phases allows the deformation of the particles during fracture and the bridging of the crack by the ductile inclusions.

The tungsten-reinforced alumina-matrix composites have exhibited a mild increase in the impact strength for low W contents, possibly due to the deflection of the propagating crack and its further branching throughout the alumina matrix. The high elastic modulus of tungsten does not facilitate the attraction of the crack by the particles, while its low CTE results in a composite with a strong mechanical bonding, i.e. the matrix must have gripped the particles upon cooling given the higher expansion coefficient of alumina, and therefore, its larger contraction after sintering.

The W-Cu-reinforced alumina-matrix composites have demonstrated a more complex impact behavior than those of the Cu-Al_2O_3 and W-Al_2O_3 composites. The augmented toughness response is related to crack bridging, and the activation of the microcracking mechanism, in view of the major differences in expansion coefficients among the three constituent materials, in combination to the crack-tip blunting mechanism given the presence of residual pores in the samples. Further, the presence of copper particles close to the outer surface of the specimens (unlike the Cu-alumina samples with a copper-free surface) has highlighted the demand for additional energy in order to initiate the crack, and not only propagate through the matrix.

In conclusion, a substantial increase in the impact resistance of the metal-reinforced alumina-matrix composites has been attained in this study for relatively low contents of second-phase inclusions in the case of Cu-Al_2O_3 and W-Al_2O_3 composites, as well as for relatively higher contents in the case of W-Cu-Al_2O_3 composites. Although a direct comparison of the theoretical estimates with the experimental observations was not feasible, it can be concluded that, in spite of the toughening mechanism, the dispersion of the metallic particles in the brittle alumina matrix has indeed formed a longer and more tortuous path for the advancing crack and has elongated, thus, its course through the matrix material. The homogeneous distribution of particles has maximized the possibility of the crack to interact with a fraction of them, and dissipate energy either to fracture them, or to by-pass them and form alternative diverged routes (Krstic, 1983; Basista and Wglewski, 2006).

Toughness is an intricate mechanical property and this relates to the cumulative effect of various aspects. Besides its dependence upon the material characteristics, and not so straightforward porosity-correction of the values as it is for the elastic modulus and the hardness, the results are also affected by the measurement technique. For instance the measurement in this study was performed on unnotched cylindrical specimens which has perplexed, to

some degree, the evaluation of energy consumption arising from: (a) the initiation of the crack (from the surface of specimen), and (b) the propagation of the crack (through the bulk of specimen) (Pelleg, 2014). Further, the energy consumption for the propagation of the crack across the matrix may be associated to the required energy to: fracture the ceramic matrix, move towards the particles and deform them, fend off the particles and form alternative diverged routes (Sbaizero, Pezzotti, and Nishida, 1998; Raj and Thompson, 1994).

Any imperfections (surface or internal) that are present in a material can act as stress raisers and be accountable for the origin of the failure. In this work, special care was taken during the manufacturing of the specimens in order to avoid the formation of cracks - a common disadvantage of metal/ceramic composites- by adjusting a stepwise drying process and proper heating and cooling rates that assisted the stress relief of the compacts.

7 Conclusions and Future Directions

The present PhD dissertation was a study of the fundamental aspects of alumina-matrix composites reinforced with metallic inclusions. The scope of the thesis was to fabricate Cu-Al_2O_3, W-Al_2O_3, and W-Cu-Al_2O_3 composite materials, characterize them in terms of macro- and micro-structure, determine their mechanical behavior as a response to the variation of the metal loading, and investigate the interrelationships between structure and properties. Pure, untreated alumina samples were also prepared to assist a fruitful comparison with the reinforced samples and evaluate the contribution of the second-phase metallic inclusions.

The compositions under investigation in this study vary significantly due to the differences that arise from the properties of the metallic reinforcements that have been dispersed throughout the Al_2O_3 matrix. These relate to mechanical properties including: (i) density, (ii) modulus of elasticity, and (iii) ductility/toughness, and thermal properties of: (i) melting point, and (ii) expansion coefficient. Yet, it is the metallic bonding of each element that accounts for these contrasting properties and characteristics: the weak bonding of copper allows its deformation due to high ductility, but also yields a low melting point and high expansion coefficient, while the strong bonding of tungsten renders it hard and stiff, but also results in a high melting point and low expansion coefficient.

Albeit this diversity of properties between, not only the two metallic inclusions, but also among them and the matrix material, we have demonstrated in this study that the fabrication method and overall processing route is rather competent to form composites with augmented mechanical behavior. Should we give a definition of a composite; it is a material that satisfies the following conditions: (i) it is manufactured, (ii) it consists of two or more distinct phases with an interface that separates them, and (iii) it has characteristics that are not depicted by any of the components in isolation (Chawla, 2013b).

The fabrication was realized via the slip-casting processing route to achieve consolidation of a compact body from the initial powder particles. The capillary suction due to the porosity of the PoP molds assisted the formation of a dense cast, while preparing a well-dispersed stable slip was of paramount importance in order to synthesize reproducible samples with a homogeneous structure, high green density and low porosity. Both extremes i.e. flocculated or over-deflocculated slurry have undesired effects: the former leads to a cast with high porosity, while the latter renders the slip casting rather difficult.

The pre-sinter heating step of binder burn-out was realized to extract the additional aids that have been added to the slurry and remove any residual moisture/water that might have been absorbed from the samples. The organic burnout is a crucial step; one has to gradually remove the organics and refrain from damaging the green body, while an incomplete binder removal might bring about residual carbon in the body and diminish the properties of the specimen. The sintering step, a rather demanding and complicated process for mixed ceramic-metallic powders, included densification and pore shrinkage and resulted in sintered parts that were characterized by reproducibility.

The sintered composites exhibited a sufficiently dense microstructure over the entire metal loading range and a rather high density (>95%) for low additions of metallic particles. A uniform structure and a homogeneous distribution of second-phase inclusions has been achieved, which is attributed to the processing route that has been followed. The specimens did not exhibit any cracks formed on the surface after drying, debinding and/or sintering, indicating a stepwise process and a good adjustment of heating and cooling rates.

The presence of the metallic inclusions in the matrix hindered the densification process and resulted in pure Al_2O_3 specimens having the highest density. The parameters that influenced the densification relate to the thermal expansion mismatch and subsequent differences in the contraction of the phases during cooling, the low wettability of molten copper on alumina, and the presence of agglomerated tungsten particles.

The composites exhibited notably enhanced fracture properties derived from the dispersion and even distribution of metal particles in the ceramic matrix. The energy required to fracture the composite materials under a given impact load was more than that of alumina, indicating the synthesis of samples with a better resistance to crack propagation attributed to the activation of various toughening mechanisms. This was achieved for low metal loading compositions, for which the other mechanical properties were maintained at high values. The elastic modulus and Vickers microhardness exhibited

a reduction upon metal loading, as anticipated upon the addition of a soft metallic phase, but were not compromised and followed a theory-based trend after the corresponding correction for residual porosity and metal content contribution.

A deduction upon the literature survey on metal/alumina composites relates to the discrepancies in structure and properties among theoretically similar materials; however any differences in the characteristics of the materials and/or the processing characteristics might bring about a significant variation. This confirms the perplexity of the metal/ceramic composites and the further fascinating Materials Science interdisciplinary field.

7.1 Concluding remarks from the present study

Processing Route

- The slip-casting technique is suitable for the successful preparation of metal-particle reinforced alumina-matrix composites.
- The porous nature of the PoP mold and the capillary suction mechanism assist the formation of a dense cast in the green state.
- The debinding and sintering under a reducing atmosphere yield metal/ceramic composites free from oxides, that are undesired as they usually diminish the mechanical response of the sintered compacts.
- The structure of the samples is homogeneous with an even distribution of metallic particles in the matrix, and the sintered densities of the composites are reasonably high, rendering thus, the aqueous slip-casting route an alternative to other dry-pressing techniques.

Mechanical Properties

- The copper-alumina composites exhibit a high toughness increase, upon the addition of low contents of copper, attributed to the ductility of Cu and its ability to deform plastically during fracture. The high expansion coefficient of copper results in some void space around the particles which enables the propagation of the crack through the particle/matrix interface. Further, the low elastic modulus of copper facilitates the attraction of the crack by the particles.
- The tungsten-alumina composites maintain a stiff structure and, albeit their mild increase in impact resistance, are not restricted, in terms of high-temperature applications, in view of the exceptionally high

melting point of tungsten. The enhancement in impact strength is attributed to the deflection and/or the branching of the propagating crack through the matrix material.

- The tungsten-copper-alumina is a promising composite structure, in view of the high densities of the green parts and the augmented toughness response of some composite types. The ductility of copper along with the thermal mismatch of the constituent phases facilitates the enhancement of toughness via the bridging of the crack and the microcracking toughening mechanisms.
- The fit of experimental data with theoretical estimations is highlighted as an important parameter in terms of design, i.e. preparation of materials with an expected structure and mechanical response.
- The composites prepared in this study have served their purpose, i.e. they augmented the impact resistance of the matrix upon crack propagation but not at the expense of stiffness and hardness.

7.2 Propositions for further work

While the aims of the present PhD dissertation have been achieved, opportunities for further work regarding metal-alumina composites have arose from this study. These are discussed in this section.

Composition

An augmented mechanical response has been achieved for metal-alumina composites with a low metal loading, and therefore, it would be of great interest to prepare compositions with a further reduced content of metallic phase, i.e. less than 1 vol.% for copper and less than 0.5 vol.% for tungsten. This would, presumably, promote a better densification of the compacts, a lower amount of porosity, and an improved toughness response, with the green and sintered densities, as well as the overall response of the 1Cu, 3Cu, 05W, and 2W composites advocating strongly for such a hypothesis.

Properties

To widen the applicability of the composites, further investigation can be carried out towards the evaluation of their high-temperature mechanical behavior and response. It would be of interest to study the effect of temperature on elasticity, which can be determined via the impulse excitation technique, and can be associated with the thermal expansion coefficients of the constituent

materials. The core-skin structure of the copper-alumina composites is also a field of possible exploitation, i.e. a surface that is harder than the core, and a core that is tougher than the surface, provided the formation of a thick surface that allows its hardness evaluation. As for the W-Cu-Al_2O_3 composites, given their impact response and that three-phase composites have not been widely studied for their potential enhanced impact resistance, a range of properties may be researched, in addition to the further investigation of their activated toughening mechanisms.

Appendices

A ASTM International

E 1259

Standard Test Method for Dynamic Youngs Modulus, Shear Modulus, and Poissons Ratio for Advanced Ceramics by Impulse Excitation of Vibration.

This test method addresses the room temperature determination of dynamic moduli of elasticity of slender bars, cylindrical rods, and measures the fundamental resonant frequency of test specimens of suitable geometry by exciting them mechanically by a singular elastic strike with an impulse tool.

E 384

Standard Test Method for Microindentation Hardness of Materials.

This test method covers microindentation tests made with Vickers indenters under test forces in the range from 9.8×10^{-3} N to 9.8 N (1 to 1000 gf).

Microindentation tests permit hardness testing of specific phases or constituents and regions or gradients too small for evaluation by macroindentation tests. Low test forces also extend hardness testing to materials too thin or too small for macroindentation tests.

B Image Processing

ImageJ

ImageJ[1] has been used for particle counting and analysis of the optical micrographs. Fig. B.1 portrays the major steps of the process: (a) capturing the image and then transforming it to an 8-bit color image. (b) Converting the image to binary[2]. A threshold range[3] is set to distinguish the objects of interest (in our case metallic particles) from the background. (c) Outlining and numbering the detected objects. (Burger and Burge, 2016)

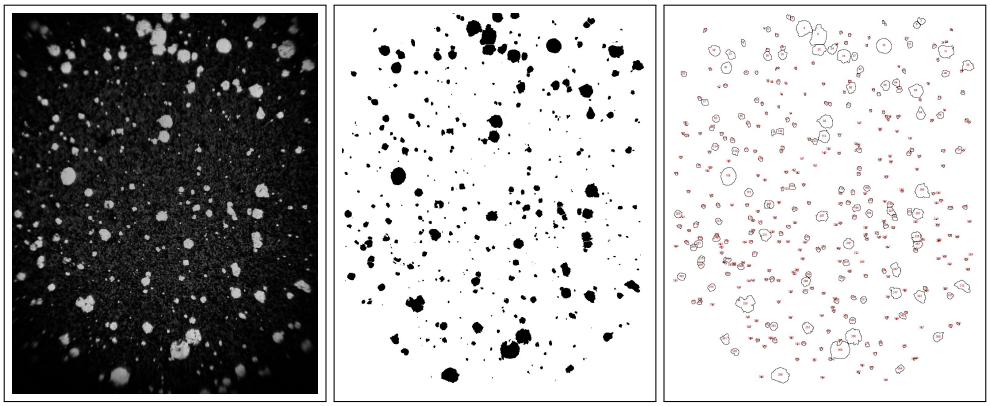

Figure B.1: A schematic of the image processing of the optical micrographs.

[1] An imaging system developed, maintained, and distributed by the National Institutes of Health (Schneider, Rasband, and Eliceiri, 2012).

[2] Binary images are a special type of intensity image where pixels can only take on one of two values, black or white.

[3] Thresholding an image is a special type of quantization that separates the pixel values in two classes, depending upon a given threshold value that is usually constant.

C Impulse Excitation Technique

IET measurements

A snapshot is provided in this section for the impulse excitation measurement performed on a 0.5 vol.% W/Al_2O_3 specimen. Fig. C.1 shows the vibration signal[1] (upper left), the frequency spectrum obtained via FFT[2] (upper right), the frequency value (lower right), and the elastic properties[3] (lower left).

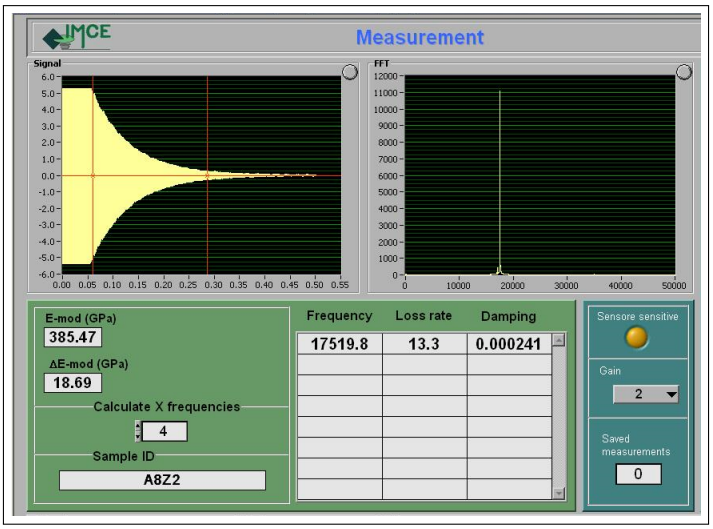

Figure C.1: A screen capture that demonstrates the IET measurement.

[1] Impulse response signal (amplitude as a function of time).

[2] A fast Fourier transform (FFT) is an algorithm that samples a signal over a period of time (or space) and divides it into its frequency components.

[3] The calculated Young's modulus value via Eq. 3.8 knowing the mass and dimensions of the given specimen.

D Elastic Modulus | Interface

Introduction

This section[1] reviews the elastic behaviour of metal particle-reinforced alumina ceramics. Experimental data available in the literature are compared with models that have been developed to predict the elastic modulus of composite materials. The study considers two approaches regarding the predictive models: models that are based on the properties of the constituents only, and models that acknowledge the existence of a third (inter)phase between the two phases. It is shown that the existence of an interphase with different elastic properties is necessary for the correct prediction of the elasticity of metal particle-reinforced ceramic matrix composites.

The elastic properties of a composite depend mainly on the properties of its components. In heterogeneous systems they depend also on the size, shape, aspect ratio and orientation of the phases, and on the nature of the interface. The degree of adhesion between the phases may play a role, as it affects the stress transfer through the interfaces. Further, the presence of one phase may influence the structure and the properties of the other, at least in areas near the interfaces. In the case of composites, where a ceramic phase has been produced by firing and sintering in situ, the process may also influence the properties of the other phases. Thus, a general model describing the behaviour or a heterogeneous ceramic based composite should take into account all these aspects.

Two different types of models that predict the elastic behaviour of two-component ceramic matrix composites are considered in this study. The first includes the classical "two-phase" models (a matrix reinforced with a filler). These models neglect interfacial phenomena and their critical aspect is the correct choice for the values of the properties of the components. For ceramic matrix composites, these values may be different in the composite from the ones in material property tables or measured for the neat materials.

[1] Based on a manuscript to be submitted for publication

The second type includes the "three-phase" models, where the third phase is the matrix material around the interface. This phase will have different properties from that of the bulk of the matrix, as it is influenced by the presence of the inclusions and the firing process. Here the properties in the bulk (far form the interface) are considered for each component to be the same as in the neat material.

The 2-phase models cannot fit the data

We have discussed in section 2.5.2 that, in several cases in the literature, the 2-phase models cannot describe the change of the modulus of the ceramic upon addition of the (softer) reinforcing phase. Some of the factors that can cause the discrepancy between the predictions of these models and the experimental data are summarised here:

1. The overall properties of the matrix in the composite may be different from the ones of the pure matrix because the reinforcement alters them by affecting the sintering process.

   The change of the overall matrix properties due to the effect of the inclusions on the sintering process does not seem plausible in composites with low fraction of micron-sized particles. It should take place only in the vicinity of the particles.

2. The sintering process can affect the properties of the metal inclusions.

   With the exception of cases, in which the sintering process prevents the crystallisation of the material in the inclusions, the process cannot affect much the mechanical properties of the metallic particles. Suppression of the crystallinity of the metal is highly unlikely in these processes and, even if it takes place, its contribution to decreasing the modulus of the composites is very small in samples of low volume fraction of particles.

3. The adhesion between the phases may be inadequate.

   Voids may exist between the matrix and the metal inclusion, possibly due to differences of the thermal expansion coefficients and the degree of shrinkage during crystallisation. If these are significant their volume should be deducted from the measured density of the composite.

4. The presence of the particles can alter the properties of the matrix locally – around the interface, mainly during the sintering process. In this case there may finally be three phases with distinct properties in the composite: i) the metal inclusions; (ii) the ceramic matrix in the

bulk; and (iii) the ceramic matrix close to the interfaces surrounding the metal particles.

The last case leads us to examine another set of models that take into account the possible existence of the third phase.

“Three-phase" models

The models discussed in section 2.2.1.2 assume a zero-thickness interfacial region and sufficient interfacial adhesion between the inclusions and the matrix. The existence of an interfacial region between the constituents, however, could affect the mechanical properties of the composite.

Strong adhesion between the ceramic matrix and the metal inclusions justifies the assumptions of affine deformation and full stress transfer between the phases. The data that fall between the curves of the parallel and the series models could satisfy this. The elastic properties of composites that show weak adhesion between the phases or have softer interfacial region of non-zero thickness cannot be predicted by these models.

The concept of the interphase region that was introduced in the previous section may account for the data that fall outside the physical bounds of the 2-phase models. The interphase region is part of the matrix, surrounds the dispersed particles, and is considered to have different physical and mechanical properties from the bulk of the matrix. It is a third, discreet phase in the composite, with volume fraction V_i and modulus of elasticity E_i. Thus, $V_f + V_{mb} + V_i = 1$, where the subscript $_{mb}$ corresponds to the bulk (away from the interphase) of the matrix.

The amount of material in the interphase region depends on the interfacial area and the thickness of this region. The interfacial area is a function of the volume fraction of the reinforcing particles and their size: for a given volume fraction the smaller the particles, the higher their numbers and the larger the total interfacial area. Thus, the contribution of the interphase to the elastic properties of the composites increases when the size of the reinforcing particles decreases, especially in the nanometer region.

In the following we present some “3-phase” models, schematically shown in Fig. D.1, that describe the modulus of elasticity of particle-reinforced composites, where a third phase (inter-phase, consisting of matrix material with different properties, e.g. porosity or crystallinity) surrounds the reinforcing particles. These models were developed originally for composites with $\delta > 1$ and have been adjusted here to apply for ceramic-matrix composites, where $\delta < 1$. The models fall into two types.

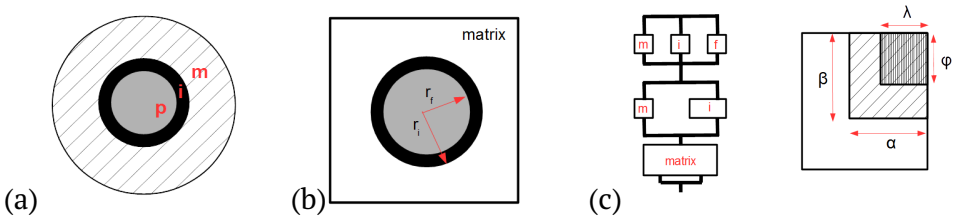

Figure D.1: 3-phase models: (a) Three concentric spheres showing the particle (r_f) surrounded by the inter-phase (r_i) surrounded, in turn, by the matrix, (b) Spherical particle, surrounded by the interphase, inside a cubic matrix cell; (c) Modified model of Takayanagi including the inter-phase; the parameters α and β determine the third constituent, i.e. the interphase region.

The first type of these models assumes a composite consisting of three phases arranged as either three concentric spheres, Fig. D.1a, or as spherical particles surrounded by a concentric cell of the interphase region inside a cube of the matrix, Fig. D.1b. In all cases $V_f + V_m + V_i = 1$. The volume fraction of the interphase, V_i ($< 1 - V_f$), is:

$$V_i = V_f \left[\left(\frac{r_i}{r_f} \right)^3 - 1 \right] \qquad \Leftrightarrow \qquad r_i = r_f \sqrt[3]{1 + \frac{V_i}{V_f}} \tag{A.1}$$

The limit for the equivalent radius of the interphase regions is $r_i < d_s/2$, where d_s is the average distance between the centers of the particles. Eq. A.1 gives another limit: $r_i < r_f V_f^{-1/3}$.

The elastic modulus of the interphase, $E_i(r)$, depends on the diameter of the particles and varies between the modulus at $r = r_f$ and that of the matrix at $r = r_i$. The modulus $E_i(r_f)$ should be lower than the modulus of the matrix but independent of that of the metal. The form of $E_i(r)$ should reflect the physics that is responsible for the reduction of the matrix modulus in the interfacial region.

The several models of this type differ in the form of $E_i(r)$ for $r_f < r < r_i$. The ones proposed by (Spathis, Sideridis, and Theocaris, 1981; Sideridis, 1986; Sideridis, Theocaris, and Papanicolaou, 1986) assume linear, hyperbolic, logarithmic, and parabolic functions and are shown in Fig. D.2a for indicative values of $E_i(r_f)$, E_m, r_f and r_i. The model of (Saeed and Akbar, 2007), adjusted for ceramic-matrix composites, results in the following form for $E_i(r)$:

$$E_i(r) = E_{fi} + \left(\frac{r - r_f}{r_i - r_f} \right)^{n/2} \left(E_m - E_{fi} \right) \ . \tag{A.2}$$

Here $E_{if} = E_i(r_f)$ and n is a dimensionless interfacial enhancement index,

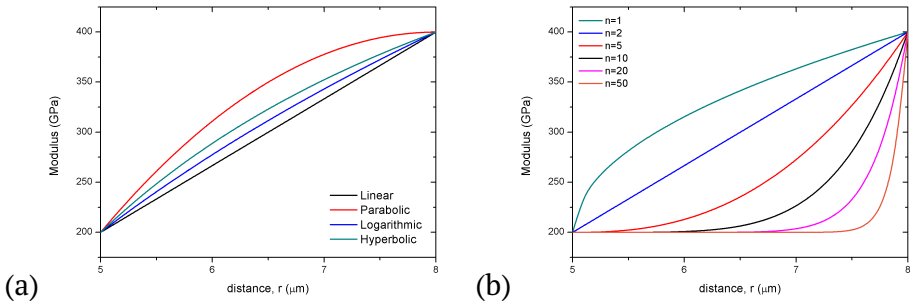

Figure D.2: The elasticity modulus in the interfacial region; $r_f = 5$, $r_i = 8$ μm; E_m = 400 GPa and E_{fi} = 200 GPa: (a) for linear, parabolic, logarithmic and hyperbolic curves; (b) for several values of the exponent n of eq. A.2.

which gives the rate of the decrease (form of the curve) of the modulus in the interphase region. Its value depends on the properties of the matrix and the filler, the surface treatment of the particles, and the degree of dispersion in the composite. E_{fi}, n and r_i depend on the type of the ceramic and its structure around the interface. Thus, the parameters should eventually depend on the sintering process used for the manufacturing of the composite. Curves of $E_i(r)$ for several values of the exponent n are shown in Fig. D.2b.

The elastic modulus of the composite material for these models can be determined by adding the contributions of each phase using modified parallel or series models:

$$E_c = E_f V_f k + E_m(1 - V_f - V_i) + \bar{E}_i V_i \,, \tag{A.3}$$

$$E_c = \left(\frac{1}{k} \frac{V_f}{E_f} + \frac{1 - V_f - V_i}{E_m} + \frac{V_i}{\bar{E}_i} \right)^{-1} . \tag{A.4}$$

where $\bar{E}_i$ is the average of $E_i(r)$ in the interphase: $\bar{E}_i = \int_{r_f}^{r_i} E_i(r)\, dr \,/\, (r_i - r_f)$. The correction parameter, $k \leq 1$, describes the degree of adhesion between matrix and particles and depends on the particle diameter. k should have a value close to 1. Given the shape of the inclusions in a ceramic matrix composite, the series model seems more appropriate.

The second type of 3-phase models (Ling et al., 2002) is based on the Takayanagi model. It includes the parameters λ and ϕ to describe the spatial distribution of the dispersed phase and it incorporates also the parameters α and β to describe the interphase (Fig. D.1c):

$$\frac{E_c}{E_m} = \left[1 - \beta + \frac{\beta - \lambda}{1 - \alpha + \alpha(c-1)/\ln c} + \frac{\phi}{1 - \alpha + (\alpha - \lambda)(c+1)/2 + \lambda\delta} \right]^{-1} , \tag{A.5}$$

where $c = E_{fi}/E_m$. The value of E_i in this model varies linearly between a low

value at the surface of the particle, and E_m at the other end of this region. The value of c has to be estimated from the details of the process that produced the ceramic.

A simplification of the model for spherical inclusions has $\phi = \lambda = \sqrt{V_f}$, and $\alpha = \beta = \sqrt{(1+\tau/r_f)^3 V_f}$.

Fitting of experimental data

The three-phase models described here were originally developed for nanocomposites, where the reinforcement phase was used to enhance the stiffness of the matrix and $E_f >> E_m$. However, the idea that the interphase region may have different properties from those of the matrix can also be applicable in ceramic matrix composites, where $E_f < E_m$. The equations given in the previous section have been adjusted from the original papers to conform with this difference.

The fitting of the experimental data with the models depends on the choice of the values of their parameters: E_{fi}, V_i, k, r_i, n, c and/or τ. The variables E_f, E_m, V_f and r_f are properties of the components. The data of the Ni/alumina composites (Tuan and Chen, 2002) were chosen for the comparison because their particle size and porosity have been reported, and are used here to correct the properties of the matrix. Fig. D.3 shows that successful fitting of the data is possible for many combinations of its parameters.

In general, the lower the average value of the modulus at the interface, $\bar{E}_i$, the lower the amount of matrix material (V_i) that needs to be situated in this area. The parameter k, which gives the degree of discontinuity of the stress around the metal/ceramic interface in the first type of models corresponds to voids at the interface, possibly resulting from the greater shrinkage of the metallic inclusion than the ceramic matrix. This effect is small and k should not have values lower than 0.8-0.9. For these values of k, the parallel formulation, eq. A.3 (Fig. D.3a) would require an unrealistically high amount of interphase material or a very low value of its modulus to fit the data. The series formulation, eq. A.5 (Fig. D.3b,c), on the other hand, seems to better describe the data, allowing lower values to be assigned for V_i and reasonable values of k and E_{fi}. Then, it is sufficient to set, e.g., $V_i = 5V_f$ (or $r_i = 1.82r_f$ according to eq. A.1), $\bar{E}_i$ = 300 GPa and $k = 0.8$ to describe the data adequately (Fig. D.3c). Table D.1 shows the values of the parameters of the several models to obtain this average value for $E_i(r)$ between r_f and r_i. Obviously, the best model of the first type that can fit this set of experimental data using reasonable values of its parameters is given by eq. A.2 in combination with eq. A.4.

Table D.1: Best values of the parameters of the "3-phase" models which are needed to obtain the fitting curve in Fig. D.3c ($\bar{E}_i = 300$ GPa) and Fig. D.3d.

model	form of $E_i(r)$	Parameters E_{fi}/E_m	n	τ/r_f
Eq. A.4	parabolic	0.1	-	-
Eq. A.4	hyperbolic	0.32	-	-
Eq. A.4	logarithmic	0.44	-	-
Eq. A.4	linear	0.52	-	-
Eq. A.4	eq. A.2	0.17	1	-
Eq. A.4	eq. A.2	0.52	2	-
Eq. A.4	eq. A.2	0.68	4	-
Eq. A.4	eq. A.2	0.72	6	-
Eq. A.5		0.1	-	0.6
Eq. A.5		0.3	-	0.8
Eq. A.5		0.6	-	1.2

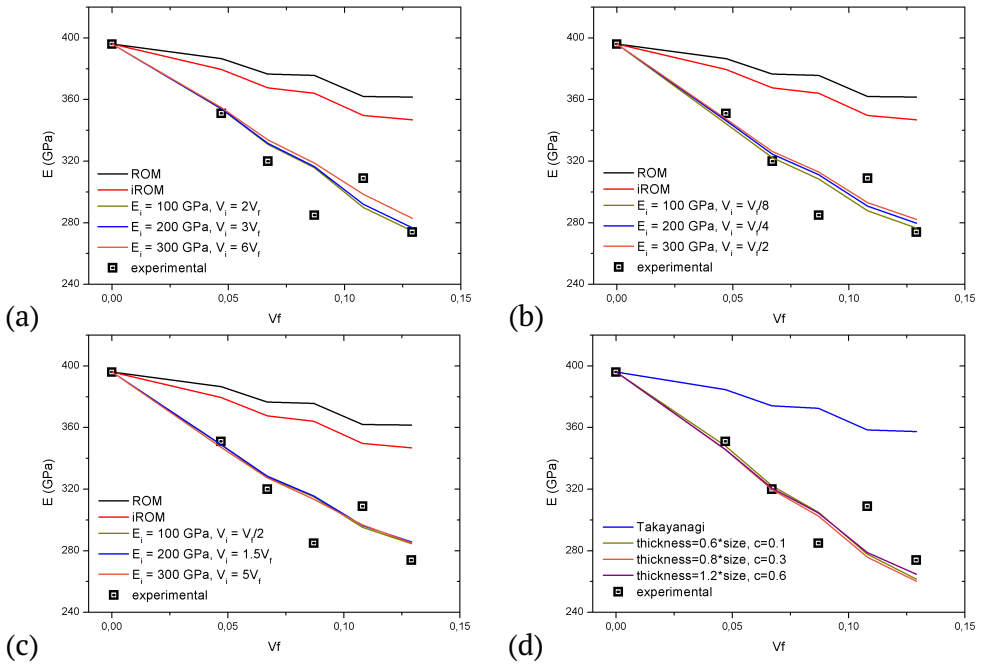

Figure D.3: Fits of elasticity modulus data for the Ni/alumina composites with: (a) eq. A.3 (k=0.5), (b) eq. A.4 (k=0.5), (c) eq. A.4 (k=0.8), (d) eq. A.5.

The fitting using the other type of models is shown in Fig. D.3d. Again, various combinations of c and τ can fit the data. It seems that low values of c or high values of τ are needed for the Ni/alumina composites. E.g. for c = 0.3, i.e., $E_{fi} = 0.3E_m$, the value of τ should be 0.8 times that of the particle size to fit the data. This means that $V_i \approx 5V_f$. As V_f = 13% in this case, then the volume fraction of the inter-phase exceeds 60% of the total.

For the Mo/alumina composites, where the data are not very far off the iROM, eq. A.5 can fit the data with $V_i = 1.2V_f$, $c = 0.5$ and $\tau/r_f = 0.3$ (Fig. D.4a). In that case Eq. A.4 also describes the data assuming a mean value of $\bar{E}_i = 350$ GPa and $V_i = 0.25V_f$, Fig. D.4b. Eq. A.5 also fits the data of the Ag/alumina composite with $c = 0.5$ and $V_i = 2.4V_f$, obviously better than the original Takayanagi ("2-phase") formulation (Fig. D.4c).

In summary, a variety of combinations can result in a satisfactory fitting of the available data by the "3-phase" models (Fig. D.3 and D.4). It is important, however, to assign such values to the variables that reflect the adhesion efficiency of the composite structure.

The remaining question relates to how low $\bar{E}_i$ or E_{fi} can be. The modulus of the ceramic depends the structure that is formed during the sintering process. Thus, the answer to this question should be sought in the examination of

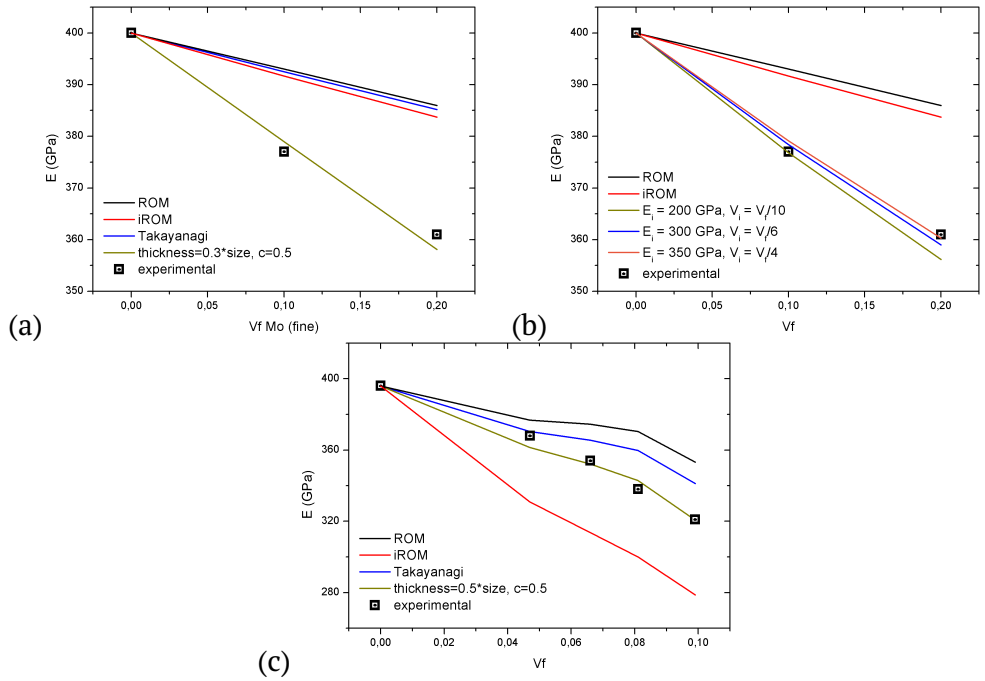

Figure D.4: Fit of the Mo/alumina composite data with: (a) eq. A.5, (b) eq. A.4 (k=0.8). (c) Ag/alumina and eq. A.5.

the physics of this process. I.e., of how the presence of the metal inclusions affects the diffusion of the ceramic material in their vicinity. This will affect the changes in grain size in the ceramic and the local porosity. If confined areas are formed, the local crystallinity may also be affected. A high volume fraction of matrix porosity concentrated in the interfacial region and/or small matrix grain sizes that favor the contribution of grain boundaries in the same area could contribute to the low values of E_i.

For example to fit the elastic modulus of the composite of 10.8 vol% Ni in alumina matrix with the series model of eq. A.4 (Fig. D.3b); E_i = 0.75E_m = 300 GPa, and $V_i = V_f/2$ = 5.4%. That is, around each metal particle there is a region of matrix with $\sqrt[3]{3}r_i$ thickness and an average modulus of 75% of that of the bulk matrix. The lower value of the modulus there could be due to higher porosity locally. Since the total porosity of the matrix was measured to be 2.1%, the porosity of the interphase region should be 13.6% to justify the value of the modulus there and the rest of the matrix (V_m = 0.838) should have 1.6% porosity to justify the global measured value of 2.1%. Similarly, for a total porosity of 1% and V_f = 6.7%, the porosity of the interphase region should be again 13.6% to justify the value of the modulus there (E_i = 300 GPa) and the rest of the matrix (V_m = 0.8995) should only have 0.6% porosity.

Conclusions

The dispersion of ductile metallic inclusions in the brittle alumina matrix results in enhanced fracture toughness values, yet diminishes those of elasticity. According to published experimental data the elastic moduli values of some metal/alumina are sometimes even lower than the predictions of simple mixing rules. Based on this observation the concept of a third phase is introduced. An interfacial region with non zero thickness that surrounds the dispersed particles in the matrix could affect the mechanical behavior of the composite structure. The existence of a third phase between the two constituent materials could result in stresses that are transferred irregularly. This assumption can relate to the poor bonding between the alumina matrix and the metallic particles reported in several studies. The fitting of the "three-phase" models highly depends on the choice of the variables included in the equations and these should reflect the adhesion quality of the composite. Assigning realistic and physically meaningful values to all model parameters is critical.

Other characteristics such as the matrix porosity and grain size are found to slightly reduce the elastic modulus of the matrix, and thus lower the total modulus values. The effect of additional parameters including the size and shape of particles and their possible melting during the sintering process, the effect of the processing route/conditions such as temperature, is still under investigation.

In metal/ceramic composites, where the components differ significantly in terms of physical and mechanical properties, the accurate prediction of Young's modulus requires complicated models. Future work should involve the verification of the "third-phase" assumption with better characterised experimental data and the establishment of its origin and its properties in the ceramic sintering process.

Bibliography

Ahmed, S. and F. R. Jones (1990). "A review of particulate reinforcement theories for polymer composites". In: *Journal of Materials Science* 25.12, pp. 4933–4942.

Aldrich, D.E. and M.J. Edirisinghe (1998). "Addition of copper particles to an alumina matrix". In: *Journal of Materials Science Letters* 17.12, pp. 965–967.

Aldridge, M and J.A Yeomans (1999). "The thermal shock behaviour of ductile particle toughened alumina composites". In: *Journal of the European Ceramic Society* 19.9, pp. 1769 –1775.

American Mineralogist Crystal Structure Database. http://rruff.geo.arizona.edu/AMS/amcsd.php. [Online; accessed 2018].

Ashby, M.F. (1989). "Overview No. 80: On the engineering properties of materials". In: *Acta Metallurgica* 37.5, pp. 1273 –1293.

Ashby, M.F (1993). "Criteria for selecting the components of composites". In: *Acta Metallurgica et Materialia* 41.5, pp. 1313 –1335.

Ashby, M.F., F.J. Blunt, and M. Bannister (1989). "Flow characteristics of highly constrained metal wires". In: *Acta Metallurgica* 37.7, pp. 1847 –1857.

Azar, M. et al. (2008). "Effect of initial particle packing on the sintering of nanostructured transition alumina". In: *Journal of the European Ceramic Society* 28.6, pp. 1121 –1128.

Bao, G. and Hui Chung-Yuen (1990). "Effects of interface debonding on the toughness of ductile-particle reinforced ceramics". In: *International Journal of Solids and Structures* 26.5, pp. 631 –642.

Barsoum, M. and M.W. Barsoum (2002). *Fundamentals of Ceramics*. Series in Material Science and Engineering. Taylor & Francis.

Basista, M. and W. Wglewski (2006). "Modelling of damage and fracture in ceramic matrix composites an overview". In: *Journal of Theoretical and Applied Mechanics* 44.3.

Basu, B. and K. Balani (2011). *Advanced Structural Ceramics*. Wiley.

Beatty, R. (2001). *Copper*. Elements (Benchmark Books). Benchmark Books.

Becher, P.F. (1991). "Microstructural Design of Toughened Ceramics". In: *Journal of the American Ceramic Society* 74.2, pp. 255–269.

Breval, E. and C. G. Pantano (1992). "Sol-gel prepared Ni-alumina composite materials". In: *Journal of Materials Science* 27.20, pp. 5463–5469.

Breval, E. et al. (1992). "Sol-gel prepared Ni-alumina composite materials". In: *Journal of Materials Science* 27.6, pp. 1464–1468.

Broniszewski, K. et al. (2013). "Al_2O_3-Mo cutting tools for machining hardened stainless steel". In: *Wear* 303.1, pp. 87 –91.

Budiansky, B., J.C. Amazigo, and A.G. Evans (1988). "Small-scale crack bridging and the fracture toughness of particulate-reinforced ceramics". In: *Journal of the Mechanics and Physics of Solids* 36.2, pp. 167 –187.

Burger, W. and M.J. Burge (2016). *Digital Image Processing: An Algorithmic Introduction Using Java*. Texts in Computer Science. Springer London.

Cahill, J.A. and A.D. Kirshenbaum (June 1962). "The density of liquid copper from its melting point (1356 °K.) to 2500 °K. and an estimate of its critical constants". In: *Journal of Physical Chemistry (U.S.)* 66, pp. 1080–1082.

Callister, W.D. and D.G. Rethwisch (2009). *Materials Science and Engineering: An Introduction, 8th Edition*. Wiley.

Cardarelli, F. (2008). *Materials Handbook: A Concise Desktop Reference*. Springer London.

Carter, C.B. and M.G. Norton (2007). *Ceramic Materials: Science and Engineering*. Springer ebook collection / Chemistry and Materials Science 2005-2008. Springer New York.

Chakraborty, A. et al. (2000). "Effect of $MoSi_2$ and Nb reinforcements on mechanical properties of Al_2O_3 matrix composites". In: *Journal of Materials Science* 35.15, pp. 3827–3835.

Chakraborty, A. et al. (2009). "An effort to fabricate and characterize in-situ formed graded structure in a ceramic-metal system". In: *Journal of Materials Processing Technology* 209.5, pp. 2681 –2692.

Chawla, K.K. (2013a). *Ceramic Matrix Composites*. Springer US.

Chawla, K.K (2013b). *Composite Materials: Science and Engineering*. Materials Research and Engineering. Springer New York.

Chen, R.Z. and W.H. Tuan (1999). "Pressureless Sintering of Al_2O_3/Ni Nanocomposites". In: *Journal of the European Ceramic Society* 19.4, pp. 463 –468.

Chou, W.B. and W.H. Tuan (1995). "Toughening and strengthening of alumina with silver inclusions". In: *Journal of the European Ceramic Society* 15.4, pp. 291 –295.

Coble, R. L. and W. D. Kingery (1956). "Effect of porosity on physical properties of sintered alumina". In: *Journal of the American Ceramic Society* 39.11, pp. 377–385.

Counto, U.J. (1964). "The effect of the elastic modulus of the aggregate on the elastic modulus, creep and creep recovery of concrete". In: *Magazine of Concrete Research* 16.48, pp. 129–138.

Davidge, R.W. and T.J. Green (1968). "The strength of two-phase ceramic/-glass materials". In: *Journal of Materials Science* 3.6, pp. 629–634.

Davis, J.R. (2001). *Copper and Copper Alloys*. ASM specialty handbook. ASM International.

Deng, Z-Y. et al. (2004). "Reinforcement by crack-tip blunting in porous ceramics". In: *Journal of the European Ceramic Society* 24.7, pp. 2055 –2059.

Dewey, J.M. (1947). "The Elastic Constants of Materials Loaded with NonRigid Fillers". In: *Journal of Applied Physics* 18.6, pp. 578–581.

Diaz, L.A et al. (2003). "Alumina/molybdenum nanocomposites obtained in organic media". In: *Journal of the European Ceramic Society* 23.15. Ceramic and Metal Interfaces, pp. 2829 –2834.

Donald, I. W. and P. W. McMillan (1976). "Ceramic-matrix composites". In: *Journal of Materials Science* 11.5, pp. 949–972.

Dutta, A.K., A.B. Chattopadhyaya, and K.K. Ray (2006). "Progressive flank wear and machining performance of silver toughened alumina cutting tool inserts". In: *Wear* 261.7, pp. 885 –895.

Dutta, A.K. et al. (2001). "The load dependence of hardness in aluminasilver composites". In: *Ceramics International* 27.4, pp. 407 –413.

E 1876-15, ASTM International (2015). *Standard Test Method for Dynamic Young's Modulus, Shear Modulus, and Poisson's Ratio by Impulse Excitation of Vibration*. Tech. rep. ASTM International, West Conshohocken, PA.

E 384-17, ASTM International (2017). *Standard Test Method for Microindentation Hardness of Materials*. Tech. rep. ASTM International, West Conshohocken, PA.

Evans, A.G. (1990). “Perspective on the Development of High-Toughness Ceramics”. In: *Journal of the American Ceramic Society* 73.2, pp. 187–206.

Evans, A.G. and K.T. Faber (1981). “Toughening of Ceramics by Circumferential Microcracking”. In: *Journal of the American Ceramic Society* 64.7, pp. 394–398.

Evans, A.G. and Y. Fu (1985). “Some effects of microcracks on the mechanical properties of brittle solids-II. Microcrack toughening”. In: *Acta Metallurgica* 33.8, pp. 1525 –1531.

Evans, A.G. and R.M. McMeeking (1986). “On the toughening of ceramics by strong reinforcements”. In: *Acta Metallurgica* 34.12, pp. 2435 –2441.

Faber, K.T. and A.G Evans (1983a). “Crack deflection processes - I. Theory”. In: *Acta Metallurgica* 31.4, pp. 565 –576.

Faber, K.T. and A.G. Evans (1983b). “Crack deflection processes - II. Experiment”. In: *Acta Metallurgica* 31.4, pp. 577 –584.

Fahrenholtz, W.G., D.T. Ellerby, and R.E. Loehman (2000). “Al_2O_3-Ni Composites with High Strength and Fracture Toughness”. In: *Journal of the American Ceramic Society* 83.5, pp. 1279–1280.

Fu, Shao-Yun et al. (2008). “Effects of particle size, particle/matrix interface adhesion and particle loading on mechanical properties of particulatepolymer composites”. In: *Composites Part B: Engineering* 39.6, pp. 933 –961.

Gao, F. and Tianming Wang (1990). “Apparent fracture energy of brittle materials by branching of crack and microcrack”. In: *Journal of Materials Science Letters* 9.12, pp. 1409–1411.

German, R. (2014). *Sintering: From Empirical Observations to Scientific Principles*. Elsevier Science.

German, R.M. (Oct. 1987). “Theory of thermal debinding”. In: *International Journal of Powder Metallurgy* 23, pp. 237–245.

Giannakopoulos, A.E. and K. Breder (1991). “Synergism of Toughening Mechanisms in WhiskerReinforced CeramicMatrix Composites”. In: *Journal of the American Ceramic Society* 74.1, pp. 194–202.

Gibson, L.J. and M.F. Ashby (July 1982). “The Mechanics of Three-Dimensional Cellular Materials”. In: *Proceedings of the Royal Society of London A: Mathematical, Physical and Engineering Sciences* 382.1782, pp. 43–59.

Gizowska, M., K. Konopka, and M. Szafran (2011). “Properties of Water-Based Slurries for Fabrication of Ceramic-Metal Composites by Slip Casting Method”. In: vol. 56. 4, p. 1105.

Green, D.J. (1983). "Fracture Toughness Predictions for Crack Bowing in Brittle Particulate Composites". In: *Journal of the American Ceramic Society* 66.1, pp. C–4–C–5.

Green, D.J (1998). *An Introduction to the Mechanical Properties of Ceramics*. Cambridge Solid State Science Series. Cambridge University Press.

Guichard, J.L., O. Tillement, and A. Mocellin (1998). "Alumina-chromium cermets by hot-pressing of nanocomposite powders". In: *Journal of the European Ceramic Society* 18.12, pp. 1743 –1752.

Halpin, J.C. (1969). "Stiffness and Expansion Estimates for Oriented Short Fiber Composites". In: *Journal of Composite Materials* 3.4, pp. 732–734.

Hashin, Z. and S. Shtrikman (1963). "A variational approach to the theory of the elastic behaviour of multiphase materials". In: *Journal of the Mechanics and Physics of Solids* 11.2, pp. 127 –140.

Hill, R. (1952). "The Elastic Behaviour of a Crystalline Aggregate". In: *Proceedings of the Physical Society. Section A* 65.5, p. 349.

Hill., R (1963). "Elastic properties of reinforced solids: Some theoretical principles". In: *Journal of the Mechanics and Physics of Solids* 11.5, pp. 357 –372.

Hirsch, T.J. (1962). "Modulus of Elasticity of Concrete Affected by Elastic Moduli of Cement Paste Matrix and Aggregate". In: *ACI Journal Proceedings* 59.3, pp. 427–452.

Hosford, W.F. (2010). *Mechanical Behavior of Materials*. Cambridge University Press.

Hutchinson, J.W. (1987). "Crack tip shielding by micro-cracking in brittle solids". In: *Acta Metallurgica* 35.7, pp. 1605 –1619.

Ighodaro, O.L. and O.I. Okoli (2008). "Fracture Toughness Enhancement for Alumina Systems: A Review". In: *International Journal of Applied Ceramic Technology* 5.3, pp. 313–323.

IMCE NV. http://www.imce.eu. [Online; accessed 2018].

Ishai, O. and L.J. Cohen (1967). "Elastic properties of filled and porous epoxy composites". In: *International Journal of Mechanical Sciences* 9.8, pp. 539 –546.

Ji, Y. and J. A. Yeomans (2002a). "Microstructure and mechanical properties of chromium and chromium/nickel particulate reinforced alumina ceramics". In: *Journal of Materials Science* 37.24, pp. 5229–5236.

Ji, Y. and J.A. Yeomans (2002b). “Processing and mechanical properties of $Al_2O_3$5 vol.% Cr nanocomposites”. In: *Journal of the European Ceramic Society* 22.12, pp. 1927 –1936.

Johnson, J.L., J.J. Brezovsky, and R.M. German (2005). “Effects of tungsten particle size and copper content on densification of liquid-phase-sintered W-Cu”. In: *Metallurgical and Materials Transactions A* 36.10, pp. 2807–2814.

Kafkaslolu, B. and Yahya Kemal Tür (2016). “Pressureless sintering of Al_2O_3/Ni nanocomposites produced by heterogeneous precipitation method with varying nickel contents”. In: *International Journal of Refractory Metals and Hard Materials* 57, pp. 139 –144.

Kang, S.J.L. (2004). *Sintering: Densification, Grain Growth and Microstructure*. Elsevier Science.

Katayama, Tomoyuki et al. (2011). “Fabrication of Al_2O_3-W Functionally Graded Materials by Slip-casting Method”. In: *IOP Conference Series: Materials Science and Engineering* 18.20, p. 202023.

Khaund, A.K., V.D. Krstic, and P.S. Nicholson (1977). “Influence of elastic and thermal mismatch on the local crack-driving force in brittle composites”. In: *Journal of Materials Science* 12.11, pp. 2269–2273.

Kim, J-C. and I-H. Moon (1998). “Sintering of nanostructured W-Cu alloys prepared by mechanical alloying”. In: *Nanostructured Materials* 10.2, pp. 283 –290.

Konopka, K., M. Maj, and K.J. Kurzydowski (2003). “Studies of the effect of metal particles on the fracture toughness of ceramic matrix composites”. In: *Materials Characterization* 51.5, pp. 335 –340.

Konopka, K. and A. Oziebo (2001). “Microstructure and the fracture toughness of the Al_2O_3-Fe composites”. In: *Materials Characterization* 46.2. STERMAT 2000: Stereology and Image Analysis in Materials Science, pp. 125 –129.

Krstic, V., P.S. Nicholson, and R.G. Hoagland (1981). “Toughening of Glasses by Metallic Particles”. In: *Journal of the American Ceramic Society* 64.9, pp. 499–504.

Krstic, V.D. (1983). “On the fracture of brittle-matrix/ductile-particle composites”. In: *Philosophical Magazine A* 48.5, pp. 695–708.

Kwon, Sung-Tae et al. (1987). “Effect of Sintering Temperature on the Densification of Al_2O_3”. In: *Journal of the American Ceramic Society* 70.4, pp. C–69–C–70.

Lane, S.M., S.B. Biner, and O. Buck (1998). "Room temperature fracture and high temperature creep characteristics of 20 vol.% Nb particulate reinforced alumina". In: *Materials Science and Engineering: A* 246.1, pp. 244 –251.

Lassner, E. and W.D. Schubert (1999). *Tungsten: Properties, Chemistry, Technology of the Elements, Alloys, and Chemical Compounds*. Springer US.

Lee, W.E. and M. Rainforth (1994). *Ceramic Microstructures: Property control by processing*. Springer Netherlands.

Levin, I. and D. Brandon (1998). "Metastable Alumina Polymorphs: Crystal Structures and Transition Sequences". In: *Journal of the American Ceramic Society* 81.8, pp. 1995–2012.

Lewis, T.B. and L.E. Nielsen (1970). "Dynamic mechanical properties of particulatefilled composites". In: *Journal of Applied Polymer Science* 14.6, pp. 1449–1471.

Li, Guo-Jun, Xiao-Xian Huang, and Jing-Kun Guo (2003). "Fabrication, microstructure and mechanical properties of Al_2O_3/Ni nanocomposites by a chemical method". In: *Materials Research Bulletin* 38.11, pp. 1591 –1600.

Li, Y. and M Zhou (2013a). "Prediction of fracture toughness of ceramic composites as function of microstructure: I. Numerical simulations". In: *Journal of the Mechanics and Physics of Solids* 61.2, pp. 472 –488.

Li, Y. and M. Zhou (2013b). "Prediction of fracture toughness of ceramic composites as function of microstructure: II. analytical model". In: *Journal of the Mechanics and Physics of Solids* 61.2, pp. 489 –503.

Lieberthal, M. and W.D. Kaplan (2001). "Processing and properties of Al_2O_3 nanocomposites reinforced with sub-micron Ni and $NiAl_2O_4$". In: *Materials Science and Engineering: A* 302.1, pp. 83 –91.

Ling, Ji Xiang et al. (2002). "Tensile modulus of polymer nanocomposites". In: *Polymer Engineering & Science* 42.5, pp. 983–993.

Loehman, R.E. (2010). *Characterization of Ceramics*. Material Characterization Series: Surfaces, Interfaces and Thin Films. Momentum Press.

Low, I.M. (2018). *Advances in Ceramic Matrix Composites*. Woodhead Publishing Series in Composites Science and Engineering. Elsevier Science.

Lu, Jinshan et al. (2000). "Effect of nickel content on the sintering behavior, mechanical and dielectric properties of Al_2O_3/Ni composites from coated powders". In: *Materials Science and Engineering: A* 293.1, pp. 223 –228.

Lucchini, E., S. Lo Casto, and O. Sbaizero (2003). "The performance of molybdenum toughened alumina cutting tools in turning a particulate metal matrix composite". In: *Materials Science and Engineering: A* 357.1, pp. 369 –375.

Mackenzie, J.K. (1950). "The Elastic Constants of a Solid containing Spherical Holes". In: *Proceedings of the Physical Society (London)* B 63.1, pp. 2–11.

Mitchell, B.S. (2004). *An Introduction to Materials Engineering and Science for Chemical and Materials Engineers*. Wiley.

Mouritz, A.P. (2012). *Introduction to Aerospace Materials*. Woodhead Publishing in Materials. Elsevier Science.

Moya, J.S., S. Lopez-Esteban, and C. Pecharromán (2007). "The challenge of ceramic/metal microcomposites and nanocomposites". In: *Progress in Materials Science* 52.7, pp. 1017 –1090.

Munro, M. (1997). "Evaluated Material Properties for a Sintered alpha-Alumina". In: *Journal of the American Ceramic Society* 80.8, pp. 1919–1928.

Nawa, M., T. Sekino, and K. Niihara (1994). "Fabrication and mechanical behaviour of Al_2O_3/Mo nanocomposites". In: *Journal of Materials Science* 29.12, pp. 3185–3192.

Nikolopoulos, P. and S. Agathopoulos (1992). "Interfacial phenomena in Al_2O_3-liquid metal and Al_2O_3-liquid alloy systems". In: *Journal of the European Ceramic Society* 10.6, pp. 415 –424.

Oh, S-T., T. Sekino, and K. Niihara (1998). "Fabrication and mechanical properties of 5 vol% copper dispersed alumina nanocomposite". In: *Journal of the European Ceramic Society* 18.1, pp. 31 –37.

Oh, S-T. et al. (May 2001). "Fabrication of Cu dispersed Al_2O_3 nanocomposites using Al_2O_3/CuO and Al_2O_3/Cu-nitrate mixtures". In: 44.

Oziębło, A. et al. (Dec. 2004). "Al_2O_3-Fe Functionally Graded Materials Fabricated under Magnetic Field". In: *Bulk and Graded Nanometals*. Vol. 101. Solid State Phenomena. Trans Tech Publications, pp. 143–146.

Ozieblo, A. et al. (Apr. 2005). "Microstructure of Al_2O_3-Fe FGM Obtained by Modified Slip-Casting Method". In: *Functionally Graded Materials VIII*. Vol. 492. Materials Science Forum. Trans Tech Publications, pp. 665–672.

Pabst, W. and E. Gregorová (2003). "Note on the so-called Coble-Kingery formula for the effective tensile modulus of porous ceramics". In: *Journal of Materials Science Letters* 22.13, pp. 959–962.

Pabst, W. and E Gregorová (2004). “Mooney-type relation for the porosity dependence of the effective tensile modulus of ceramics”. In: *Journal of Materials Science* 39.9, pp. 3213–3215.

Pabst, W., G. Tichá, and E. Gregorová (2004). “Effective elastic properties of alumina-zirconia composite ceramics - Part 3. Calculation of elastic moduli of polycrystalline alumina and zirconia from monocrystal data”. In: *Ceramics - Silikaty* 48.2, pp. 41–48.

Pabst, W. et al. (2011). “Preparation and characterization of porous alumina-zirconia composite ceramics”. In: *Journal of the European Ceramic Society* 31.14, pp. 2721 –2731.

Pabst, W. et al. (2012). “Elastic properties and damping behavior of alumina-zirconia composites at room temperature”. In: *Ceramics International* 38.7, pp. 5931 –5939.

Paul, B. (1960). “Prediction of elastic constants of multiphase materials”. In: *Trans. Metall. Soc. AIME*, pp. 36–41.

Pelleg, J. (2014). “Mechanical Testing of Ceramics”. In: *Mechanical Properties of Ceramics*. Cham: Springer International Publishing.

Pines, M.L. and H.A. Bruck (2006). “Pressureless sintering of particle-reinforced metalceramic composites for functionally graded materials: Part I. Porosity reduction models”. In: *Acta Materialia* 54.6, pp. 1457 –1465.

Ponnusami, S.A., S. Turteltaub, and S. van der Zwaag (2015). “Cohesive-zone modelling of crack nucleation and propagation in particulate composites”. In: *Engineering Fracture Mechanics* 149, pp. 170 –190.

Portu, Goffredo de et al. (2007). “Wear behaviour of Al_2O_3-Mo and Al_2O_3-Nb composites”. In: *Wear* 262.11, pp. 1346 –1352.

Rahaman, M.N. (2003). *Ceramic Processing and Sintering*. Materials Engineering. Taylor & Francis.

Raj, R. and L.R. Thompson (1994). “Design of the microstructural scale for optimum toughening in metallic composites”. In: *Acta Metallurgica et Materialia* 42.12, pp. 4135 –4142.

Ravichandran, K.S. (1994). “Elastic Properties of Two-Phase Composites”. In: *Journal of the American Ceramic Society* 77.5, pp. 1178–1184.

Rödel, J. (1992). “Interaction between crack deflection and crack bridging”. In: *Journal of the European Ceramic Society* 10.3. Symposium on the Strengthening of Ceramic Materials, University of Hamburg-Harburg, pp. 143 –150.

Rice, R.W. (1989). "Relation of tensile strength-porosity effects in ceramics to porosity dependence of Young's modulus and fracture energy, porosity character and grain size". In: *Materials Science and Engineering: A* 112.Supplement C, pp. 215 –224.

Rice, R.W (1996). "Grain size and porosity dependence of ceramic fracture energy and toughness at 22 °C". In: *Journal of Materials Science* 31.8, pp. 1969–1983.

Richerson, D., D.W. Richerson, and W.E. Lee (2005). *Modern Ceramic Engineering: Properties, Processing, and Use in Design, Third Edition*. Materials Engineering. Taylor & Francis.

Rodríguez-Reinoso, F. et al. (1994). *Characterization of Porous Solids III*. Studies in Surface Science and Catalysis. Elsevier Science.

Rodriguez-Suarez, T. et al. (2009). "Alumina/tungsten nanocomposites obtained by Spark Plasma Sintering". In: *Composites Science and Technology* 69.14, pp. 2467 –2473.

Roesler, J., H. Harders, and M. Baeker (2007). *Mechanical Behaviour of Engineering Materials: Metals, Ceramics, Polymers, and Composites*. Springer Berlin Heidelberg.

Sadowski, T. and L. Marsavina (2011). "Multiscale modelling of two-phase Ceramic Matrix Composites". In: *Computational Materials Science* 50.4. Proceedings of the 19th International Workshop on Computational Mechanics of Materials, pp. 1336 –1346.

Saeed, SaberSamandari and AfaghiKhatibi Akbar (2007). "Evaluation of elastic modulus of polymer matrix nanocomposites". In: *Polymer Composites* 28.3, pp. 405–411.

Sbaizero, O and G Pezzotti (2000). "Influence of residual and bridging stresses on the R-curve behavior of Mo- and FeAl-toughened alumina". In: *Journal of the European Ceramic Society* 20.8, pp. 1145 –1152.

Sbaizero, O. and G. Pezzotti (2003). "Influence of molybdenum particles on thermal shock resistance of alumina matrix ceramics". In: *Materials Science and Engineering: A* 343.1, pp. 273 –281.

Sbaizero, O., G. Pezzotti, and T. Nishida (1998). "Fracture energy and R-curve behavior of Al_2O_3/Mo composites". In: *Acta Materialia* 46.2, pp. 681 –687.

Schneider, C.A., W.S. Rasband, and K.W. Eliceiri (2012). "NIH Image to ImageJ: 25 years of image analysis". In: *Nature Methods* 9, pp. 671–675.

Sekino, T., T. Nakajima, and K. Niihara (1996). "Mechanical and magnetic properties of nickel dispersed alumina-based nanocomposite". In: *Materials Letters* 29.1, pp. 165 –169.

Sekino, T and K. Niihara (1995). "Microstructural characteristics and mechanical properties for Al_2O_3/metal nanocomposities". In: *Nanostructured Materials* 6.5, pp. 663 –666.

Sekino, T. and K. Niihara (1997). "Fabrication and mechanical properties of fine-tungsten-dispersed alumina-based composites". In: *Journal of Materials Science* 32.15, pp. 3943–3949.

Selsing, J. (1961). "Internal Stresses in Ceramics". In: *Journal of the American Ceramic Society* 44.8, pp. 419–419.

Shabalin, I.L. (2014). *Ultra-High Temperature Materials I: Carbon (Graphene/-Graphite) and Refractory Metals*. Springer Netherlands.

Shackelford, J.F. and R.H. Doremus (2008). *Ceramic and Glass Materials: Structure, Properties and Processing*. Springer.

Sideridis, E. (1986). "The dynamic moduli of particulate-filled polymers as defined by the concept of interphase". In: *Composites Science and Technology* 27.4, pp. 305 –332.

Sideridis, E., P. S. Theocaris, and G. C. Papanicolaou (1986). "The elastic modulus of particulate composites using the concept of a mesophase". In: *Rheologica Acta* 25.4, pp. 350–358.

Sigl, L.S. et al. (1988). "On the toughness of brittle materials reinforced with a ductile phase". In: *Acta Metallurgica* 36.4, pp. 945 –953.

Simpson, L.A. and A. Wasylyshyn (1971). "Fracture Energy of Al_2O_3 Containing Mo Fibers". In: *Journal of the American Ceramic Society* 54.1, pp. 56–57.

Sánchez-Herencia, A.J., N. Hernández, and R. Moreno (2006). "Rheological Behavior and Slip Casting of Al_2O_3-Ni Aqueous Suspensions". In: *Journal of the American Ceramic Society* 89.6, pp. 1890–1896.

Somiya, S. et al. (2003). *Handbook of Advanced Ceramics: Materials, Applications, Processing and Properties*. Elsevier Science.

Spathis, G.D., E.P. Sideridis, and P.S. Theocaris (1981). "Adhesion efficiency and volume fraction of the boundary interphase in metal-filled epoxies". In: *International Journal of Adhesion and Adhesives* 1.4, pp. 195 –201.

Sun, Xudong and J. A. Yeomans (1996). "Microstructure and fracture toughness of nickel particle toughened alumina matrix composites". In: *Journal of Materials Science* 31.4, pp. 875–880.

Takayanagi, M., S. Uemura, and S. Minami (1964). "Application of equivalent model method to dynamic rheo-optical properties of crystalline polymer". In: *Journal of Polymer Science Part C: Polymer Symposia* 5.1, pp. 113–122.

Taya, Minoru et al. (1990). "Toughening of a Particulate-Reinforced Ceramic-Matrix Composite by Thermal Residual Stress". In: *Journal of the American Ceramic Society* 73.5, pp. 1382–1391.

Tirosh, J. and A.S. Tetelman (1976). "Fracture conditions of a crack approaching a disturbance". In: *International Journal of Fracture* 12.2, pp. 187–199.

Todd, I. and A.T. Sidambe (2013). *Advances in powder metallurgy: 6. Developments in metal injection moulding (MIM)*. Woodhead Publishing Series in Metals and Surface Engineering. Elsevier Science.

Travitzky, N.A (1998). "Microstructure and mechanical properties of alumina/copper composites fabricated by different infiltration techniques". In: *Materials Letters* 36.1, pp. 114 –117.

Trusty, P.A. and J.A. Yeomans (1997). "The toughening of alumina with iron: Effects of iron distribution on fracture toughness". In: *Journal of the European Ceramic Society* 17.4, pp. 495 –504.

Tuan, W-H. and R-Z. Chen (2002). "Interactions between toughening mechanisms: Transformation toughening versus plastic deformation". In: *Journal of Materials Research* 17.11, pp. 29212928.

Tuan, W. H., H. H. Wu, and T. J. Yang (1995). "The preparation of Al_2O_3/Ni composites by a powder coating technique". In: *Journal of Materials Science* 30.4, pp. 855–859.

Tuan, Wei-Hsing, Jiang-Rung Chen, and Tsong-Jen Yang (2007). "Minimum amount of nano-sized nickel particles to enhance the strength of alumina". In: *Journal of the European Ceramic Society* 27.16, pp. 4705 –4709.

Tuan, W.H. and R.J. Brook (1990). "The toughening of alumina with nickel inclusions". In: *Journal of the European Ceramic Society* 6.1, pp. 31 –37.

Tuan, W.H and R.J Brook (1992). "Processing of alumina/nickel composites". In: *Journal of the European Ceramic Society* 10.2, pp. 95 –100.

Vickers Hardness of the Elements. http://periodictable.com/Properties/A/VickersHardness.html. [Online; accessed 2018].

Wang, J., C. Ponton, and P. Marquis (1993a). "Microstructure and mechanical properties of pressureless sintered alumina-silver composites". In: *Journal de Physique IV Colloque* 03.C7, pp. C7–1769–C7–1774.

Wang, J., C.B. Ponton, and P.M. Marquis (1993b). "The microstructure of pressureless sintered silver-toughened alumina: an in situ TEM study". In: *Materials Science and Engineering: A* 161.1, pp. 119 –126.

Wang, Lin et al. (2001). "The thermal shock behavior of alumina-copper composite". In: *Materials Research Bulletin* 36.5, pp. 925 –932.

Wang, S-C. and W-C.J. Wei (1998). "Characterization of Al_2O_3 composites with Mo particulates, II. Densification and mechanical properties". In: *Nanostructured Materials* 10.6, pp. 983 –1000.

Wei, W-C.J., S-C. Wang, and F-H. Cheng (1998). "Characterization of Al_2O_3 composites with fine Mo particulates, I. Microstructural development". In: *Nanostructured Materials* 10.6, pp. 965 –981.

Wessel, J.K. (2004). *The Handbook of Advanced Materials: Enabling New Designs*. Wiley-Interscience publication. Wiley.

Wilkinson, D.S. (2000). *Mass Transport in Solids and Fluids*. Cambridge Solid State Science Series. Cambridge University Press.

Xia, K. and G.L. Terence (1994). "The toughening and strengthening of ceramic materials through discontinuous reinforcement". In: *Journal of Materials Science* 29.20, pp. 5219–5231.

Yao, X. et al. (2005). "Alumina-nickel composites densified by spark plasma sintering". In: *Materials Letters* 59.18, pp. 2314 –2318.

Yeomans, J.A. (2008). "Ductile particle ceramic matrix composites - Scientific curiosities or engineering materials?" In: *Journal of the European Ceramic Society* 28.7, pp. 1543 –1550.

Zygmuntowicz, J. et al. (2016). "Structural and mechanical properties of graded composite Al_2O_3/Ni obtained from slurry of different solid content". In: *Procedia Structural Integrity* 1.Supplement C, pp. 305 –312.

Index

List of Figures

List of Tables

References for the Figures and the Tables

The sources used for the images, and the origin of data used in the tables are summarized in this list.

Figure 1
Shackelford and Doremus, 2008

Figure 2
Carter and Norton, 2007

Figure 3
Lee and Rainforth, 1994

Figure 2.1
Basu and Balani, 2011

Figure 2.2
Rodríguez-Reinoso et al., 1994

Figure 2.3
Lee and Rainforth, 1994

Figure 2.5
Hosford, 2010

Figure 2.6
Sadowski and Marsavina, 2011

Figure 2.10
German, 2014

Figure 2.11
Carter and Norton, 2007

Figure 2.12
Carter and Norton, 2007

Figure 2.13
Wilkinson, 2000

Figure 2.14
Wessel, 2004

Figure 2.15
Rahaman, 2003

Figure 2.16
Richerson, Richerson, and Lee, 2005

Figure 2.17
Azar et al., 2008

Figure 2.18
German, 1987

Figure 2.19
Lee and Rainforth, 1994

Figure 2.20
Kang, 2004

Figure 2.21
Barsoum and Barsoum, 2002

Figure 2.22
German, 2014

Figure 2.23
Barsoum and Barsoum, 2002

Figure 2.24
Kwon et al., 1987

Figure 2.25
German, 2014

Figure 2.26
Ashby, Blunt, and Bannister, 1989

Figure 2.27
Ponnusami, Turteltaub, and Zwaag, 2015

Figure 2.28
Donald and McMillan, 1976

Figure 2.29
Tirosh and Tetelman,

1976

Figure 2.30
German, 2014

Figure 2.31
Nikolopoulos and Agathopoulos, 1992

Figure 2.32
Pines and Bruck, 2006

Figure 2.33
Chou and Tuan, 1995

Figure 2.34
Wei, Wang, and Cheng, 1998

Figure 2.35
Li, Huang, and Guo, 2003

Figure 2.36
Lu et al., 2000

Figure 2.37
Wang, Ponton, and Marquis, 1993b

Figure 2.38
Dutta, Chattopadhyaya, and Ray, 2006

Figure 2.39
Diaz et al., 2003

Figure 2.40
Tuan, Wu, and Yang, 1995

Figure 2.41
Tuan and Chen, 2002

Figure 2.42
Sekino and Niihara, 1997

Figure 2.43
Nawa, Sekino, and Niihara, 1994

Figure 2.44
Sekino and Niihara, 1997

Figure 3.9
IMCE NV

Figure 3.10
IMCE NV

Figure 3.11
Mouritz, 2012

Table 2.1
Cardarelli, 2008

Table 2.2
Cardarelli, 2008

Table 2.3
Rahaman, 2003; Mitchell, 2004

Table 2.4
Nikolopoulos and Agathopoulos, 1992

Table 4.1
American Mineralogist Crystal Structure Database

Η παρούσα Διδακτορική Διατριβή εντάσσεται στο πλαίσιο υλοποίησης της Πράξης ΘΑΛΗΣ - ΕΜΠ, με Επιστημονικό Υπεύθυνο την Καθ. Αθηνά Τσετσέκου, και τίτλο: "Ανάπτυξη σύνθετων νανοδομημένων υλικών κεραμικής μήτρας με μεταλλικά εγκλείσματα". Το έργο αυτό συγχρηματοδοτήθηκε από το Ευρωπαϊκό Κοινωνικό Ταμείο και από Εθνικούς Πόρους μέσω του Επιχειρησιακού Προγράμματος Εκπαίδευσης και Δια Βίου Μάθησης.

Διδακτορική Διατριβή
Μαρία Στρατηγάκη
mstratigaki@isc.tuc.gr
ΑΜ: 2013040351

Επιβλέπων Καθηγητής
Αλέξανδρος Δ. Γκότσης
gotsis@science.tuc.gr

Δημοσίευση | 2014
M. Stratigaki, G. Choudalakis, A.D. Gotsis
Gas transport properties in waterborne polymer nanocomposite coatings containing organomodified clays, Journal of Coatings Technology and Research (2014) 11:899
(7 Citations | 2018)

Παρουσίαση σε Συνέδριο | Πάτρα, 5 Ιουνίου 2015
Maria Stratigaki and Alexandros D. Gotsis
Mechanical properties of metal/ceramic composites
$10^{ο}$ Πανελλήνιο Επιστημονικό Συνέδριο Χημικής Μηχανικής

Τεχνική Έκθεση | Νοέμβριος 2015
Μαρία Στρατηγάκη & Αλέξανδρος Δ. Γκότσης
Τελική Τεχνική Αναφορά της πράξης ΘΑΛΗΣ - ΕΜΠ με τίτλο:
Ανάπτυξη Σύνθετων Νανοδομημένων Υλικών Κεραμικής Μήτρας με Μεταλλικά Εγκλείσματα. Πακέτο Εργασίας 7: Θεωρητική και υπολογιστική ανάλυση συσχέτισης διεργασιών, μικροδομής, ιδιοτήτων των κεραμικών προϊόντων.

Εργασία 7.3: Στατιστική συσχέτιση ιδιοτήτων/μικροδομής και δημιουργία θεωρητικών μοντέλων. Εργασία 7.4: Ανάλυση κρίσιμων παραμέτρων-αξιολόγηση.

Τελική Παρουσίαση σε Ημερίδα | 27 Νοεμβρίου 2015
Maria Stratigaki & Alexandros D. Gotsis
Development of Theoretical Models for the Elasticity and the Ultimate Properties of Ceramic-matrix/Metal-inclusions Composites

Δημοσίευση | 2018
M. Stratigaki, W. Pabst, V. Nečina, M. Hajíček, A.D. Gotsis
Microstructure and mechanical properties study of slip-casted copper-alumina composites, Journal SN Applied Sciences (2018)

Άρθρα υπό κρίση για δημοσίευση | 2018
Reinforcing the alumina matrix with both copper and tungsten inclusions
Young's modulus of ceramic-matrix composites with dispersed metallic particles

About the Author

Maria Stratigaki obtained her Ph.D. in Materials from the School of Mineral Resources Engineering of the Technical University of Crete, Greece, in 2018 under the supervision of Prof. Alexandros D. Gotsis on the research area of Composite Materials comprising of Ceramic-matrix and Metallic second-phase inclusions, in which she enrolled in 2013. During her studies, in 2016-2017, she visited the Faculty of Chemical Technology of the University of Chemistry and Technology, UCT Prague in Czech Republic, and conducted research related to her Doctoral Dissertation at the Department of Glass and Ceramics under the direction of Prof. Willi Pabst. From 2010 to 2012 she attended a M.Sc. program in the Division of Materials and Structures at the Department of Applied Sciences of the Technical University of Crete, under the supervision of Prof. A.D. Gotsis and fabricated Polymeric Nanocomposite Coatings for Enhanced Gas Barrier Properties. She also visited the Positron Annihilation Laboratory of the Martin-Luther University Halle-Wittenberg in Halle/Saale Germany to conduct measurements via the Positron Annihilation Lifetime Spectroscopy technique under the attention of Prof. Reinhard Krause-Rehberg. From 2005 to 2010, she was an undergraduate student at the University of Crete and obtained her Degree from the Department of Materials Science and Technology. She also conducted a research project in 2010, on Dynamics and Rheology of Colloidal Star/Linear Polymer Mixtures, at the Polymer and Colloid Science Laboratory of the Institute of Electronic Structure and Laser, IESL-FORTH in Heraklion Greece under the direction of Dr. Domenico Truzzolillo and Prof. Dimitris Vlassopoulos.

LaTeX